

# Precision emulation of high contrast images using the low-order wave front sensor telemetry

Garima Singh (3262), Jet Propulsion Laboratory, California Institute of Technology  
Ashmeet Singh, California Institute of Technology

## Scientific Motivation

One of the goals identified in Astro2010/New Worlds roadmap is the atmospheric characterization of exoplanets through **direct imaging** techniques. The quest is to search for rocky exoplanets that might hold liquid water on their surface.

## A Technical Requirement

To image a terrestrial-like planet around a solar-type star (required contrast is  $10^{-10}$ ) with an angular resolution of a 2-4 meters space telescope, one of the requirement is to perform High Contrast Imaging (HCI) using the coronagraphs optimized for small inner working angle (IWA).

## Challenges foreseen for direct imaging in space

Thermal distortion, pointing errors and vibrations due to reaction wheels introduce low-order wave front aberration upstream of coronagraphs, which leaks starlight around the coronagraphic mask. A dedicated low-order wavefront sensor (LOWFS) can control these leaks, however, with an adjustable gain factor and after a processing delay. The non-zero low-order residuals per control loop iteration always leave some residual starlight in the final science image, especially at  $< 3 \lambda/D$ . **This is the region where the current post-processing techniques such as ADI/RDI can not enhance the detection sensitivity.**

Using the state-of-the-art post-processing techniques, future space-based missions such as WFIRST (IWA  $\sim 3 \lambda/D$ ), Exo-C (IWA  $\sim 2 \lambda/D$ ) and HabEx (IWA  $\sim 1-3 \lambda/D$ ) will be able to improve the raw contrast by 2 to 3 orders of magnitude but only at large angular separations.

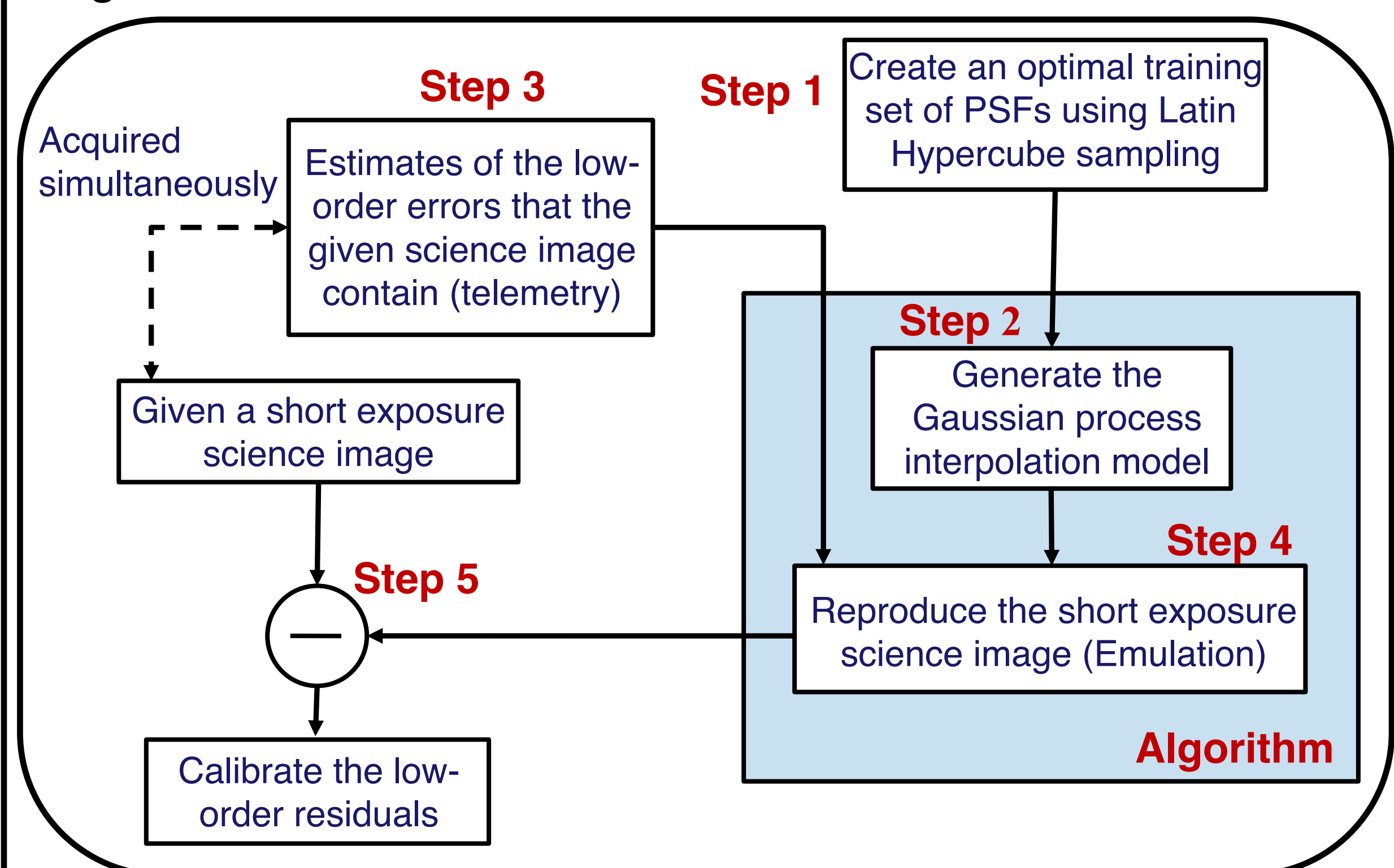
## Our Goal

At small IWA ( $\sim 1-3 \lambda/D$ ), improve contrast by calibrating leaked low-order residuals left uncorrected by the LOWFS control loop.

## Methodology

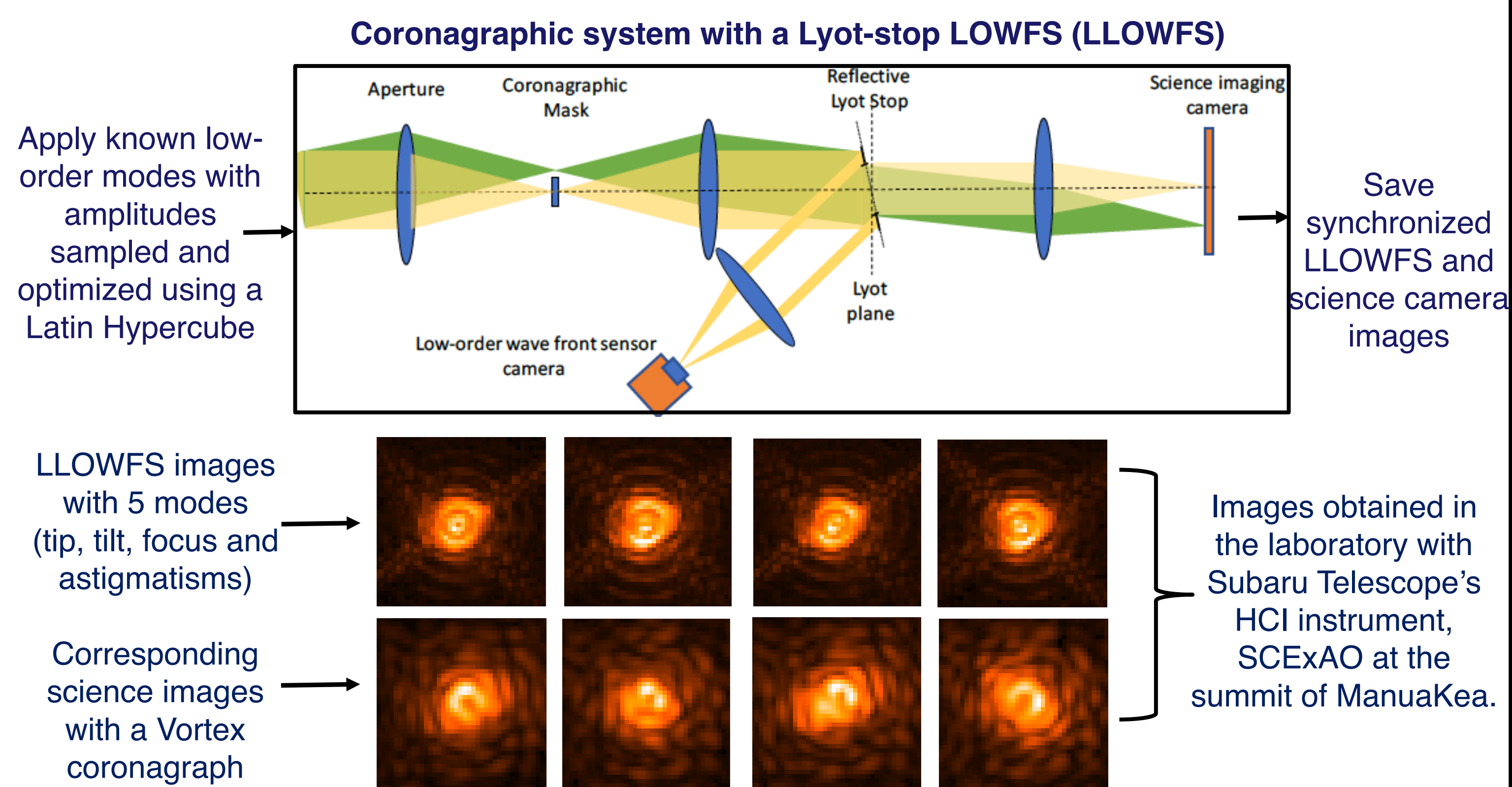
- Acquire a pre-computed knowledge on how a coronagraphic system respond to low-order aberrations. Create a PSF library containing the low-order images (measurements) and the corresponding science images affected by the low-order errors.
- Reproduce a given science image using the library and the LOWFS telemetry (saved during the observation).

The method is based on optimal sampling of the training set and uses Gaussian process modelling to recreate/emulate given science images.



## Procedure

### Step 1: Generating a training set of PSFs (performed prior of science observation)



### Step 2: Generate the model (this step is performed prior of science observation)

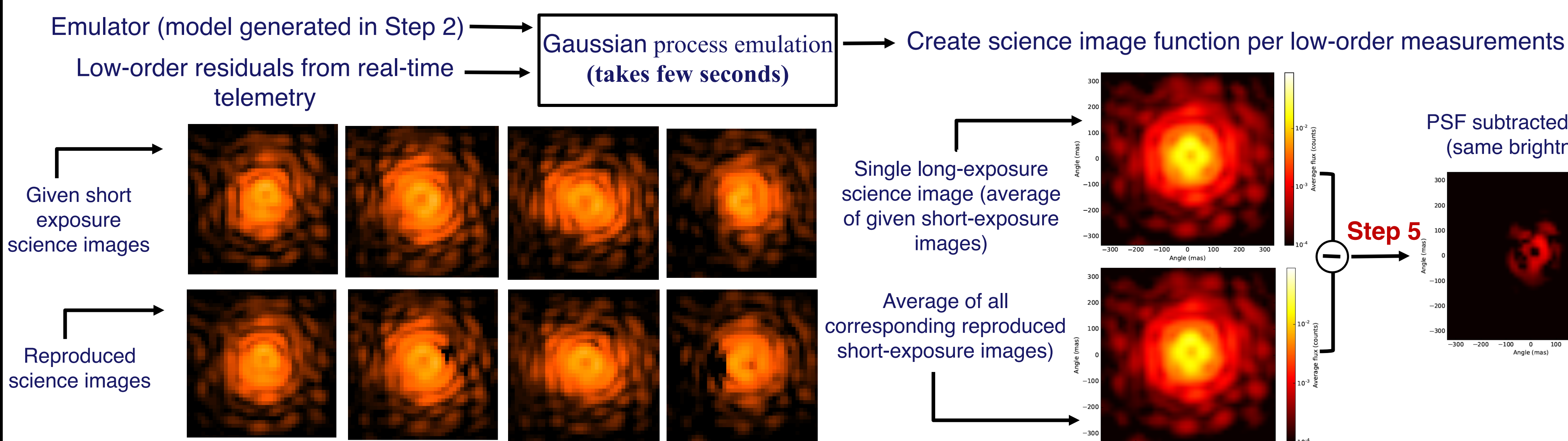


### Step 3: Save telemetry (this step is performed during science observation)

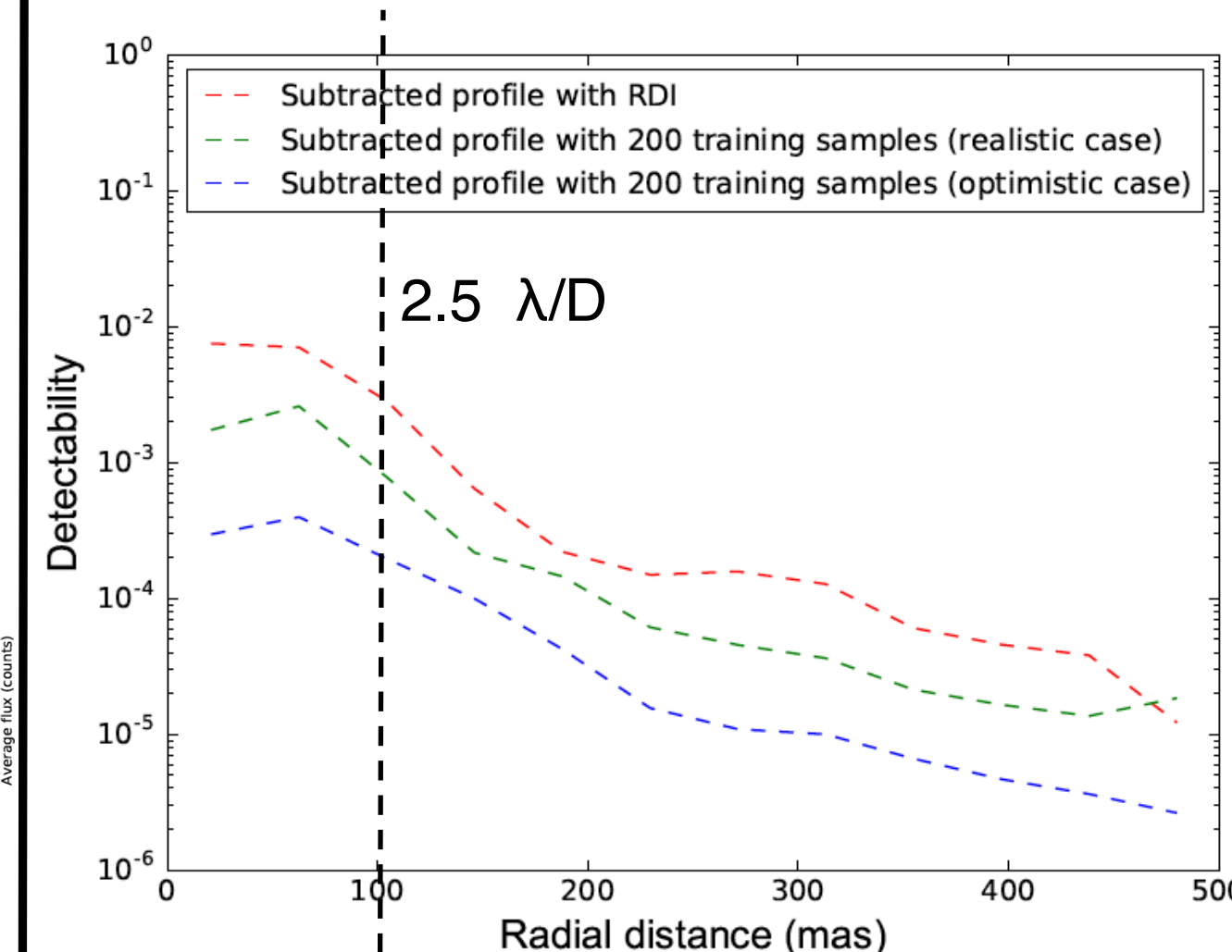
Save short-exposure science images and corresponding LLOWFS images/residuals during the science observation.

## Laboratory Results (Instrument: SCEAO at Subaru Telescope, Coronagraph: Vortex)

### Step 4: Reproduce short exposure science images using the LLOWFS telemetry acquired during science observation



### Radial azimuthal profile showing standard deviation of PSF subtracted profiles



The proposed technique significantly improve Contrast at  $< 3 \lambda/D$  over RDI

## Significance of Results

- Can calibrate coronagraphic leaks at  $< 3 \lambda/D$  and enhance detection sensitivity at small angles.
- Complementary to existing post-processing techniques.
- Can relax the requirement on telescope diameter and level of raw contrast achieved by space-based coronagraph.

- Using our proposed method, the starlight leaks can be calibrated with the Zernike WFS as well. This will increase the TRL of WFIRST mission!

# Evidence of the “brighter-fatter” effect in near-infrared detectors

Andrés A. Plazas Malagón (3268)

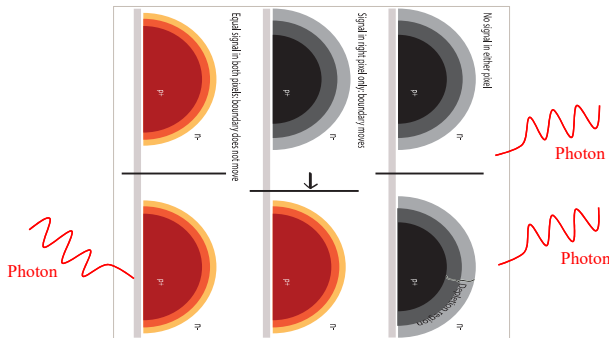
Eric Huff (3268), Jason Rhodes (3200), Charles Shapiro (389E), Roger Smith (COO)

## Introduction

Weak gravitational lensing (WL) is one of the most powerful tools to map dark matter and to constrain models of dark energy. It requires accurate shape measurements of millions of galaxies only a few pixels wide. The size (shape) of the point spread function (PSF) of the system must be known to an accuracy of order 0.001 (0.0001).

Most WL surveys to day have used charged-coupled devices (CCDs). In CCDs, photo-charges are deflected away from bright pixels due to previously accumulated charge in the pixel, distorting the detector PSF in a non-trivial way. The pixel boundaries shift, redistributing the charge in the pixel array, brighter sources appear artificially larger (the “brighter-fatter” effect), and peak fluxes are suppressed.

Future space missions (e.g., WFIRST) will use near-infrared (NIR) detectors, which have different physics compared to CCDs. **Is there a BF-type effect in NIR detectors?** There are physical reasons to expect such an effect in them:

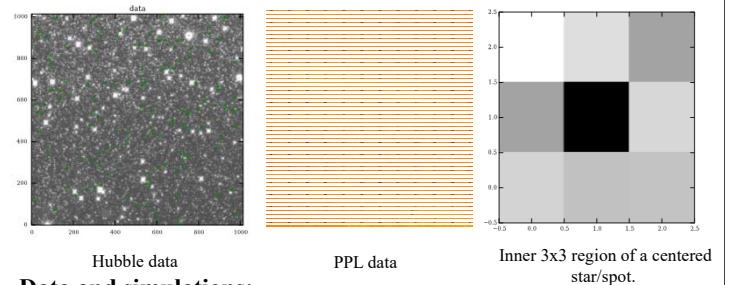


In a pixel of a NIR sensor, the charge is collected at the depletion region. As charge accumulates, the depletion regions shrinks. This effectively shifts the boundary of the pixels, creating a “brighter-fatter” effect. The effect depends on the charge contrast between pixels.

## Measurements and Simulations

### Common analysis:

- Use bright, isolated, and unsaturated stars/spots, with centers within  $\pm 0.1$  pixel of a pixel center. The larger the pixel contrast, the larger the effect.
- Correct for known detector effects (e.g., classical non-linearity).
- Stack stars/laboratory spots and examine normalized readings to look for **signal loss in the central pixel and excess signal in the neighboring pixels as integration time increases.**

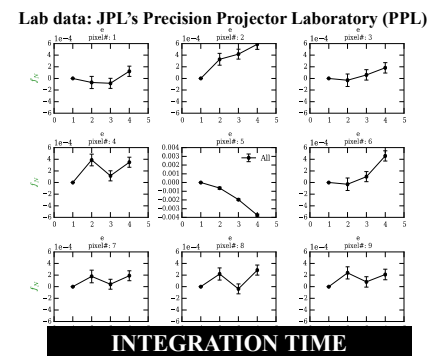
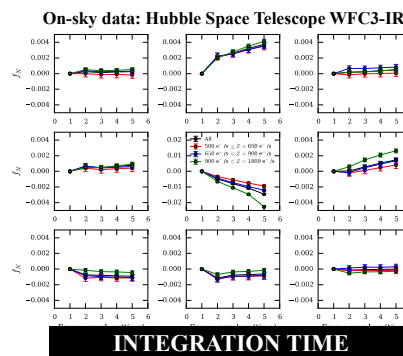
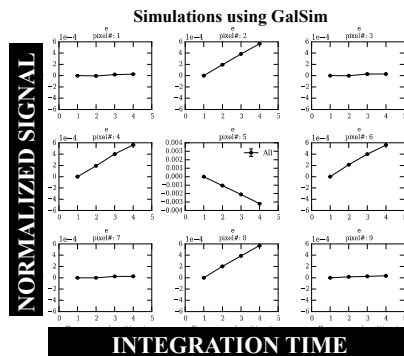


### Data and simulations:

- **On-sky data:** Globular cluster in Omega centauri, imaged with the H1RG NIR detector of the Wide Field Camera 3 of the Hubble Space Telescope.
- **Lab data:** JPL’s Precision Projector Laboratory (PPL). Project point sources with a FWHM  $< 1$  pixel (under-sampled) on a H2RG MIR detector, similar to space missions.
- **Simulations:** We use Galsim, a public code to simulate PSF and galaxy profiles for WL analyses. We simulate the PPL data, including known effects and noise sources, and use the phenomenological “brighter-fatter” model included in Galsim.

## Results

- In both WFC3-IR and PPL data, the normalized signal in the central pixel decreases with time (1-2%), while the signal in the nearest neighbors tends to increase.
- The sum of the signal (flux rate) in the surrounding 8 pixels is roughly equal to the decrease in signal of the central pixel.
- The charge redistribution, sign, and symmetry are consistent with our physical model, and qualitatively consistent with simulations.



## Conclusions

- We find **evidence of the brighter-fatter effect** in near infrared detectors, using HST and laboratory data.
- The BF effect will induce photometric and astrometric errors not only on WL science but on supernovae and microlensing measurements as well.
- More details can be found in *Plazas et al., JINST, Vol. 12, 2017.*

# High Resolution Photoacoustic Spectroscopy of the Oxygen A-Band

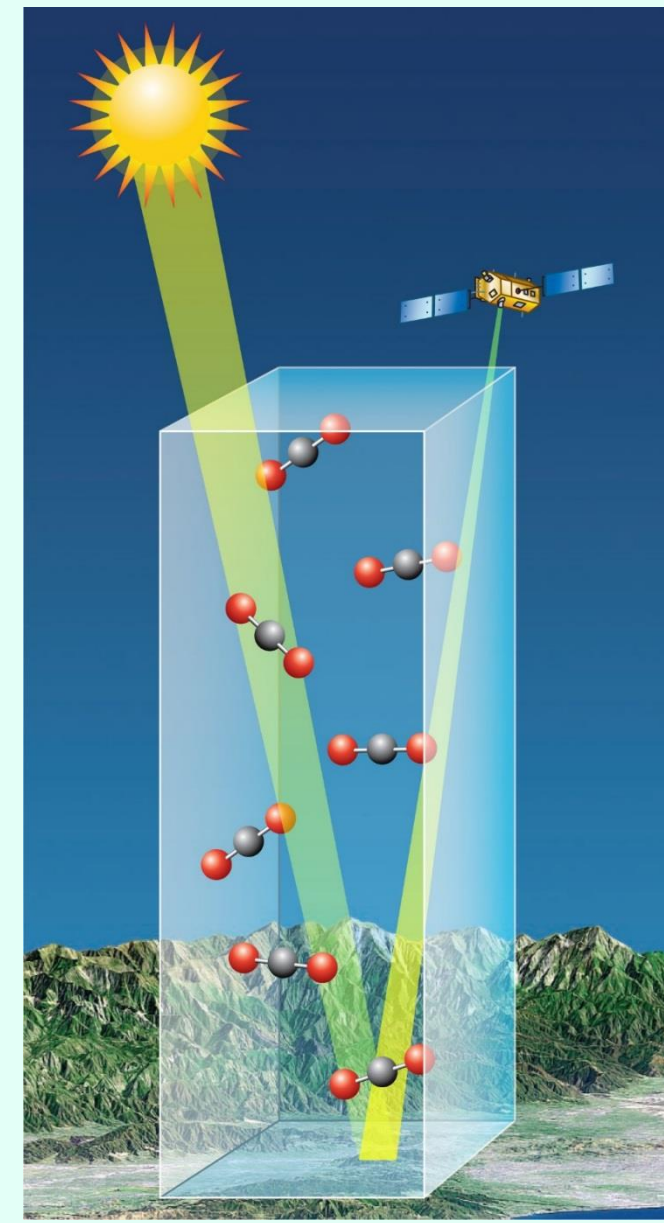
Matthew J. Cich (329H)

Elizabeth M. Lunny<sup>1</sup>, Gautam D. Stroscio<sup>1</sup>, Brian J. Drouin (329H), Mitchio Okumura<sup>1</sup>

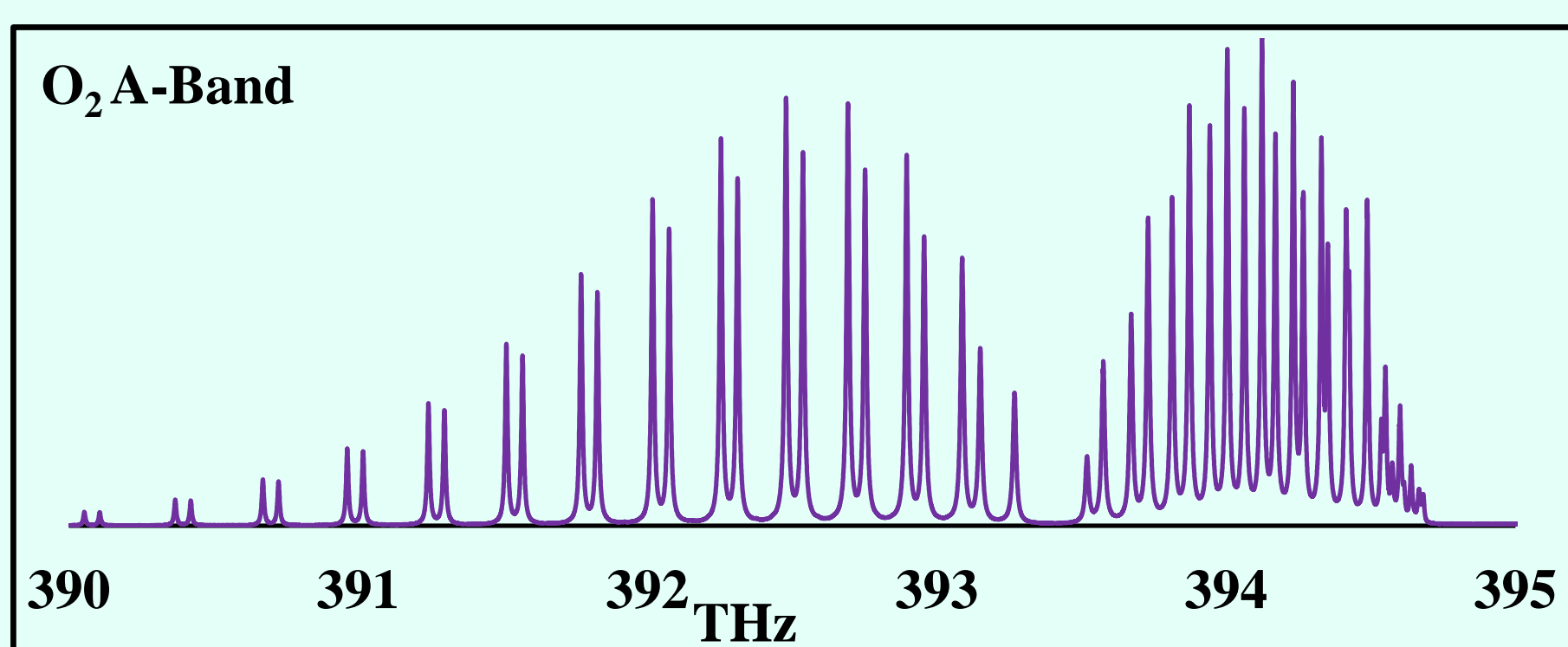
<sup>1</sup>Department of Chemistry and Chemical Engineering, California Institute of Technology, Pasadena, CA

## High resolution spectroscopy to support OCO-2

- O<sub>2</sub> is measured by OCO-2 to normalize airmass in the sunlight's path through the atmosphere
- CO<sub>2</sub> air fraction retrieval requires accurate spectroscopy (0.1%) for the O<sub>2</sub> A-band

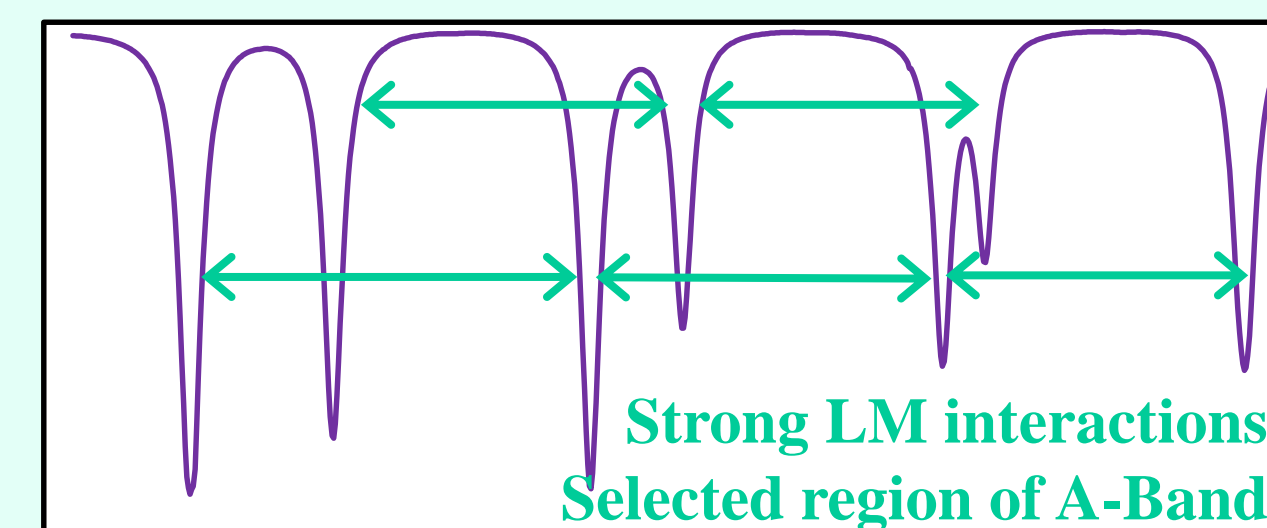


OCO-2 observes three bands: CO<sub>2</sub> (1.6 μm and 2.1 μm) and O<sub>2</sub> (0.8 μm)



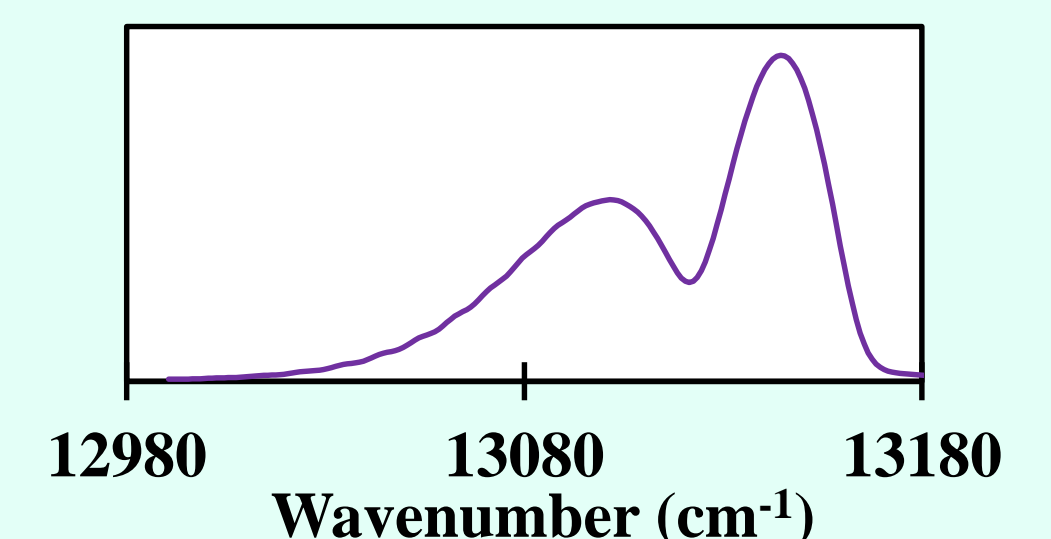
## Line mixing and collision induced absorption negatively affect satellite retrievals

### Line Mixing (LM)



When two nearby lines have interacting quantum levels, stronger lines will steal intensity from weaker lines, and both become asymmetric.

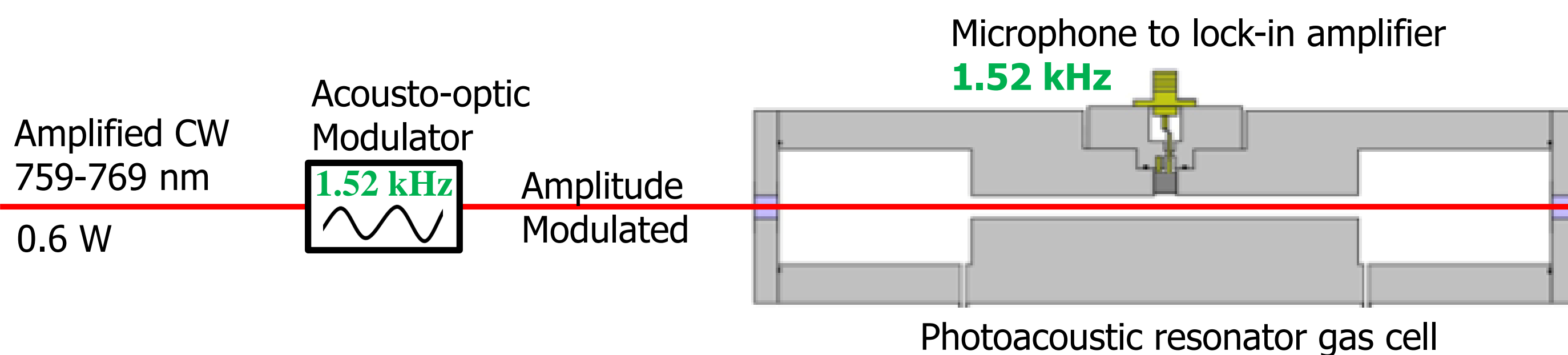
### Collision Induced Absorption (CIA)



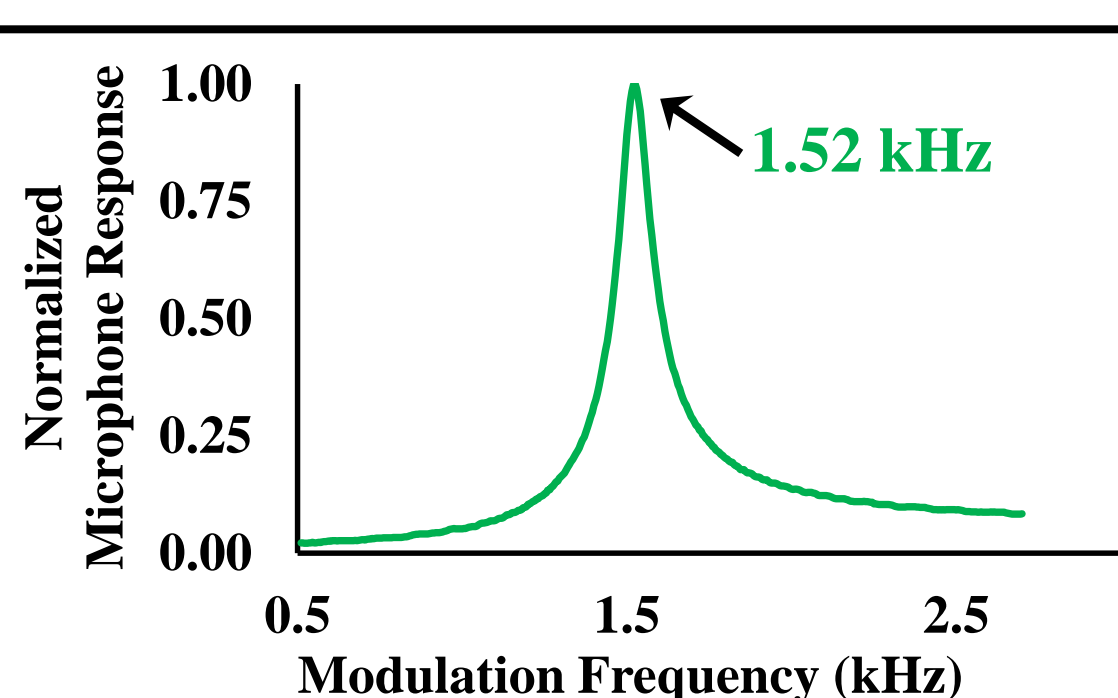
Weak 'continuum' absorption underneath the A-band caused by collision-allowed transitions.

**LM and CIA have at least a 1% effect on satellite retrievals and must be better characterized using laboratory measurements.**

## Photoacoustic spectroscopy overview



**The photoacoustic effect: detecting gas absorption with a microphone**  
Modulated absorption → thermal expansion → pressure wave → sound at modulation frequency



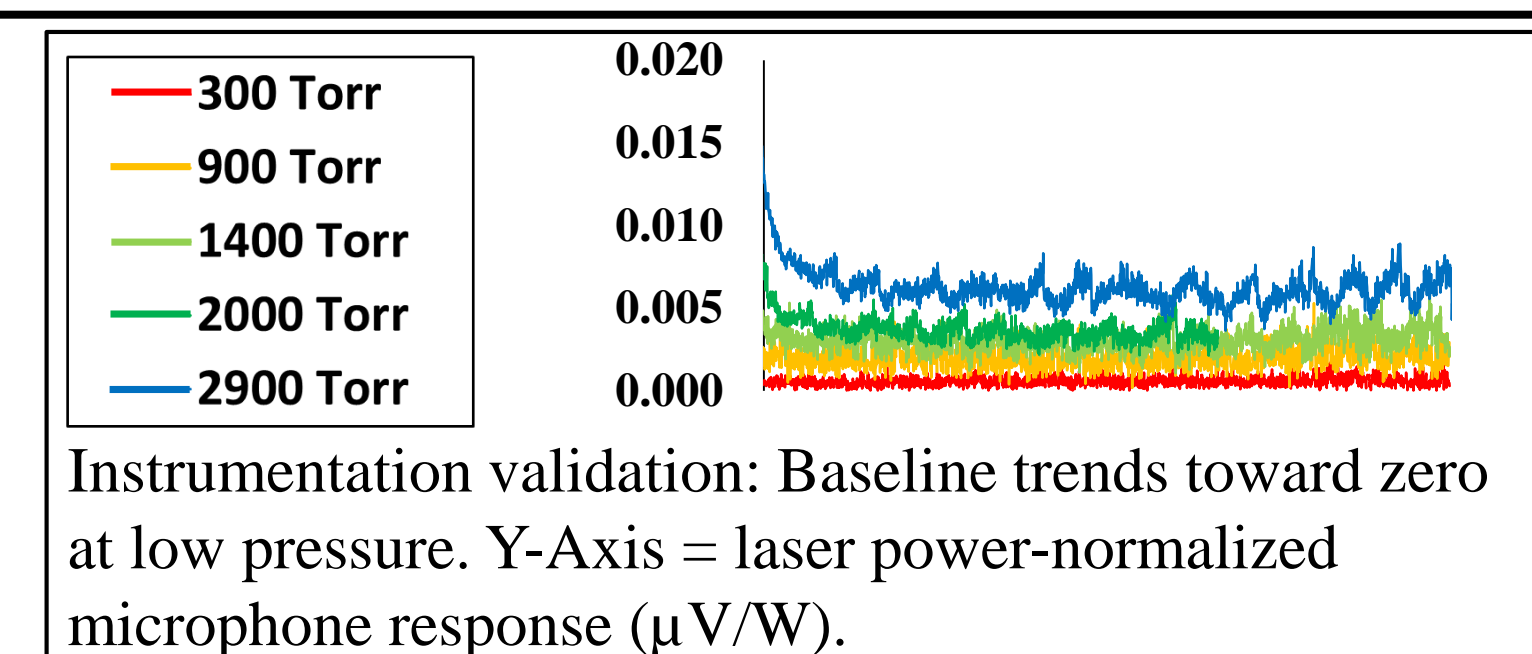
The photoacoustic cell has a peak resonant frequency that depends on gas conditions.

For O<sub>2</sub>, a small quantity of quenching gas, e.g. CF<sub>3</sub>H, must be used to fully modulate absorption at this high frequency.

## Advantages of this spectrometer

### Zero Baseline

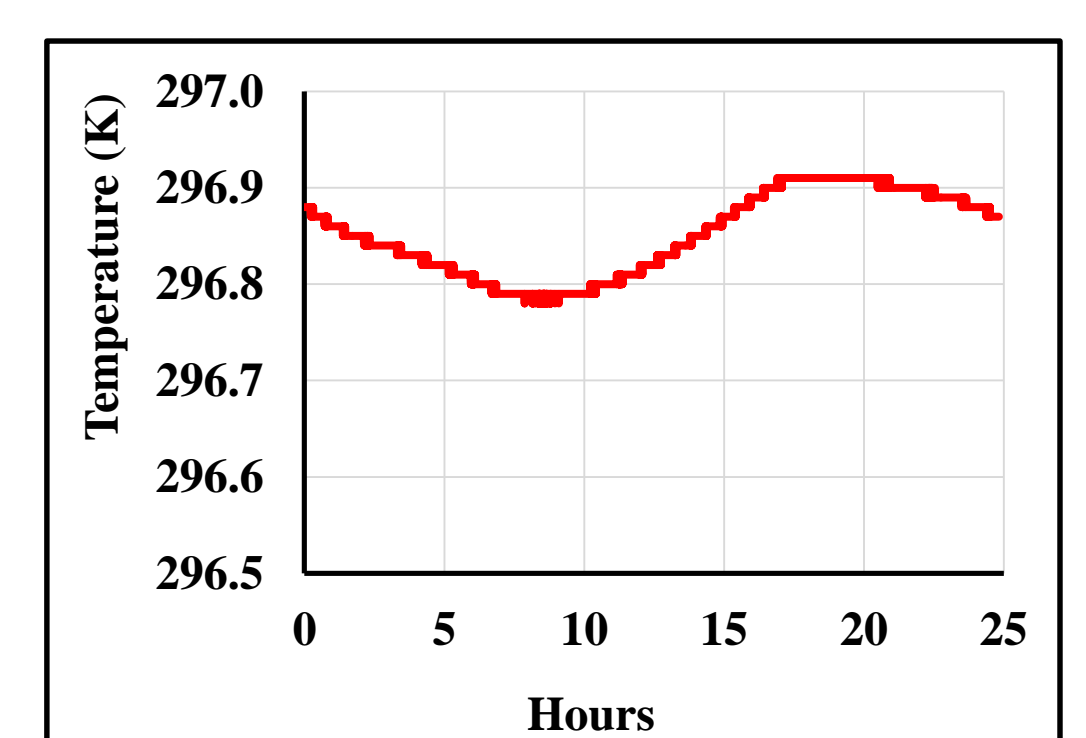
LM and CIA are subtle effects and can be lost in a spectrometer's baseline. Microphone response is wavelength independent.



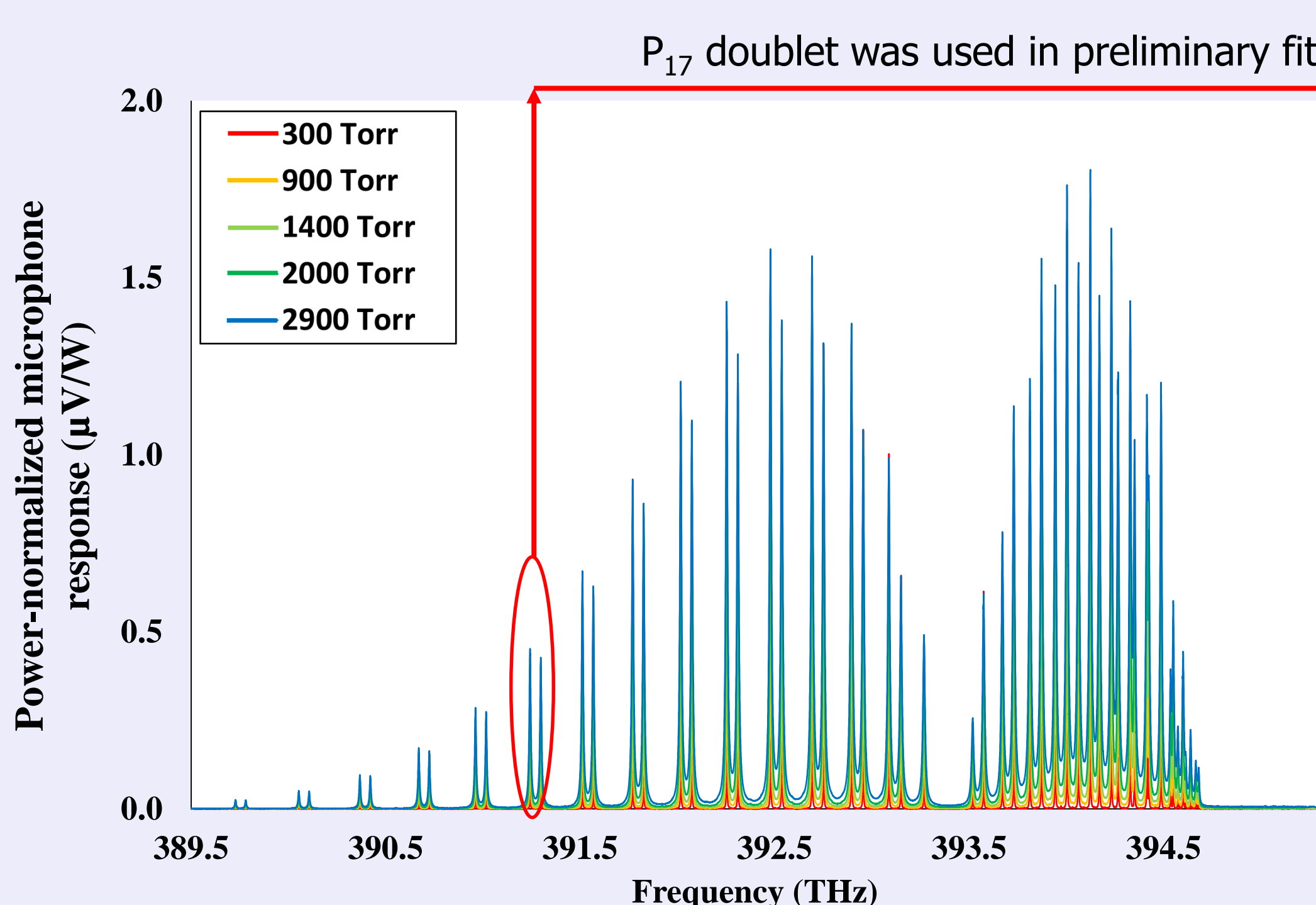
Instrumentation validation: Baseline trends toward zero at low pressure. Y-Axis = laser power-normalized microphone response (μV/W).

### High resolution, efficient, automated design

- **'Autopilot'**: Modehop-free scanning across 5+ THz A-Band
- **2 MHz High resolution**: Laser locked to stabilized He-Ne referenced wavemeter
- **Fast spectrum acquisition**: Full A-Band scans in 1 day
- **Large pressure range**: ~100-3000+ Torr
- **Temperature Stability**: 0.2 K in 1 day
  - Planned lower temperature measurements 193 – 296 K (microphone limited)



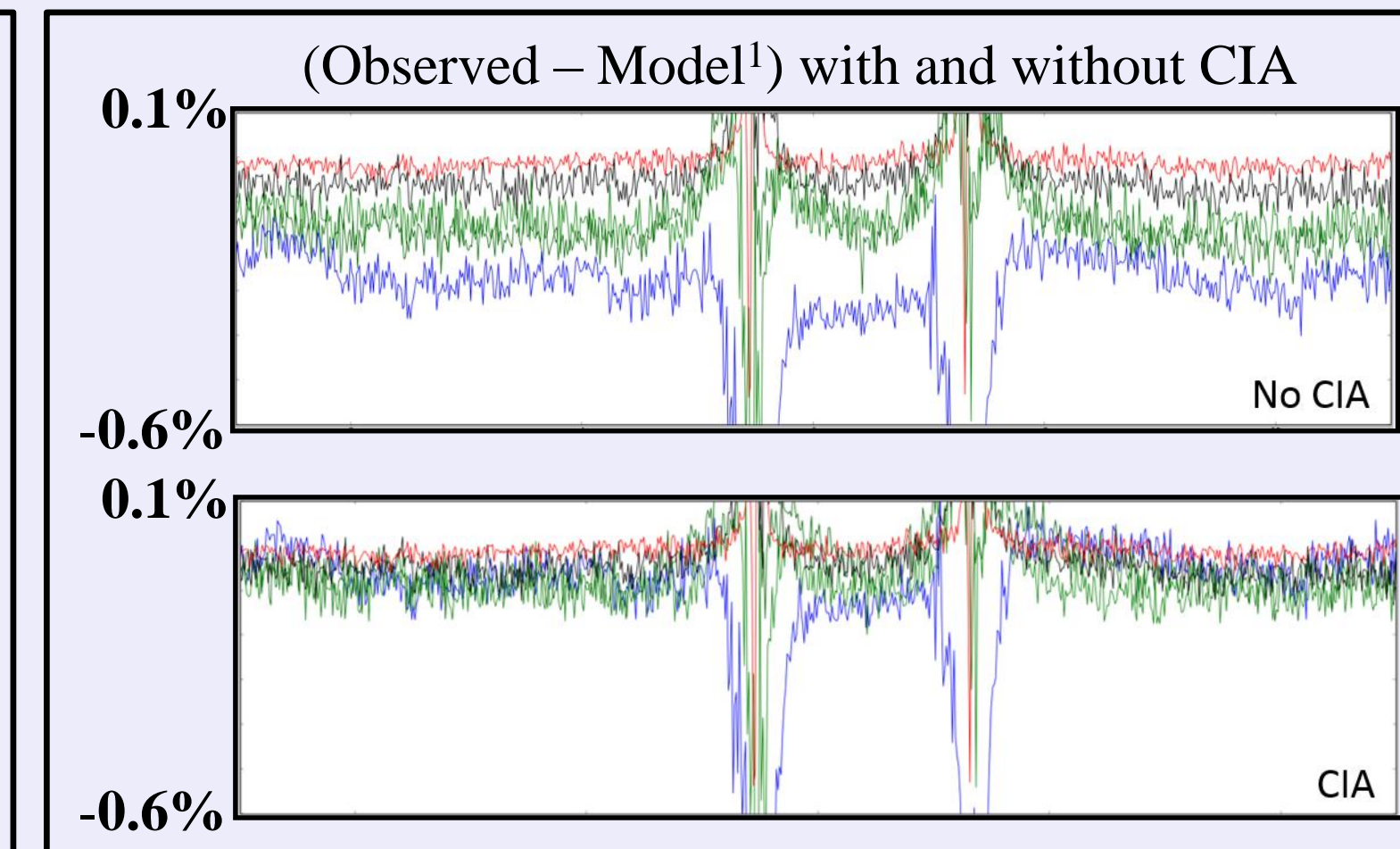
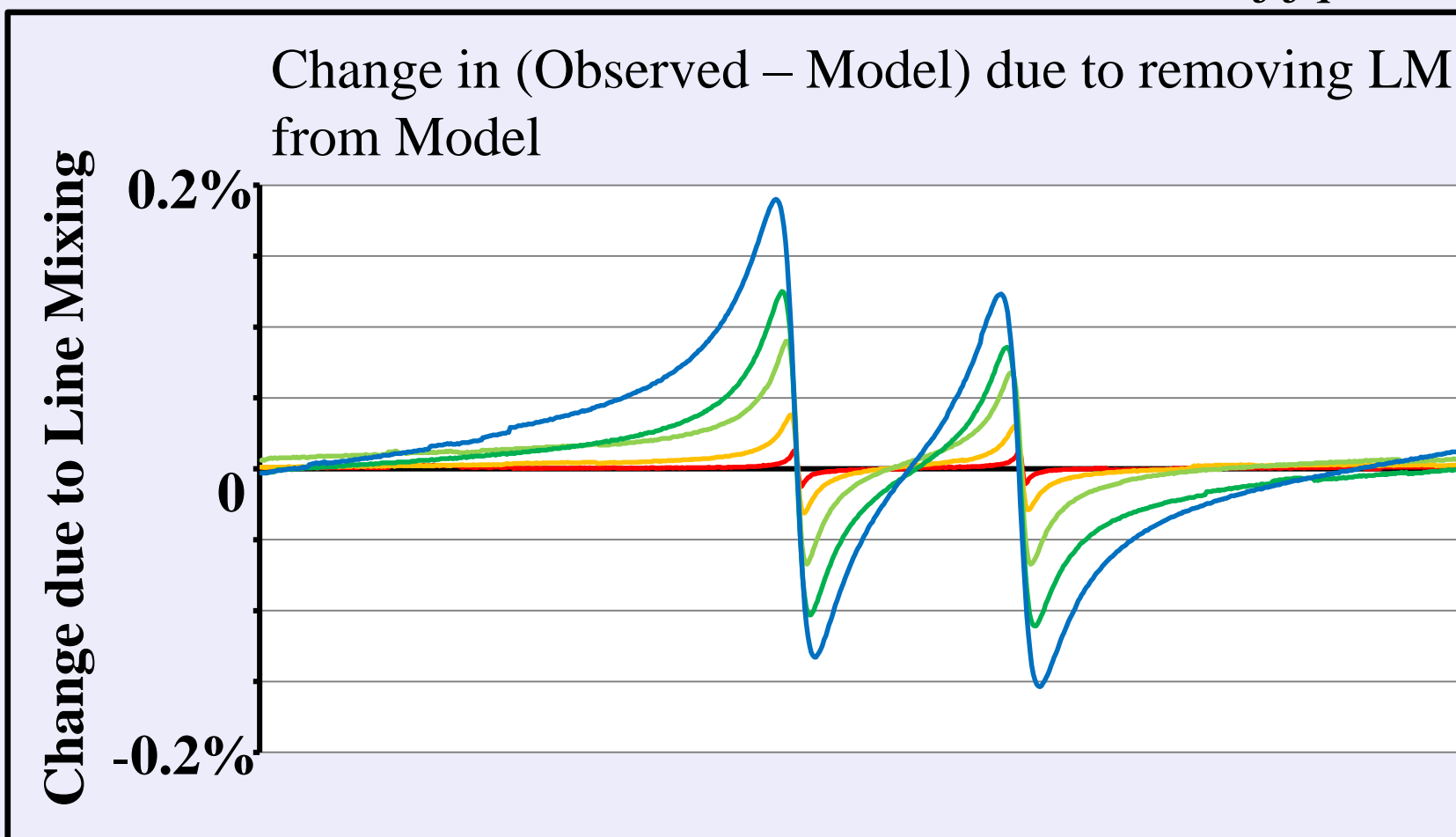
## Conclusion: Laboratory spectra contain significant observable line mixing and collision induced absorption



Photoacoustic spectrum of the O<sub>2</sub> A-Band taken at 5 different pressures.

- P<sub>17</sub> doublet is fit with a published model<sup>1</sup> including LM and CIA.
- LM or CIA are turned off in new fits to see how sensitive the data are to these effects
- The high pressure data show significant LM/CIA sensitivity that **is not present** in low-pressure-only fits
- Once analyzed this data will reduce spectroscopic uncertainties in the A-Band

<sup>1</sup>A-Band model: Drouin et al. DOI: 10.1016/j.jqsrt.2016.03.037



**NEXT STEPS: Spectra of O<sub>2</sub> in air and at different temperatures to characterize LM and CIA at atmospherically relevant conditions**

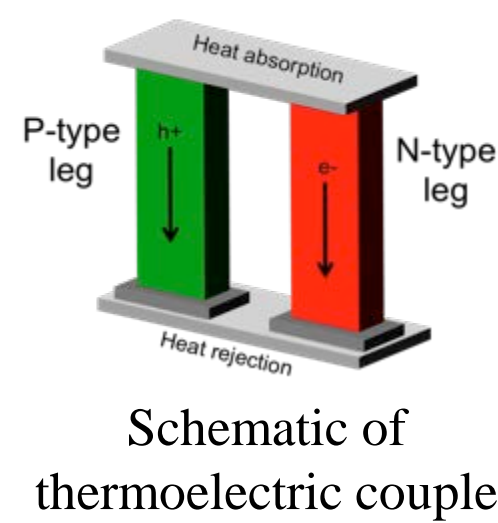
# Investigation of Defects, Thermal Stability, and Transport Properties of $n$ -Type $\text{Mg}_3\text{Sb}_{2-x}\text{Bi}_x$

Author: Kathleen Lee (3464)

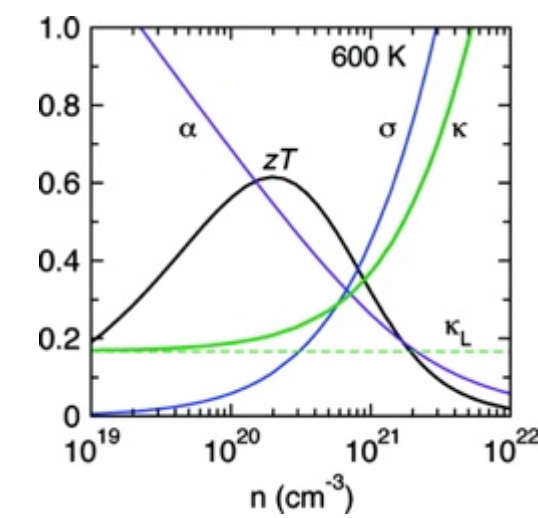
Dean Cheikh (3464), Sabah K. Bux (3464), Jean-Pierre Fleurial (3464)

## Introduction

Radioisotope thermoelectric generators (RTGs) utilize heat from decaying radioisotope fuel to generate electrical power. RTGs have a long history of reliability and are currently in use in missions such as Voyager 1 and 2 as well as on the Mars Curiosity. However, heritage thermoelectric materials suffer from low conversion efficiencies. Maximum thermoelectric efficiency depends on optimizing a material's figure of merit,  $ZT$ , which in turn depends on the Seebeck coefficient,  $S$ , electronic resistivity,  $\rho$ , thermal conductivity,  $\kappa$ , and absolute temperature,  $T$ .



$$\text{Figure of Merit, } ZT = \frac{S^2 T}{\rho \kappa}$$



## Project Objective

- New materials with better electrical and thermal transport properties are required to increase device efficiencies.
- Investigate  $n$ -type  $\text{Mg}_3\text{Sb}_{2-x}\text{Bi}_x$  to determine if the material is feasible for use in future RTGs.
- Develop reproducible bulk synthetic methods and measure high-temperature transport properties.
- Investigate thermal properties, including CTE and the effect of temperature on transport properties

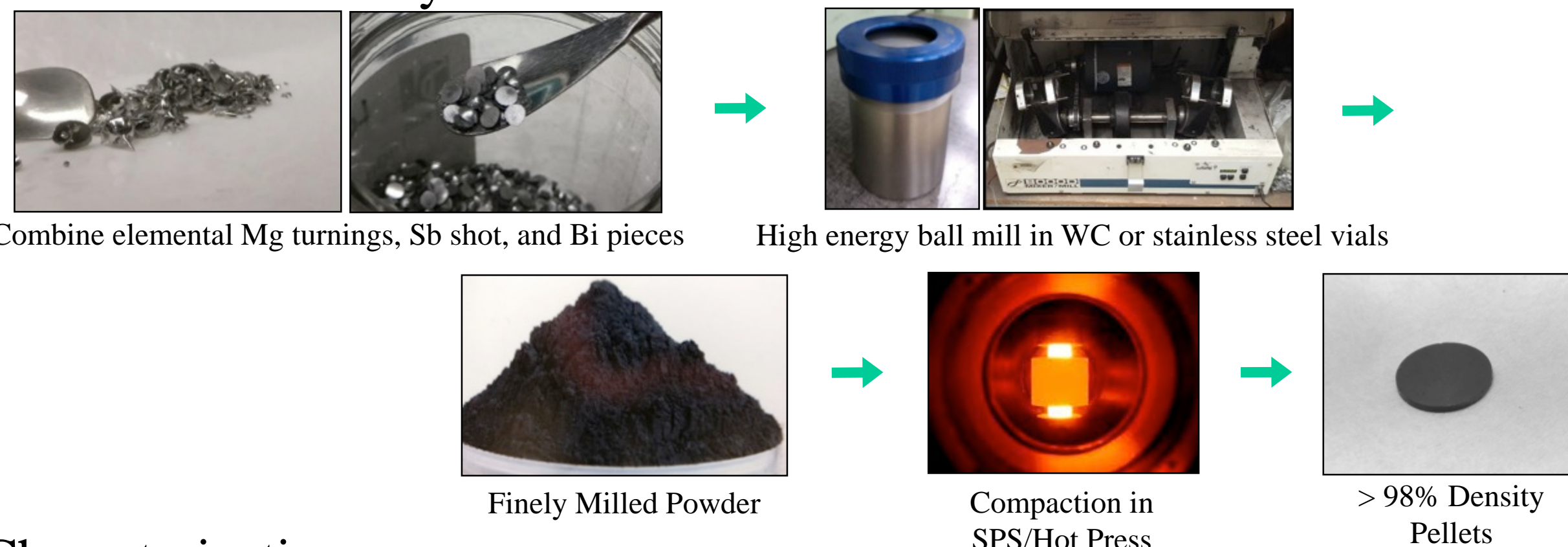


Model of RTG and a few missions that utilized thermoelectric generators.

<https://solarsystem.nasa.gov/rps/discovery.cfm>

## Methodology

### Mechanochemical synthesis:



### Characterization:

- Confirm phase purity via powder X-ray diffraction (PXRD)
- Microstructure analyzed via scanning electron microscopy (SEM) / electron probe microanalysis (EPMA)
- Transport properties measured via 4-point probe Hall, Seebeck, and thermal diffusivity measurements

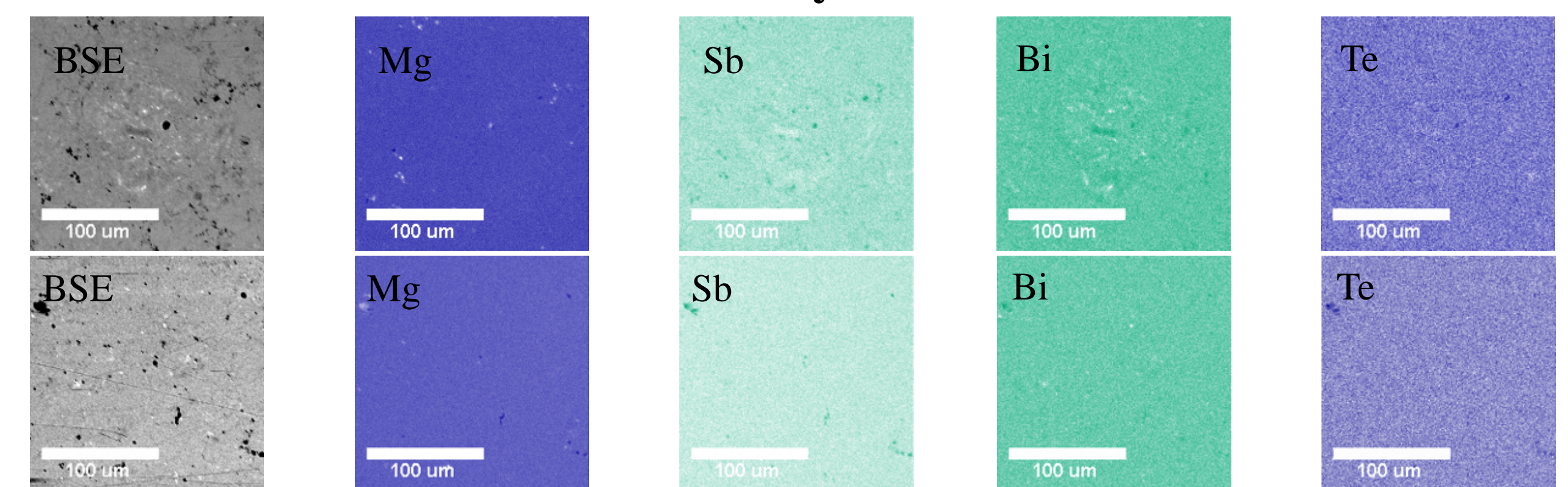


Electrical Transport: Hall, Resistivity, Seebeck Coefficient

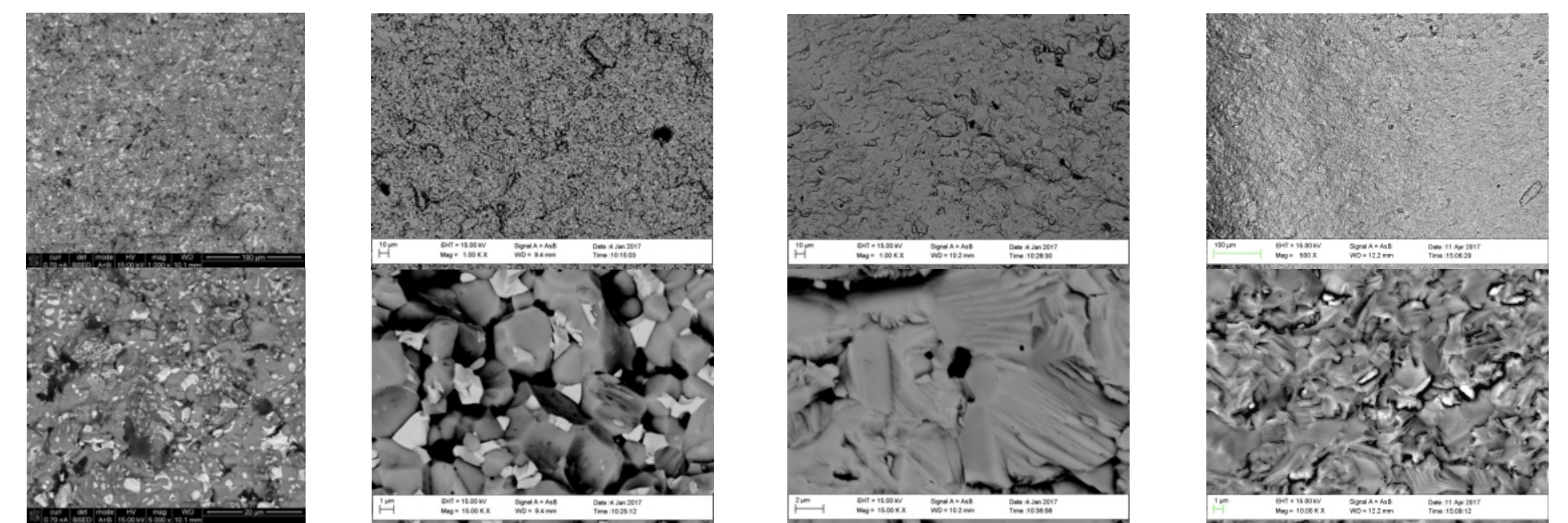


Thermal Transport

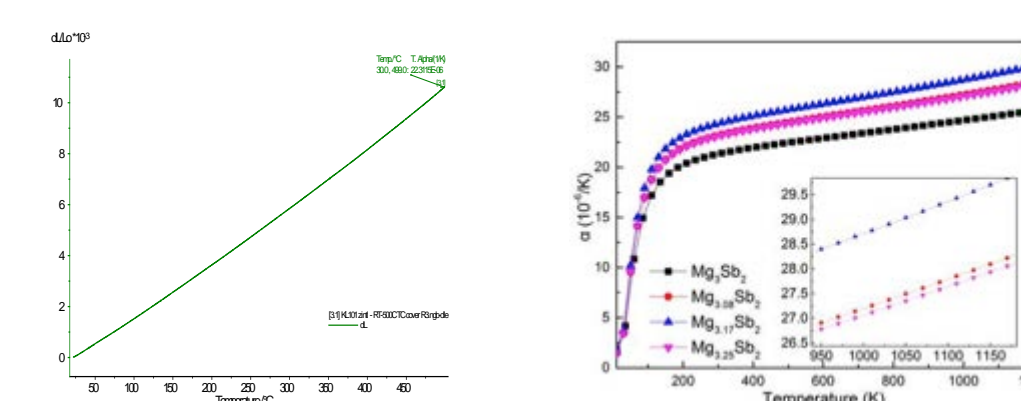
## Microstructure and Thermal Stability



- EPMA map of  $\text{Mg}_3\text{Sb}_{1.6}\text{Bi}_{0.35}\text{Te}_{0.05}$  (top) and  $\text{Mg}_3\text{Sb}_{1.8}\text{Bi}_{0.15}\text{Te}_{0.05}$  (bottom)
- The prepared materials segregate into Bi-rich and Sb-rich areas, even at low Bi concentrations



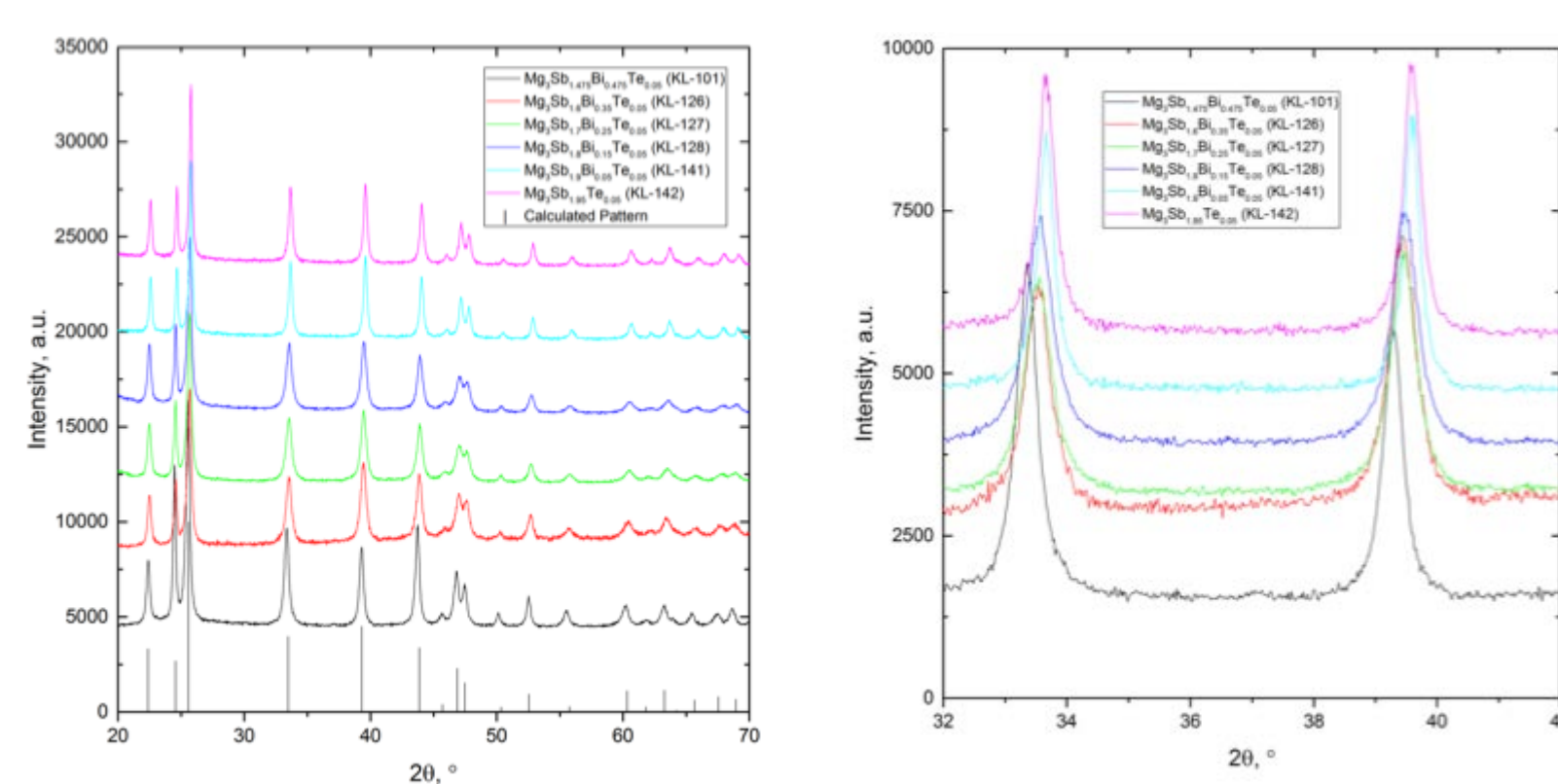
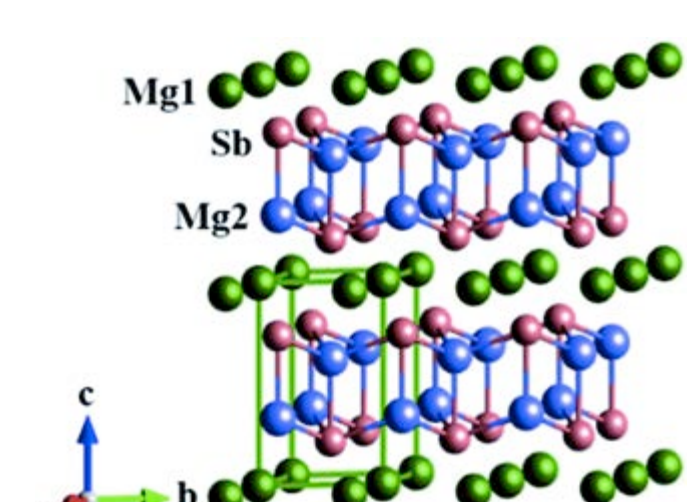
- BSE images of fracture surfaces of  $\text{Mg}_{3.05}\text{Sb}_{1.5}\text{Bi}_{0.49}\text{Te}_{0.01}$  annealed under (a) static vacuum in silica at 973 K, (b) dynamic vacuum in graphite crucible at 873 K, (c) dynamic vacuum in graphite crucible at 773 K, and (d)  $\text{Mg}_{3.0}\text{Sb}_{1.475}\text{Bi}_{0.475}\text{Te}_{0.05}$  annealed under dynamic vacuum in graphite crucible at 773 K
- Phase segregation occurs at temperatures above 773 K or if in contact with silica
- Transport properties of samples with excess Mg are not stable
- No phase segregation or affect in transport properties observed for samples with stoichiometric Mg annealed at 773 K



Properties at 300 K	$S$ , $\mu\text{V/K}$	$\rho$ , $\text{m}\Omega\text{-cm}$	$\mu$ , $\text{cm}^2\text{Vs}$	$n$ , $\text{cm}^{-3}$
Before	-192	5.49	26.8	$4.25 \times 10^{19}$
After	-188	5.23	32.6	$4.75 \times 10^{19}$

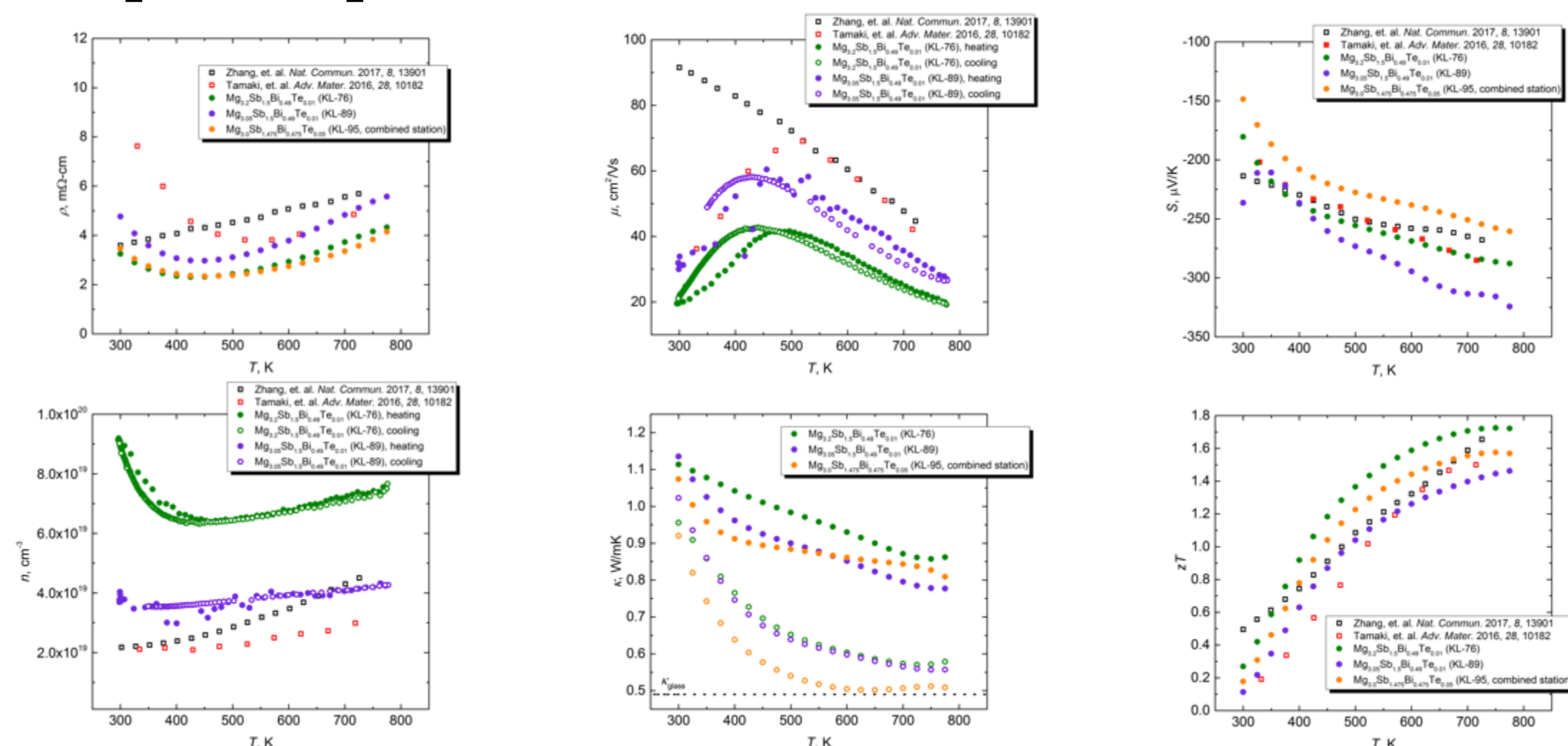
- Sublimation rate measured to be  $9.6 \times 10^{-8} \text{ g/cm}^2\text{h}$  after 2 weeks under dynamic vacuum at 773 K
- No significant change in transport properties after annealing
- Improved sublimation rate compared to heritage materials
- Coefficient of thermal expansion (CTE) measured to be 22 ppm at 773 K
- Matches well with theoretical predictions

## Crystal Structure



- Layered crystal structure with  $[\text{Mg}_2\text{Sb}_2]^{2-}$  layers with a layer of  $\text{Mg}^{2+}$  cations
- PXRD shows a shift in the unit cell as Sb content increases

## Transport Properties



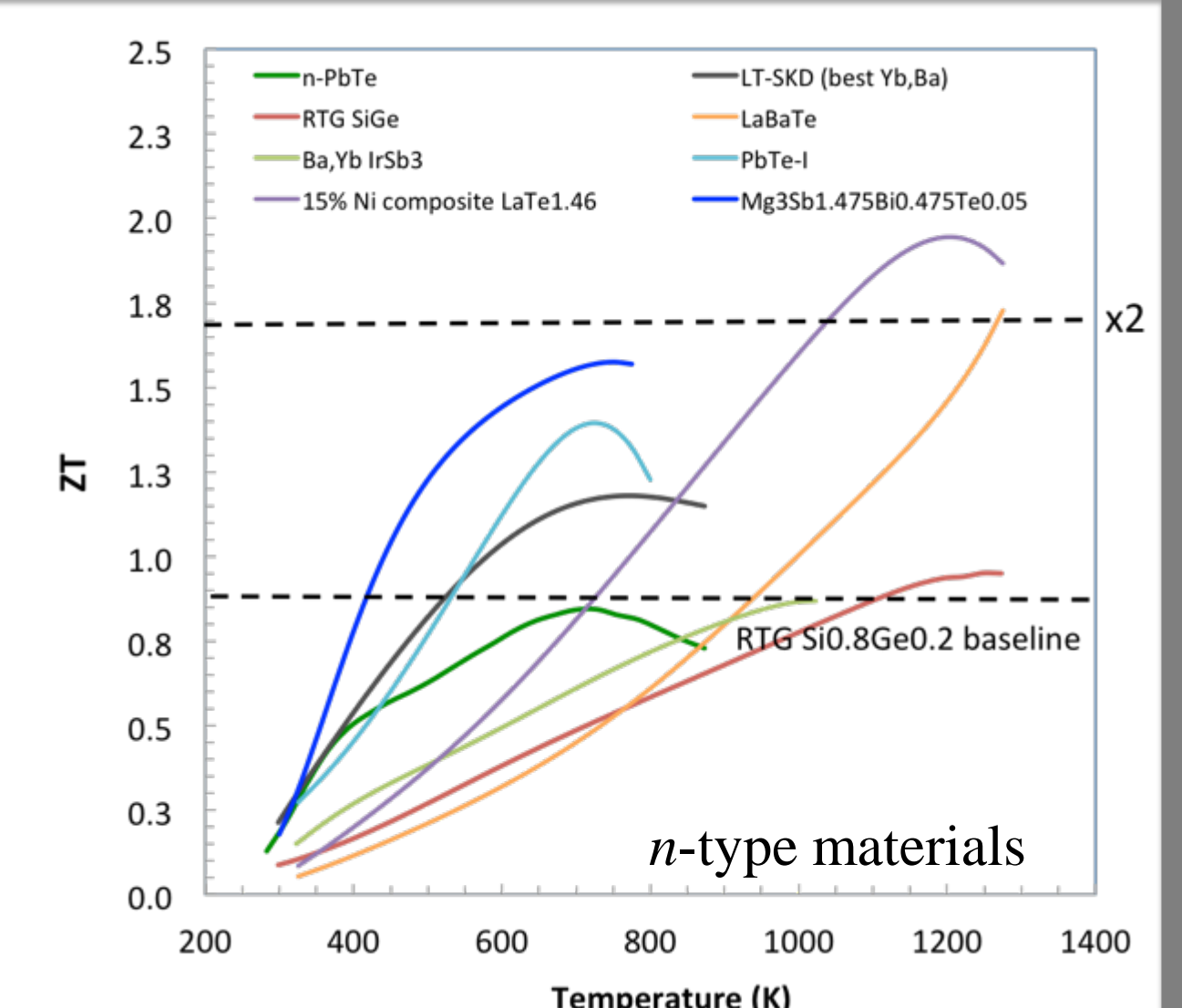
- Transport properties of a series of Te-doped  $\text{Mg}_{3+x}\text{Sb}_{2-y}\text{Bi}_y$  samples

## Conclusions

- $\text{Mg}_3\text{Sb}_{2-x}\text{Bi}_x\text{Te}_{0.05}$  shows promising transport properties at low temperature with a peak  $ZT$  of 1.6 @ 773 K
- Exhibits low sublimation rate

## Benefits to NASA and JPL

- Low temperature properties are better than those of state-of-the-art materials
- Segmented couples could lead to higher efficiencies across the full temperature range
- More capable RTGs in support of future science and exploration space missions
- Effective use of limited heat source inventory



## Acknowledgements

Thank you to Greg Gerig and George Nakatsukasa for assistance with Seebeck and thermal diffusivity measurements. Thank you to Penn State for their CALPHAD calculations of CTE and Samad Firdosy for assistance measuring the temperature-dependent CTE. This work supported by the NASA Science Missions Directorate's Radioisotope Power Systems Thermoelectric Technology Development Program. This work was performed at the California Institute of Technology/Jet Propulsion Laboratory under contract with the National Aeronautics and Space Administration.

# Fielding an Astrobiology Payload on the LEMUR Rock-Climbing Robot

Kyle Uckert (347C)

Aaron Parness (347C), Rohit Bhartia (3225), David Flannery (3225)

## Introduction:

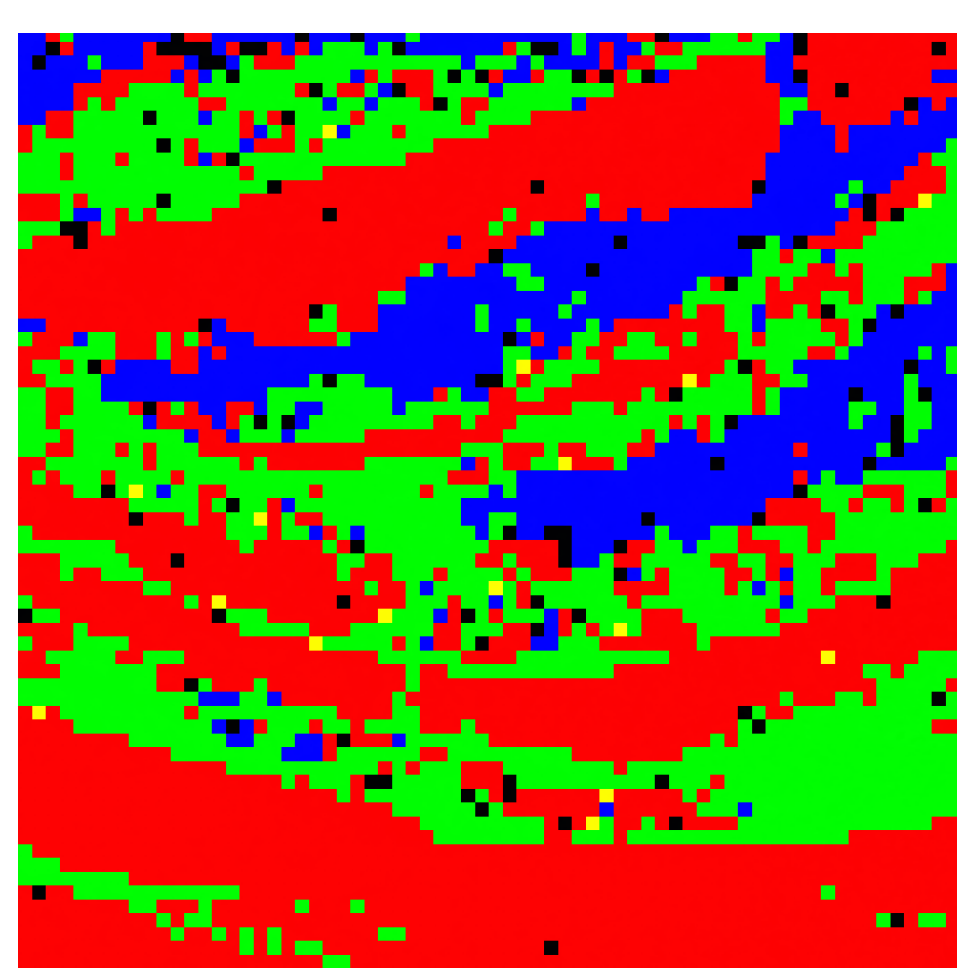
Planetary caves are desirable destinations for future robotic astrobiology exploration. A rock-climbing robot equipped with a suite of *in situ* instruments designed to identify biosignatures and characterize subsurface mineralogy is ideally suited to reveal the presence of extant or extinct microorganisms.

## Objectives:

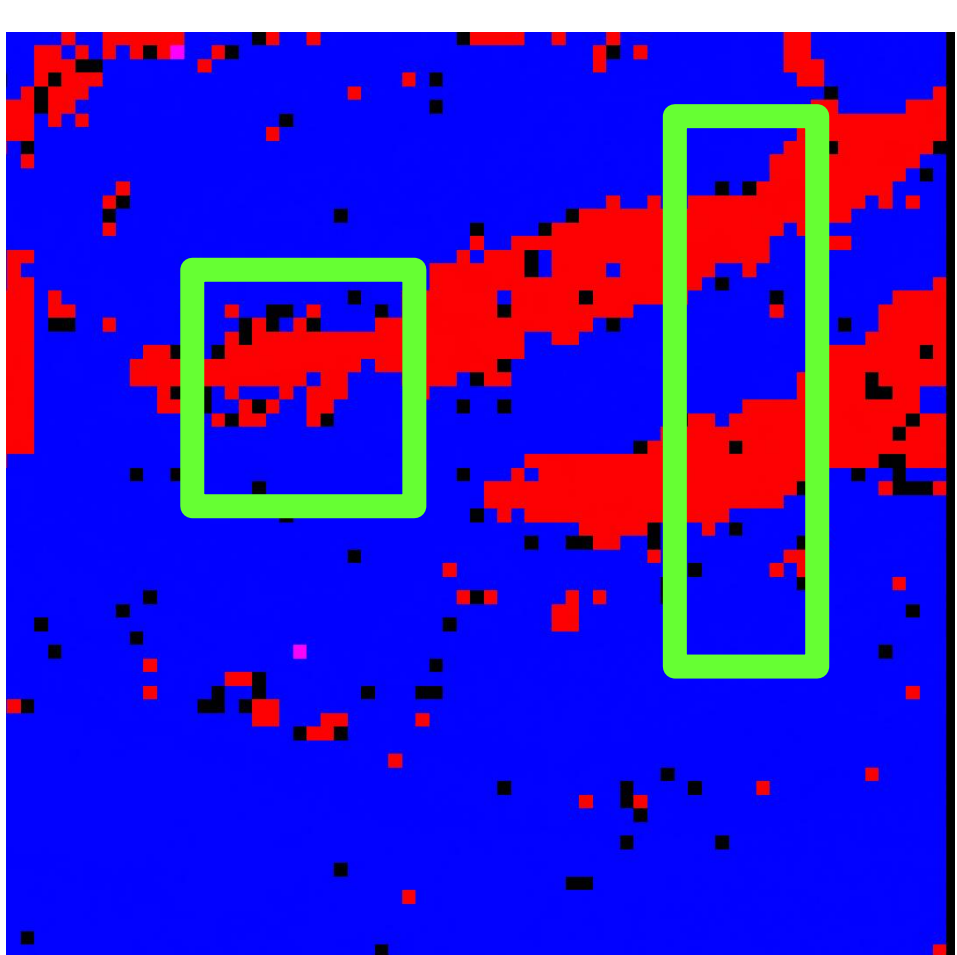
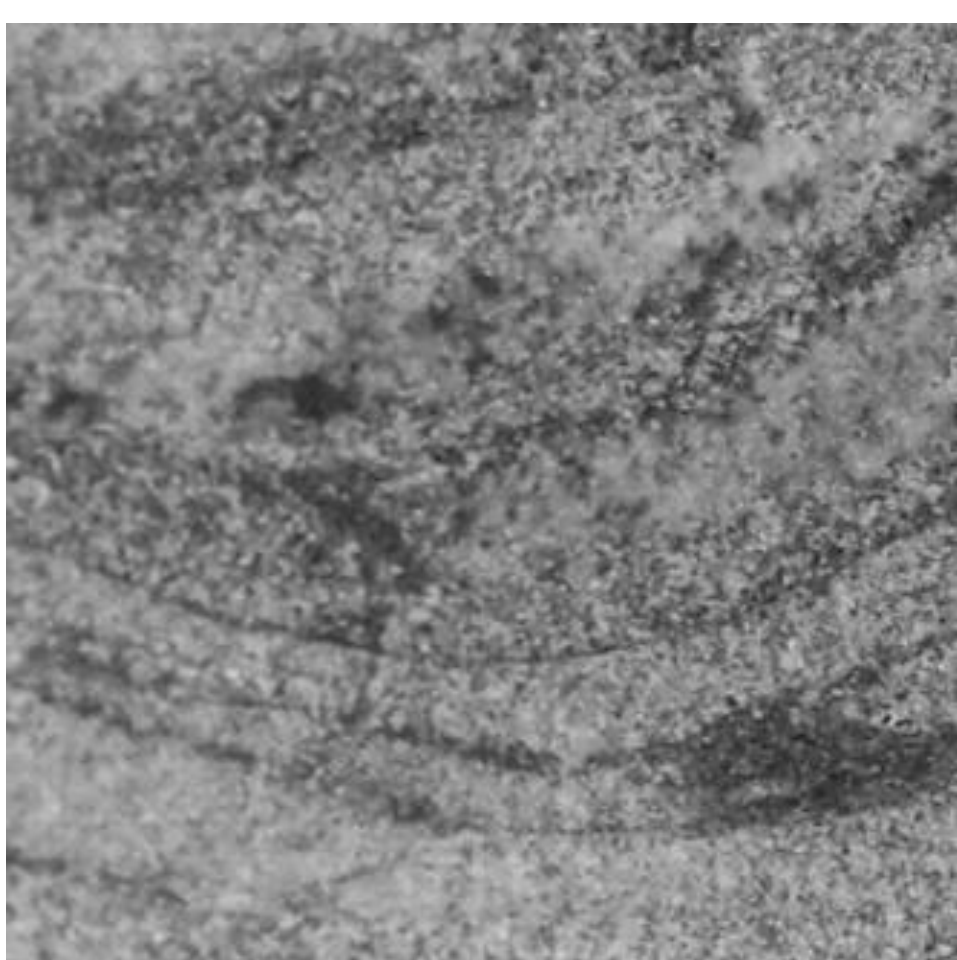
- Develop a suite of instruments to detect biosignatures in extreme, extraterrestrial environments.
- Define field operation procedures to autonomously and rapidly identify biosignature candidates while minimizing data acquisition time.
- Characterize the mineralogy and spatial distribution of organics associated with biovermiculation patterns and stromatolites *in situ*.

## GURILA:

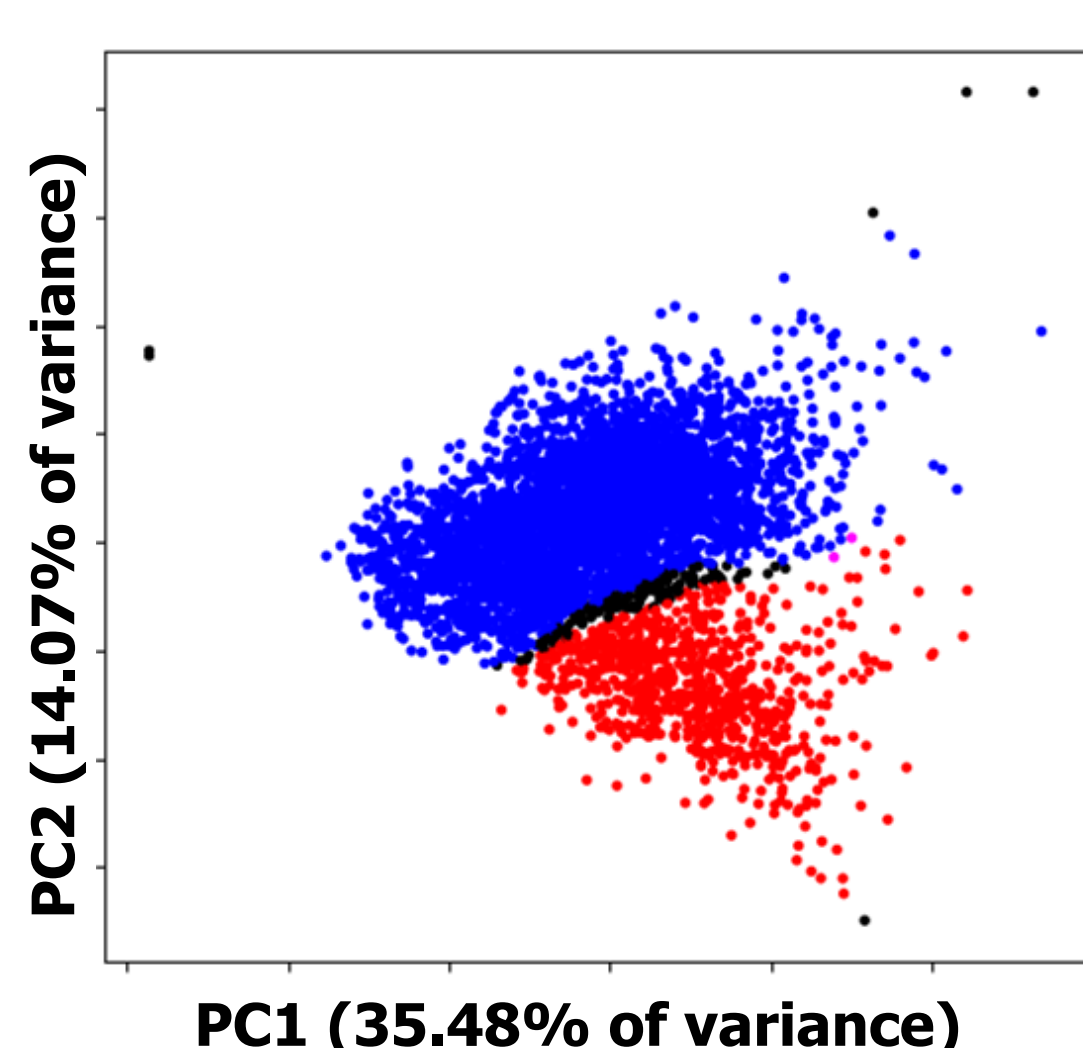
- GURILA (a deep-UV Raman spectrometer) reveals the organic and major mineralogical components of a sample via fluorescence and Raman scattering induced by a 248.6 nm laser.
- GURILA is based on the SHERLOC design to fly on the Mars 2020 Rover.



Left: Anticipated GURILA data product – Raman hyperspectral map of Strelly pool formation (top) with context photo (top). **dolomite, organics, and chert concentrations highlighted.**



Anticipated ROI selection dataset: **ROI selection of the Strelly Pool sample from the PCA of a fluorescence dataset. PC2 is dominated by the position of the 253 cm<sup>-1</sup> Raman peak.**

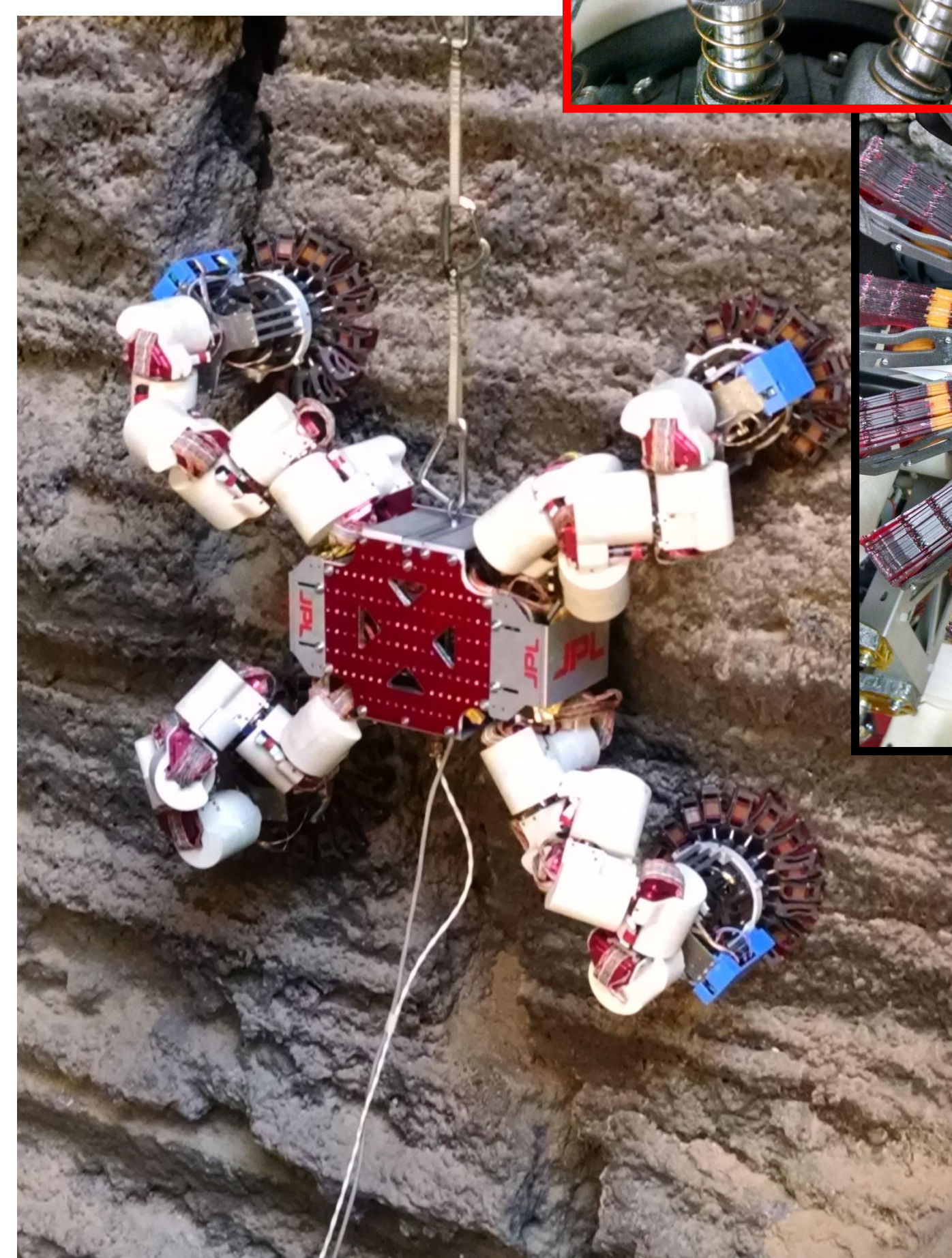


PC2 (14.07% of variance)

PC1 (35.48% of variance)



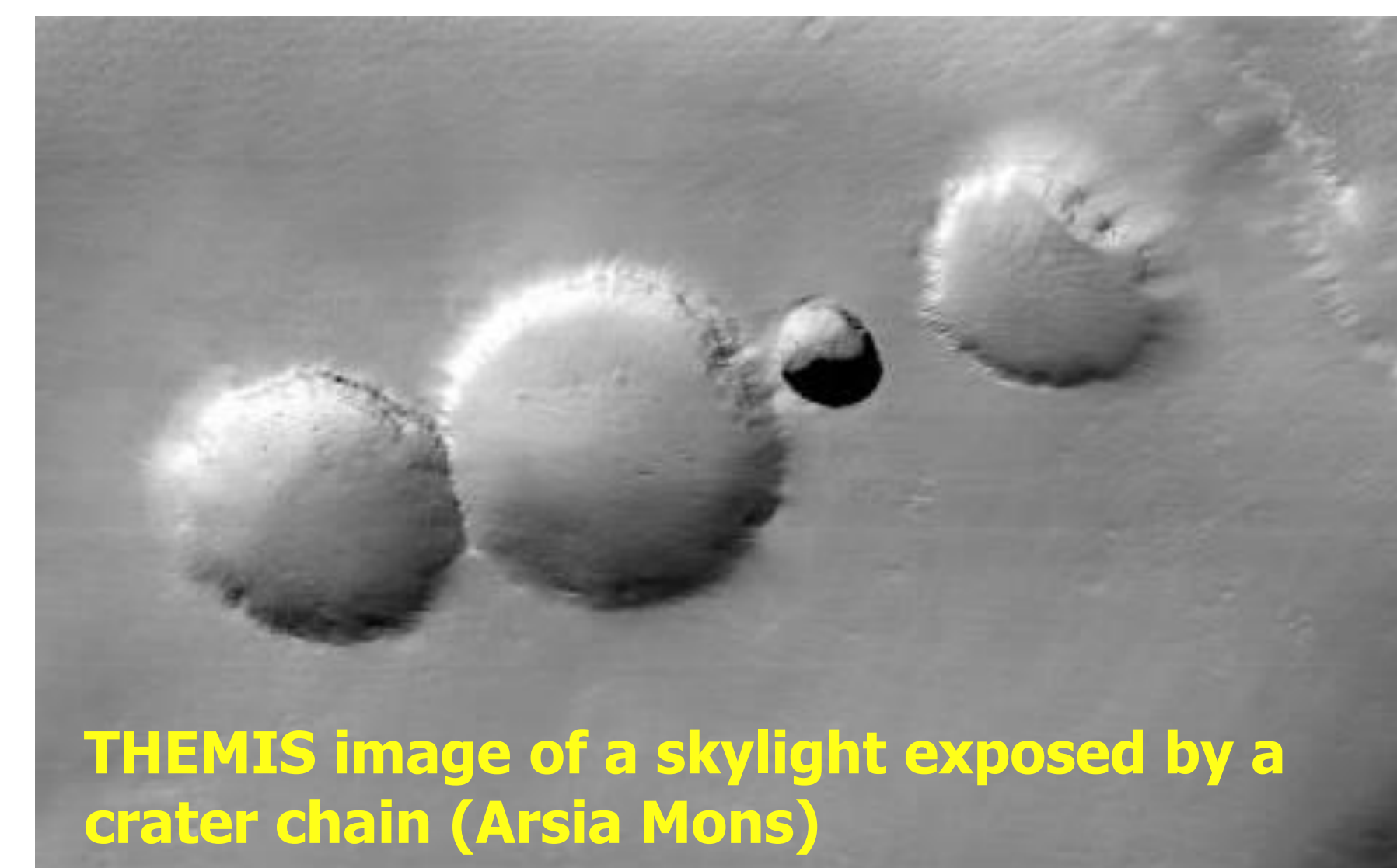
Left: Microspine gripper end effector. Only ~10% of microspines need to grip for a successful anchor.



Above: LEMUR climbing a wall in Big Skylight Cave (El Malpais, NM) September 2015.

## Field Operations:

- Autonomously identify regions-of-interest (ROI) for detailed follow-up measurements based on rapid, low-resolution fluorescence scans.
- ROIs are optimized to contain spectral variance.
- Data Product:** hyperspectral maps of the organic and major mineralogical composition (up to 5x5 cm at 100 μm resolution)



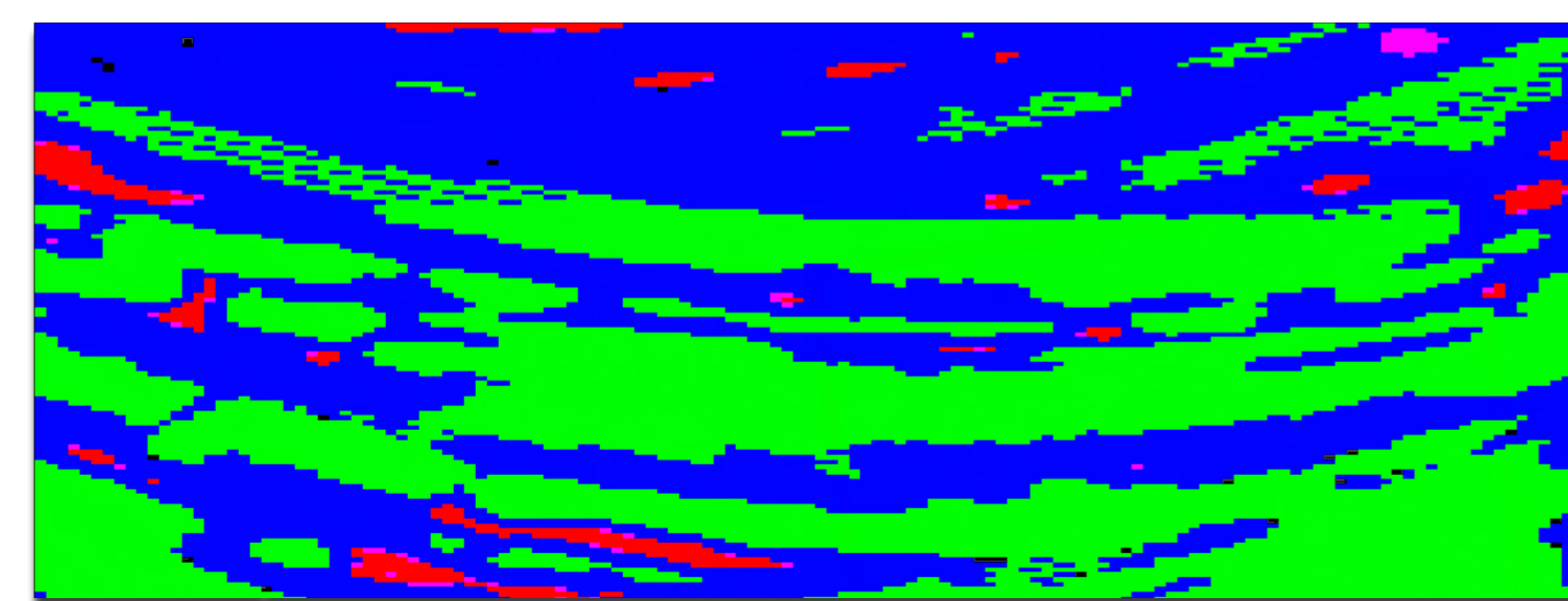
THEMIS image of a skylight exposed by a crater chain (Arsia Mons)

## LEMUR:

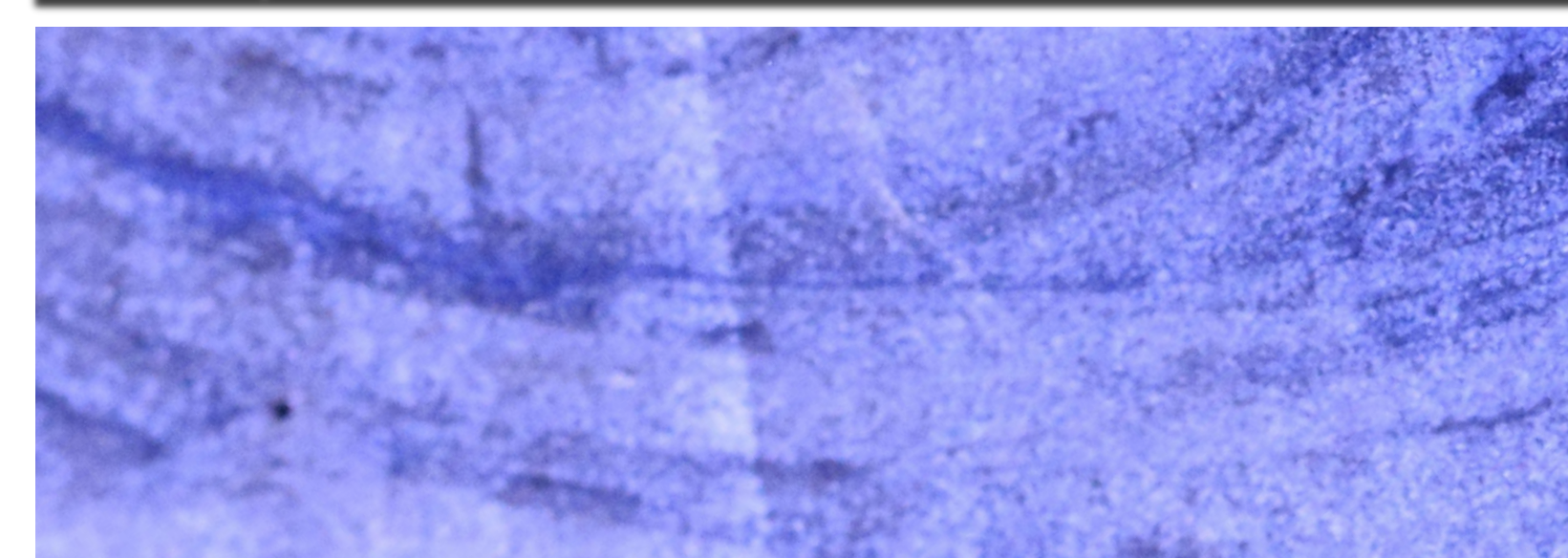
- Each of LEMUR's limbs has 7 degrees of freedom and hundreds of sharp microspine hooks that anchor itself to floors walls and ceilings of caves and cliff faces.
- Deployed successfully in basaltic environments, including the El Malpais lava tubes (NM) and Pisgah Crater (CA).

## APE:

- APE (an X-Ray Fluorescence (XRF) spectrometer) reveals the elemental composition of a sample through the detection of characteristic X-rays emitted from atoms exposed to a high-energy X-Ray source.
- APE is based on the PIXL design to fly on the Mars 2020 Rover.



Anticipated APE data product - XRF hyperspectral map of Strelly pool formation (top) with context photo (bottom). **Ti, Si, and Ca concentration highlighted.**



## Conclusions:

- XRF and Raman spectroscopy may effectively identify biosignatures associated with the presence of organics in field samples and potentially the products of biomineralization.
- A robotic platform such as LEMUR is necessary to access scientifically interesting targets in extreme environments with challenging terrain.
- A demonstration of rapid data acquisition procedures using multivariate statistical techniques to autonomously select ROIs may help inform Mars 2020 operation procedures.
- A field demonstration of GURILA and APE will take place in October 2017 (El Malpais lava tube) and February 2018 (Mojave Desert).

# High-efficiency, low-noise UV superconducting nanowire single-photon detectors



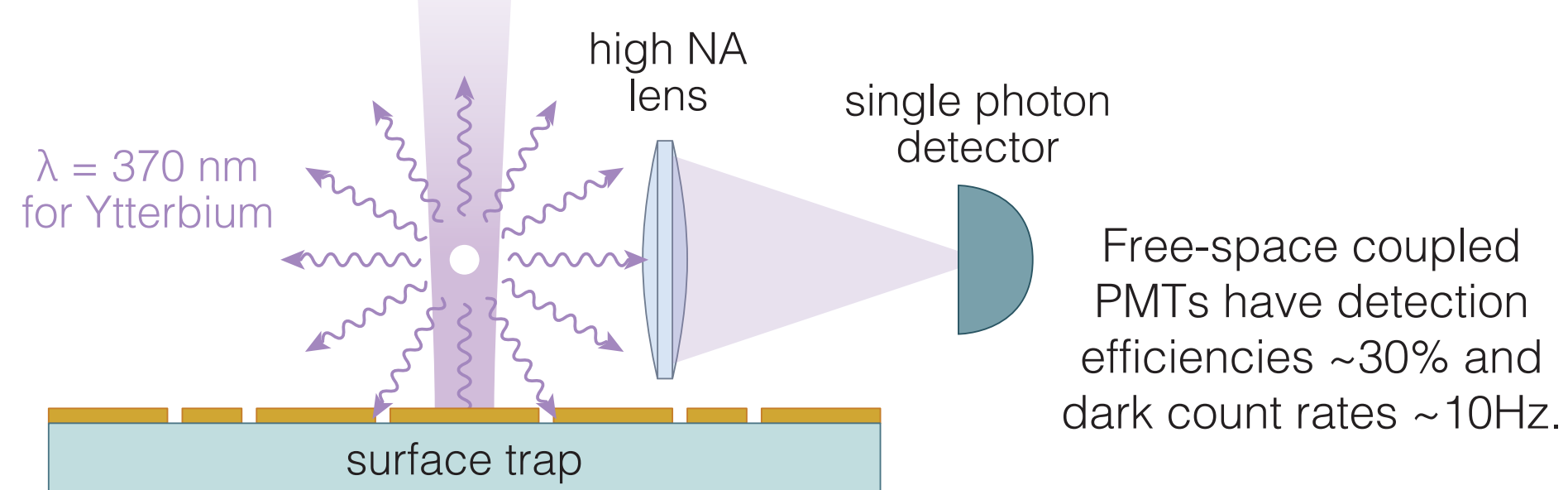
E. E. Wollman (389I), A. D. Beyer (389I), R. M. Briggs (389K), F. Marsili (389I), M. D. Shaw (389I)  
Jet Propulsion Laboratory, California Institute of Technology



V. B. Verma, R. P. Mirin, S. W. Nam  
National Institute of Standards & Technology

## Objectives

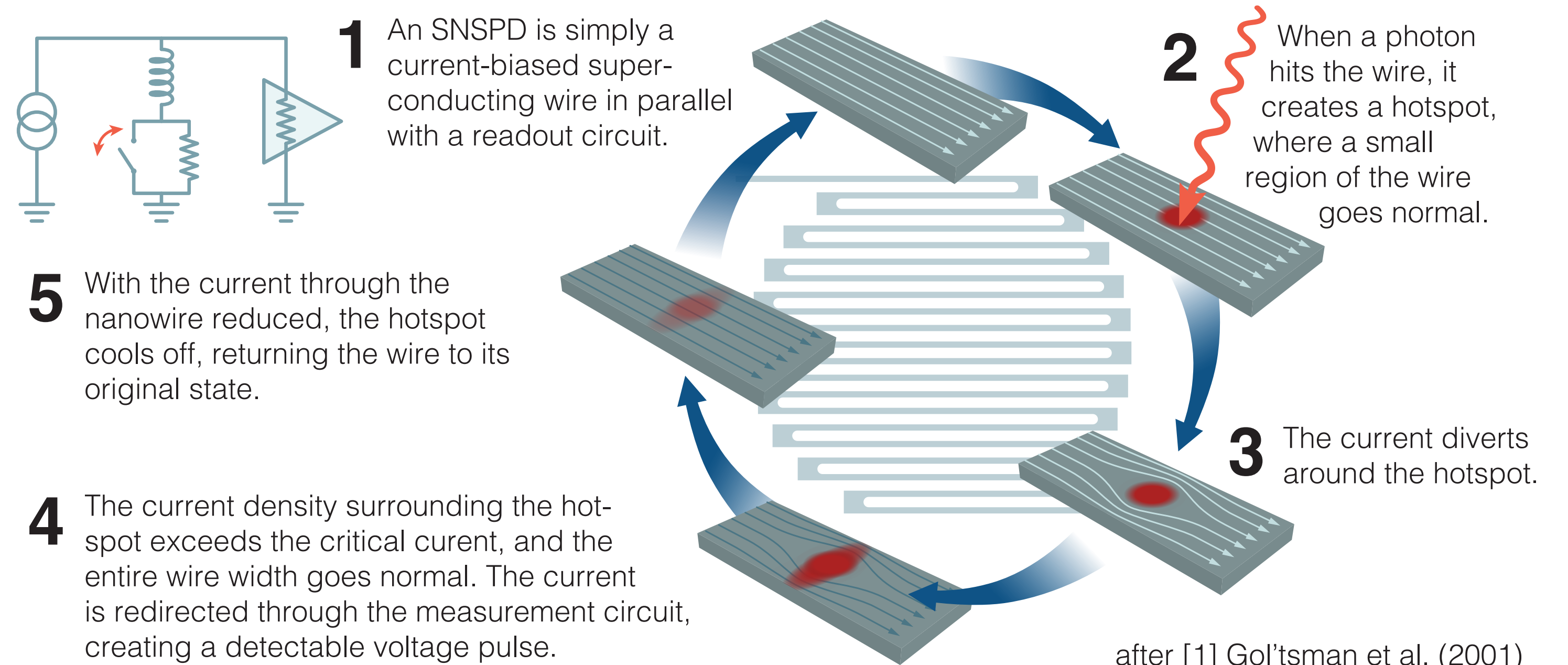
Trapped ion qubits have long coherence times and high fidelities. Qubit readout via state-dependent fluorescence is slow, however, due to inefficiencies in photon detection. SNSPDs could improve measurement time by an order of magnitude.



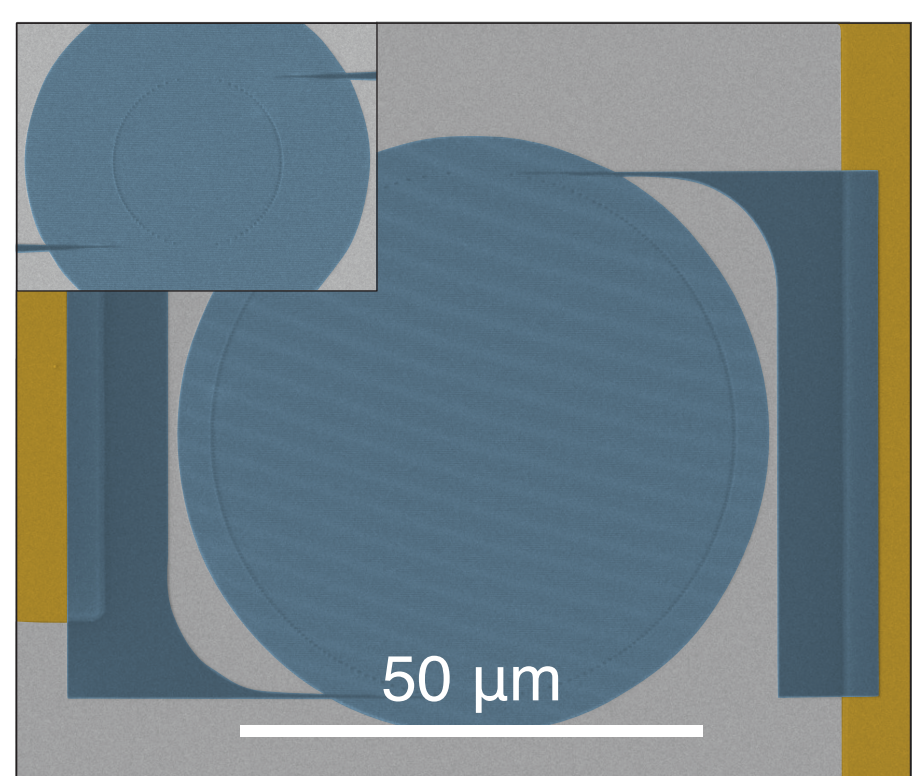
### Requirements for Ytterbium ion trap detectors:

- High efficiency at 370 nm
- Low dark count rates
- Compatible with cryocoolers running above 3 K

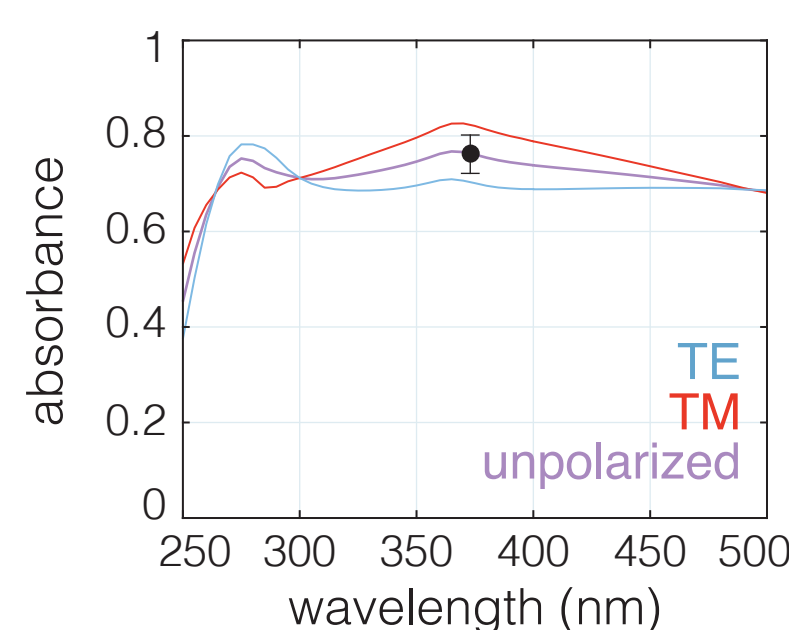
## What is an SNSPD?



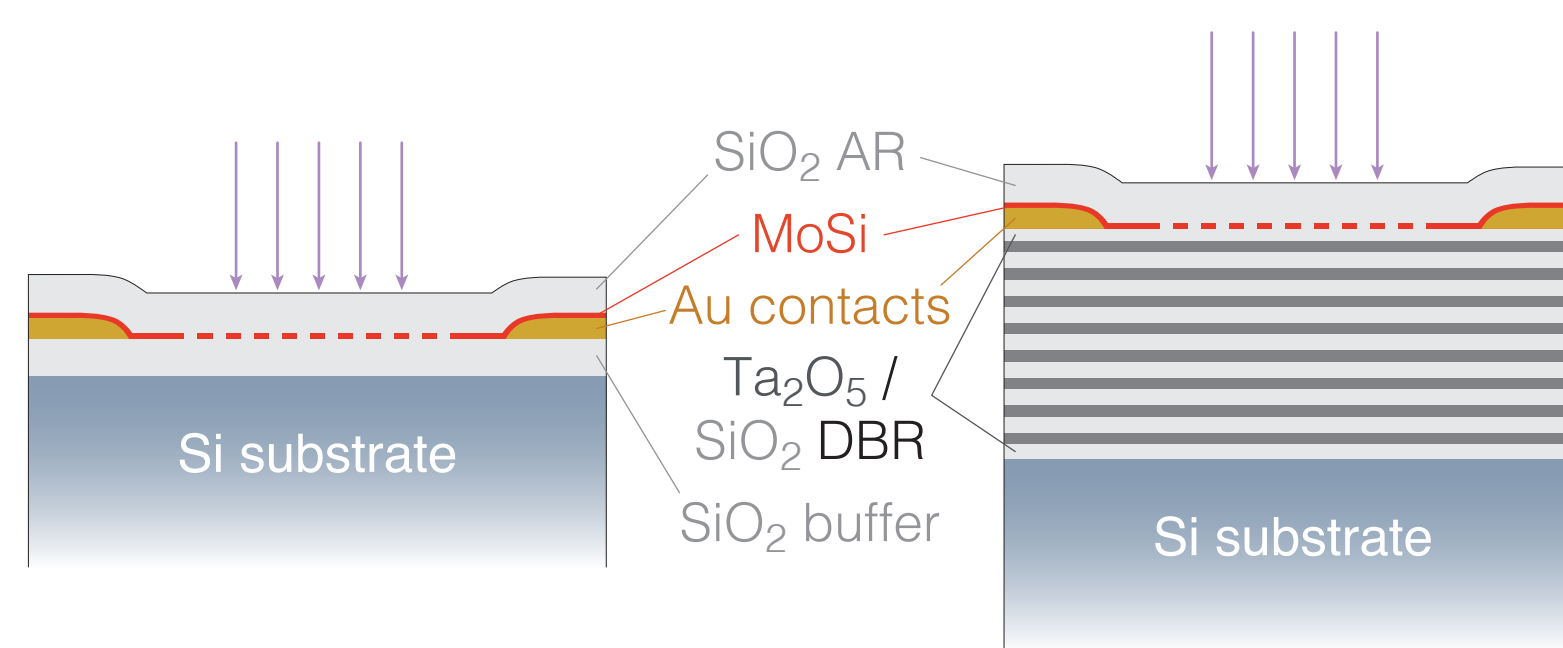
## Design & fabrication



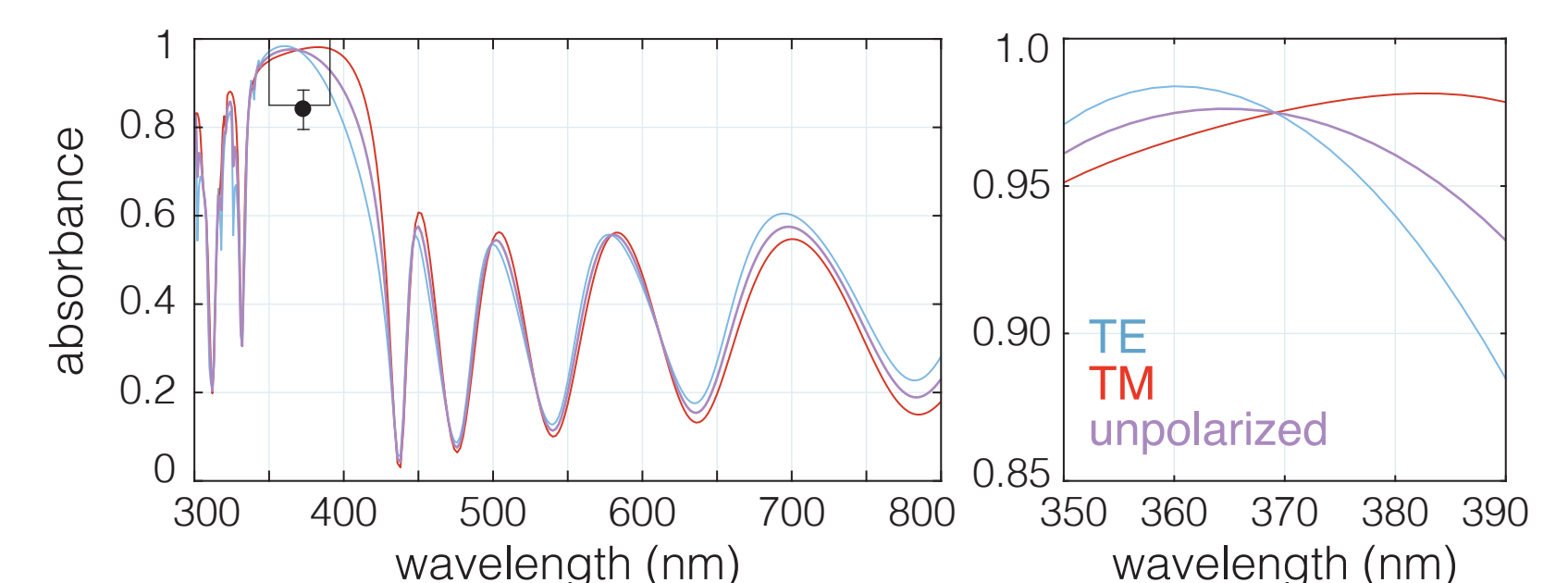
SEMs showing SNSPDs with 56  $\mu\text{m}$  or 16  $\mu\text{m}$  diameters for coupling to 50  $\mu\text{m}$  or 10  $\mu\text{m}$  core fiber.



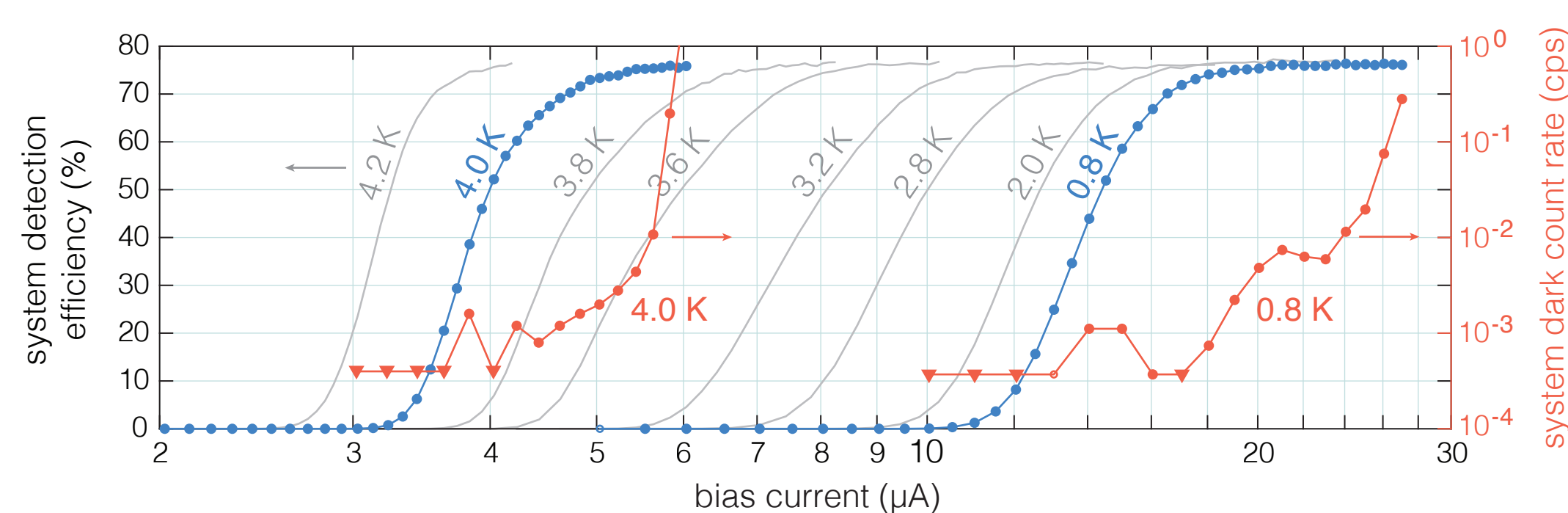
Modeled absorption (left) for a simple stack (right) consisting of a MoSi nanowire layer embedded in SiO<sub>2</sub>. The SiO<sub>2</sub> thickness is optimized for > 70% absorption into the nanowire layer for unpolarized light at wavelengths from 275 nm to 450 nm.



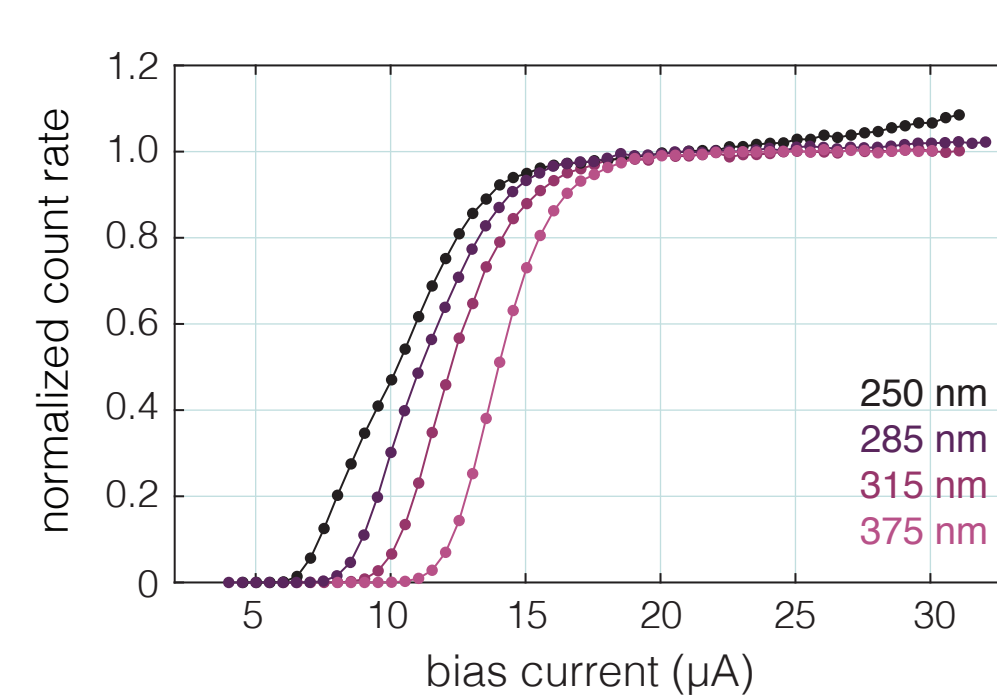
Stack design (left) and modeled absorption into the nanowire layer (right) for enhanced efficiency at 370 nm. A distributed Bragg reflector (DBR) prevents light from being transmitted into the substrate. At 370 nm, the absorption should be > 95%, with little dependence on polarization.



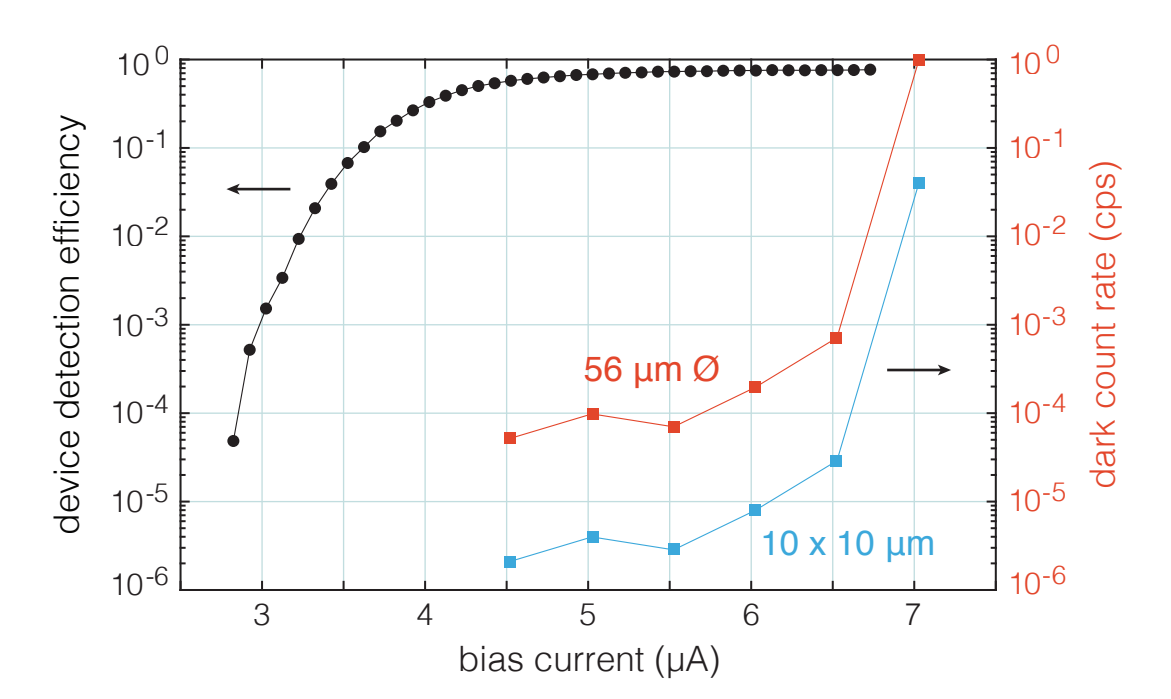
## Performance: efficiency & dark counts



Left axis, gray and blue data: system detection efficiency vs. bias current at different temperatures for a narrowband device. For all temperatures, the SDE reached  $\sim 76\%$ . Taking into account losses in the fiber, this corresponds to an efficiency of  $\sim 84\%$  at the device. Right axis, red data: system dark count rate vs. bias current at 800 mK and at 4.0 K.

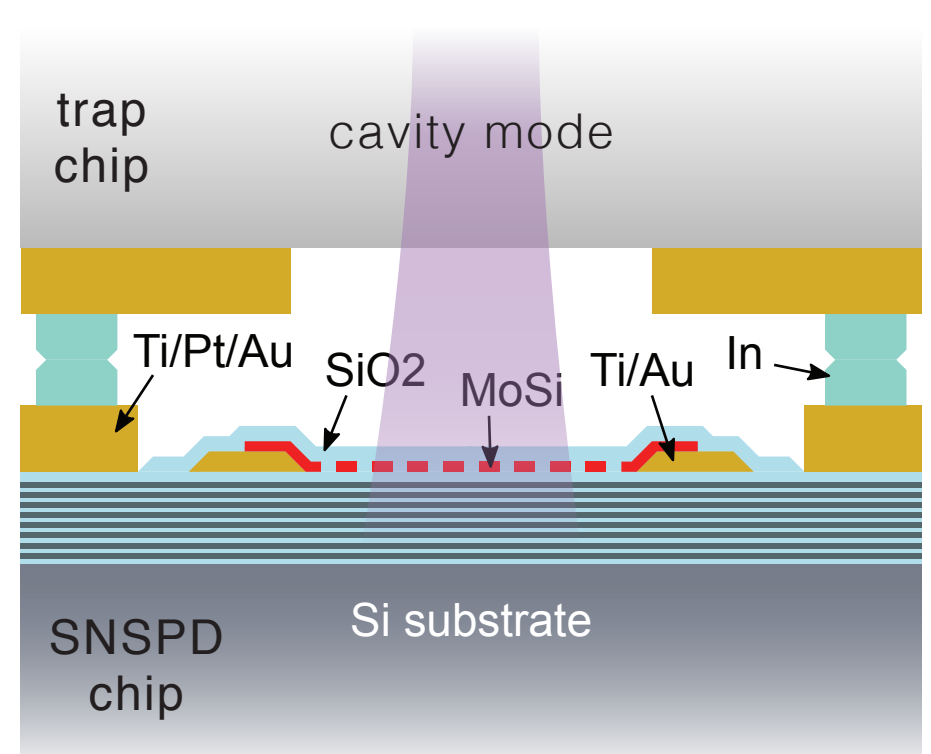


Normalized count rate vs. bias for a broadband device measured at 800 mK. Data were taken with LEDs at 250 nm, 285 nm, and 315 nm, and with a laser diode at 373 nm. The device detection efficiency was found to be  $\sim 75\%$  at 373 nm.

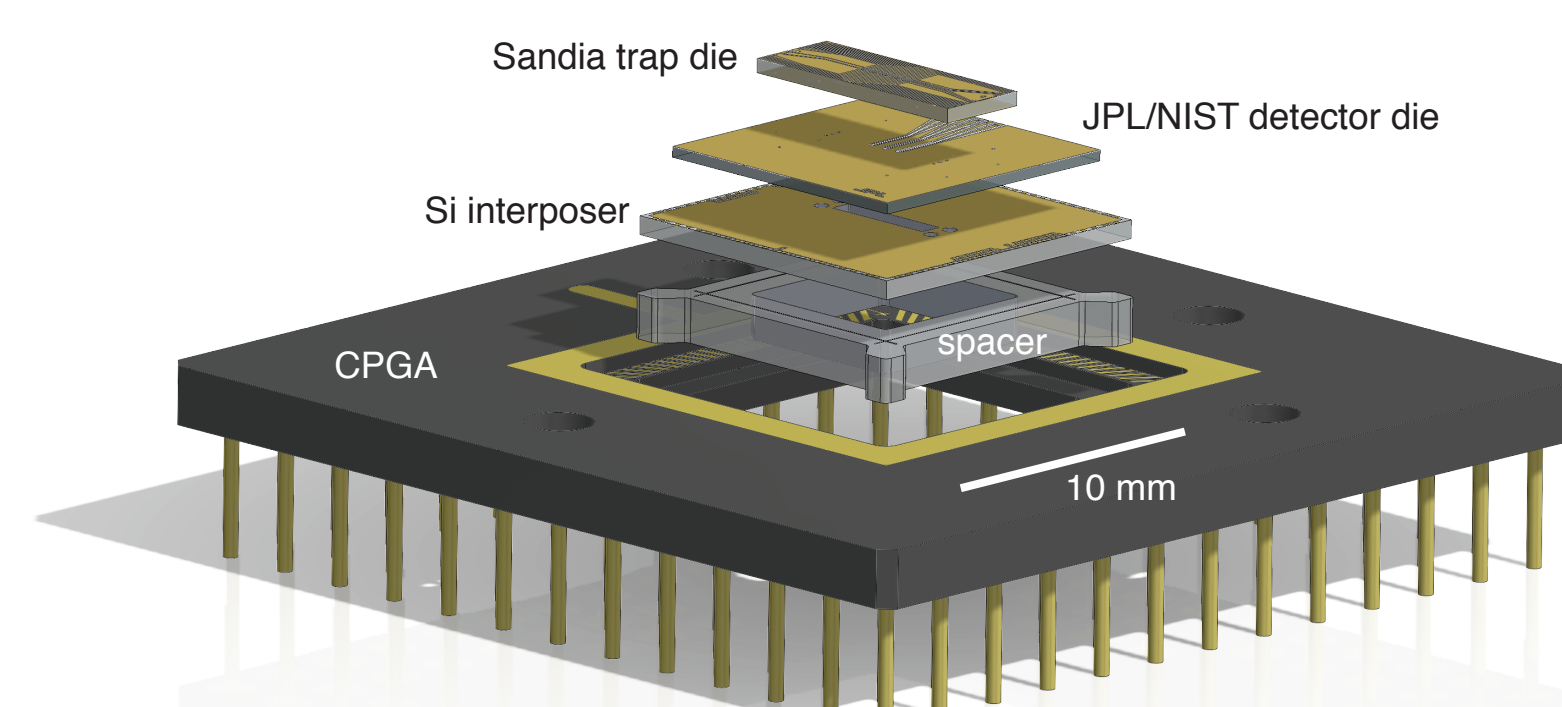


Intrinsic dark count rate for a large active-area, broadband device at 4 K. If scaled for a 10 x 10  $\mu\text{m}$  pixel, dark counts are on the order of 1 count every 100 hours.

## Integration



SNSPDs have previously been integrated directly on an ion trap chip [2], but pickup from the RF trapping field can be an issue. We are instead bonding the individual trap chips to detector chips so that the SNSPDs can have greater physical separation from the RF electrodes and can be placed behind a shielding ground plane on the backside of the trap chip. An optical cavity is also used to enhance emission from the ion into the cavity mode, increasing collection efficiency.



Model of the integrated trap/detector package. The trap chip is bonded to the detector chip, which is then epoxied to an interposer.

## References

- [1] Gol'tsman et al., "Picosecond superconducting single-photon optical detector," Appl. Phys. Lett. 79, 705-707 (2001).
- [2] Slichter et al., "UV-sensitive superconducting nanowire single photon detectors for integration in an ion trap," Opt. Express 25, 8705-8720 (2017).

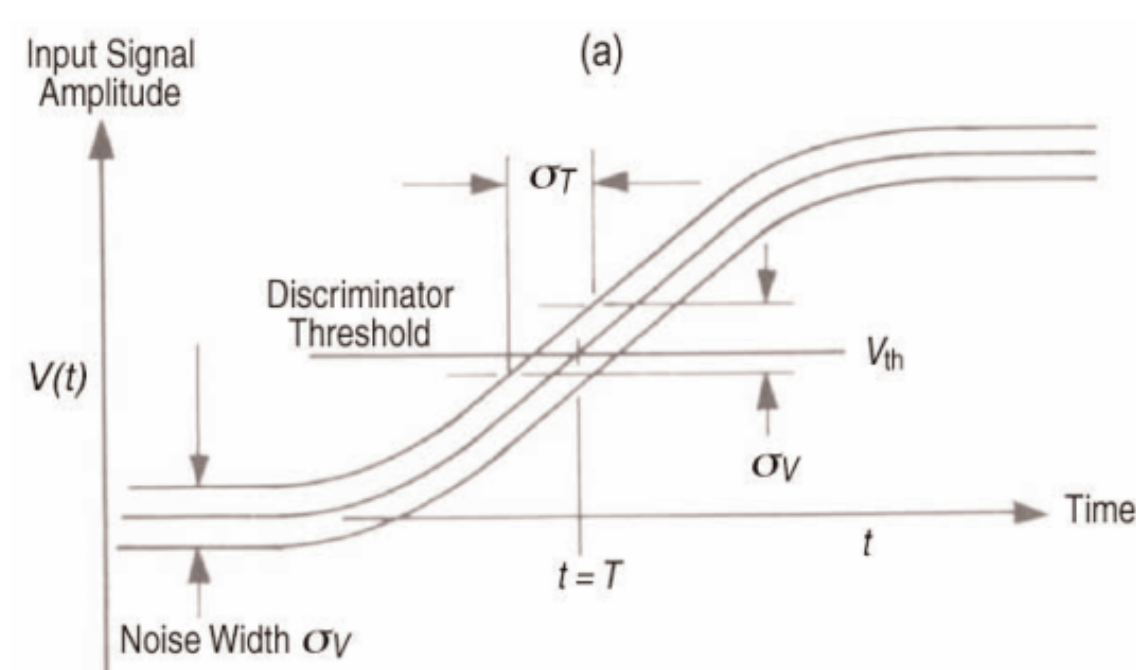
# Single photon detection with a system temporal resolution below 10 ps

Author: Boris Korzh (389I)

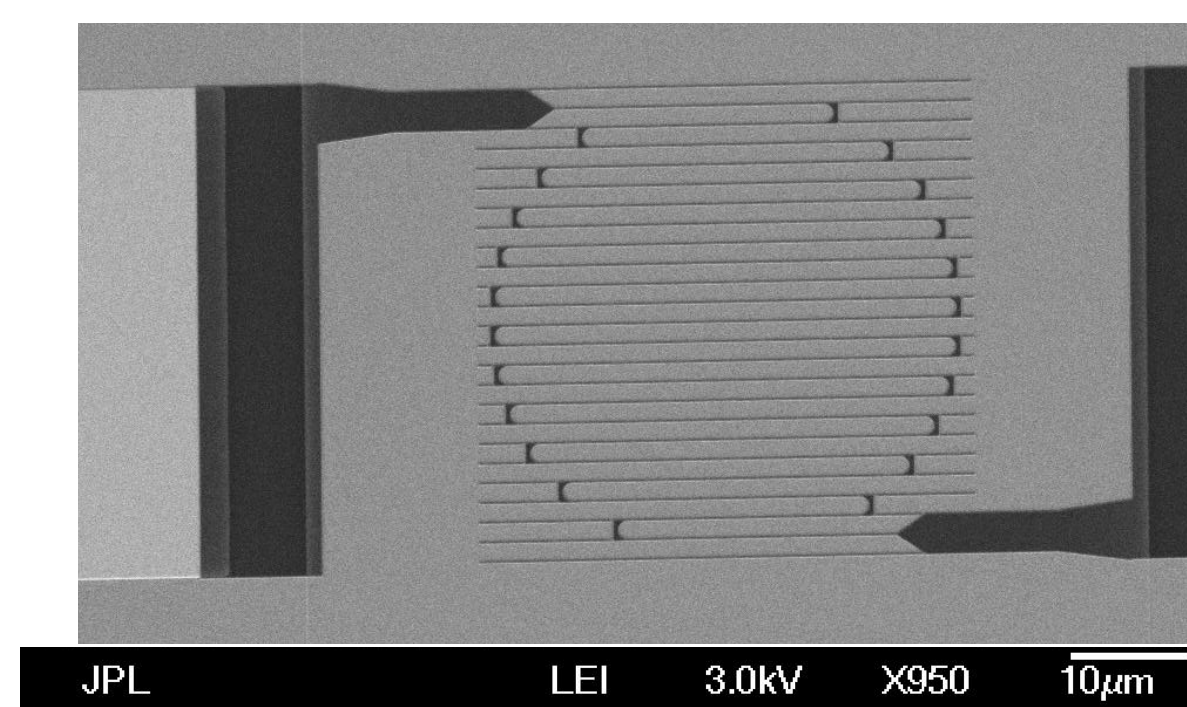
Emma Wollman (389I), Simone Frasca (389I) and Matt Shaw (389I)

## Introduction

Detecting the arrival time of single photons is a critical requirement of many applications such as deep space optical communication, biological imaging, spectroscopy, laser ranging, astronomical observation as well as quantum communication and information processing. Among the various single photon detector technologies, superconducting nanowire single photon detectors (SNSPDs) have demonstrated the lowest temporal resolution as low as 15 ps, however the fundamental limits are still poorly understood. SNSPDs form a long meandering nanowire, which leads to a delay of the readout signal, dependent on the position of the photon absorption. This is known as the geometric jitter, and it can become the dominant effect, especially for large area devices. The second contribution is the noise induced jitter, arising due to a finite slew rate of the readout signal and the presence of electrical noise. We have taken a big step towards approaching the intrinsic jitter in SNSPDs through the use cryogenic amplification and a reduction of the geometric jitter through the fabrication of very short nanowires.



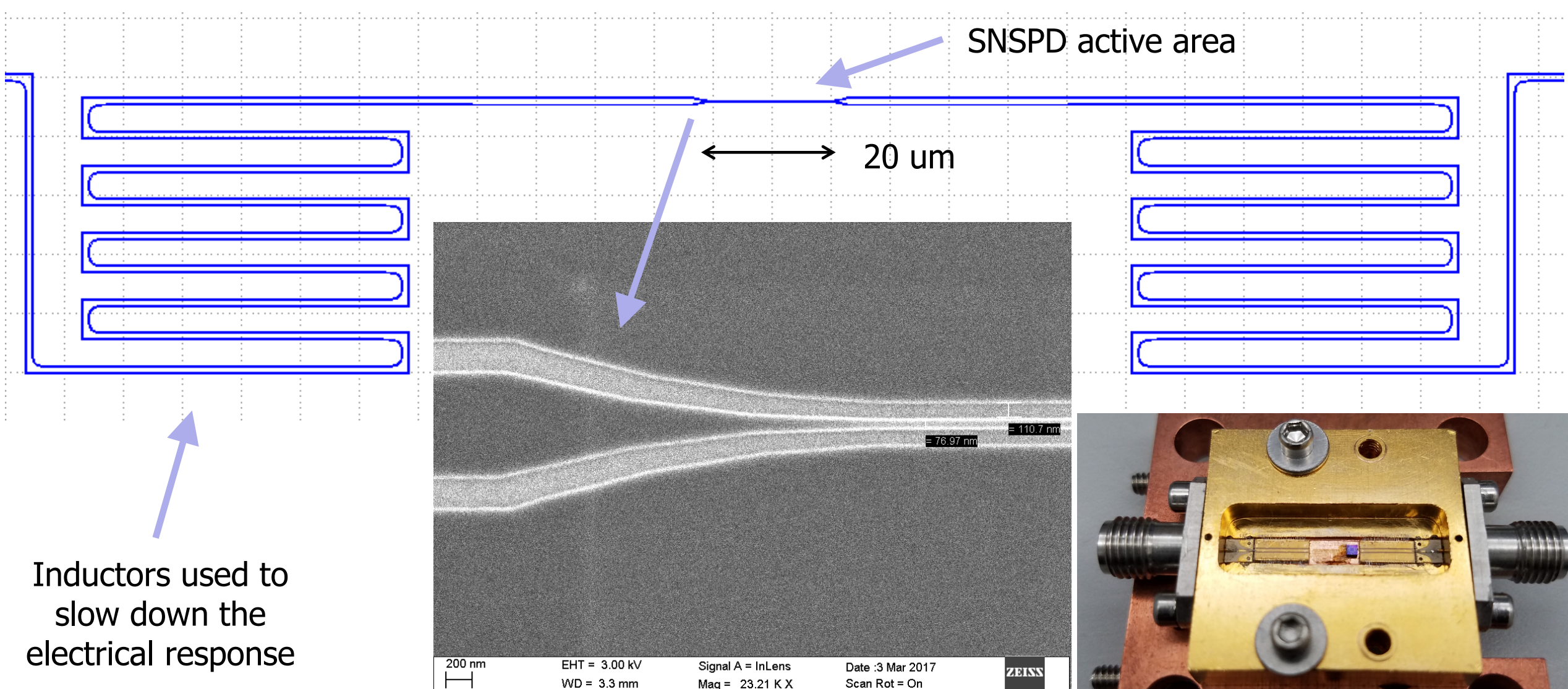
Noise contribution to jitter



Typical SNSPD with long nanowire

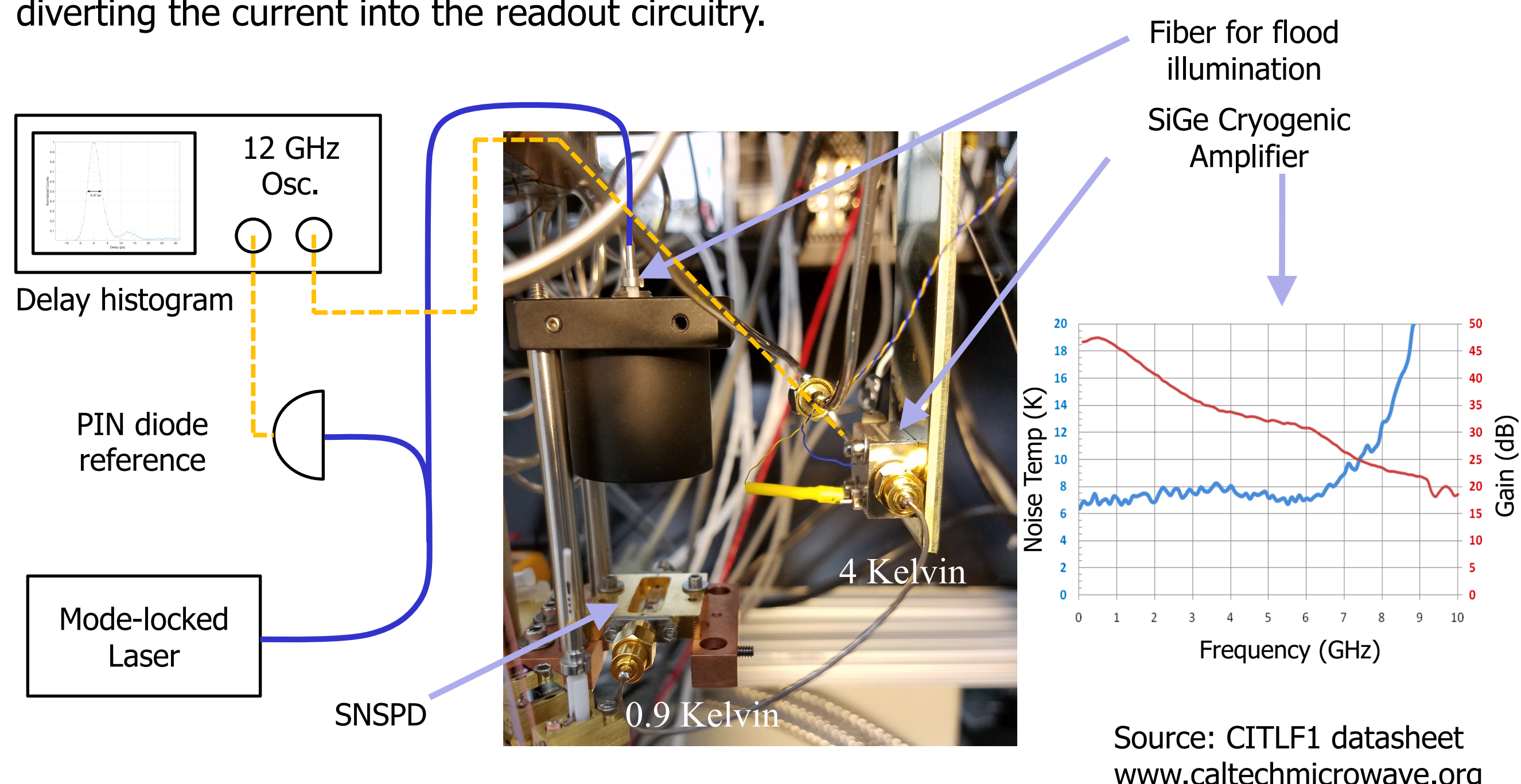
## Setup

Study of the intrinsic temporal jitter requires the reduction of the two dominant effects, noise jitter and geometric jitter. By using a differential readout scheme it is possible to eliminate the geometric effect, however, single ended readout was chosen for simplicity and noise reduction. A short nanowire was fabricated to minimize geometric jitter, which is expected to contribute approximately 3-4 ps to overall jitter.



Inductors used to slow down the electrical response

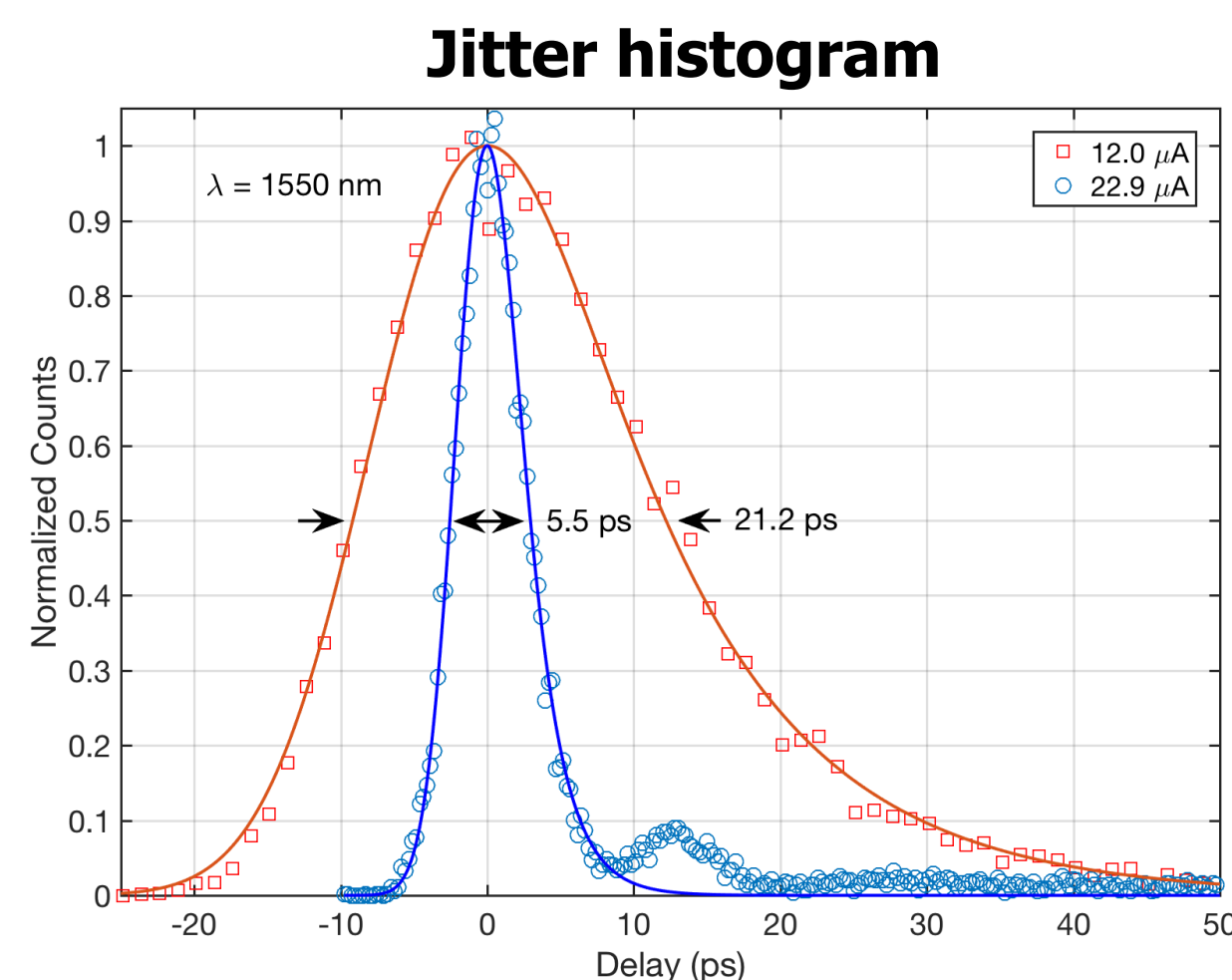
The nanowire is current biased and upon the absorption of a single photon it becomes resistive across the full cross-section, rapidly expanding along the length of the nanowire, diverting the current into the readout circuitry.



Source: CITLF1 datasheet  
www.caltechmicrowave.org

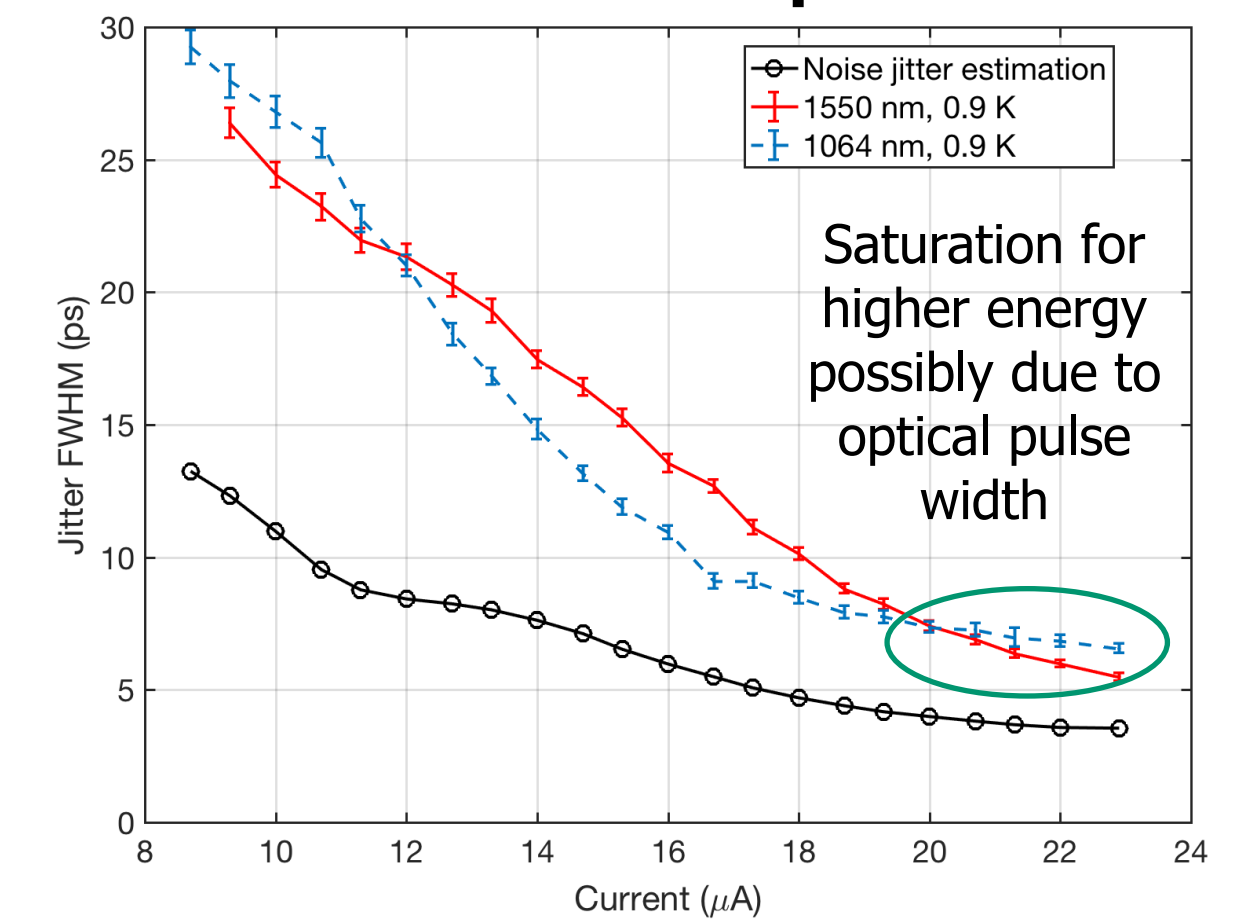
## Results

A record low jitter of **5.5 ps full-width at half maximum** was measured for 1550 nm photons, which is a factor of 3 lower than the previous record. The jitter was not dominated by the electrical noise or geometric effects, indicating that we were able to measure the intrinsic jitter of an SNSPD for the first time.



- Expect to be approaching the geometric jitter limit.
- Jitter reduces for higher energy detections.
- High energy detections possibly limited by width of pulse at shortest timescales.
  - Could reduce with access to a fast visible laser and free-space coupled cryostat.
- Nanowire shows saturation plateau for both wavelengths.
  - High quality nanowires.
  - Maximum internal efficiency.
- Temperature dependence is an additional indicator of intrinsic jitter mechanism.
- Future work will shift to even shorter wavelengths and free space coupling to minimize dispersion.
- Nanowire width dependence will be important parameter to study.

## Jitter current dependence



Saturation for higher energy possibly due to optical pulse width

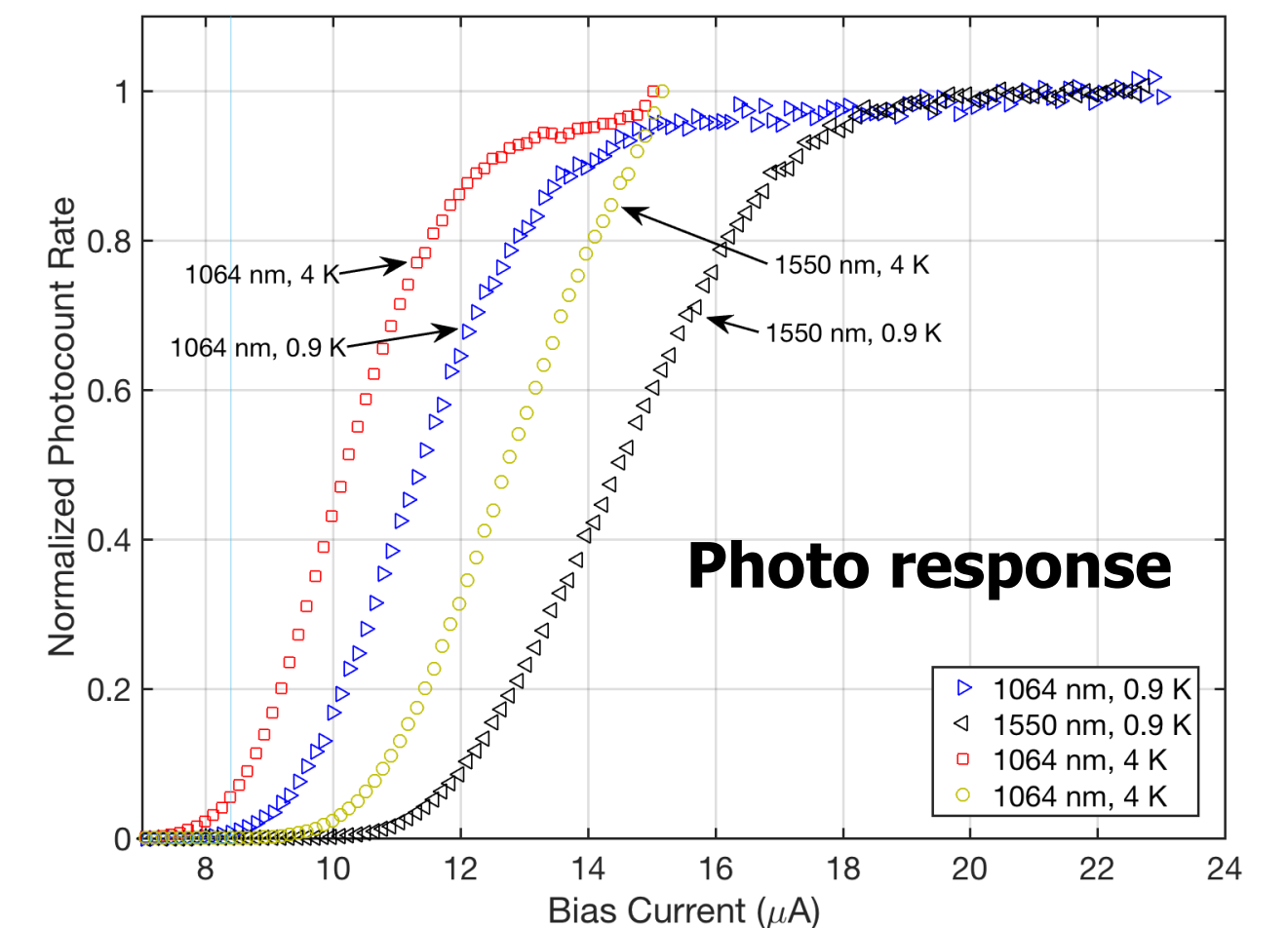
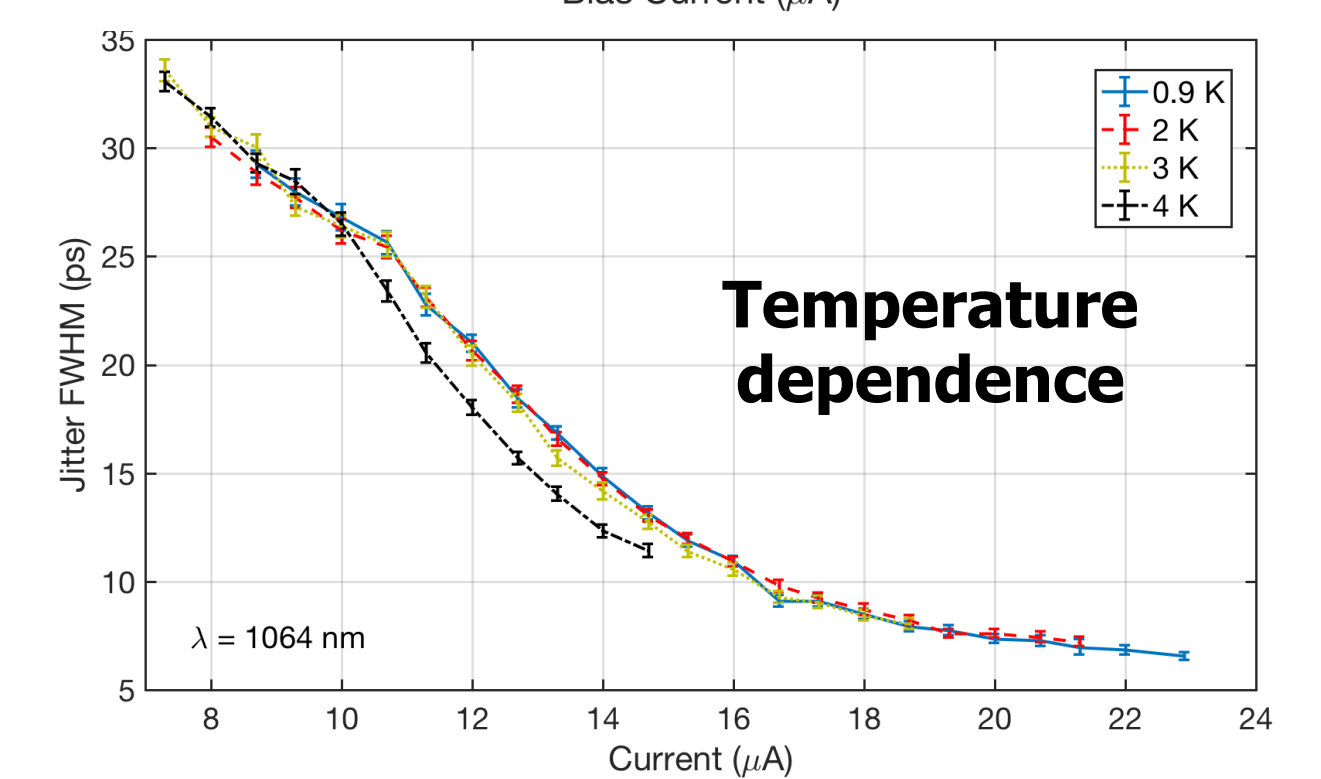


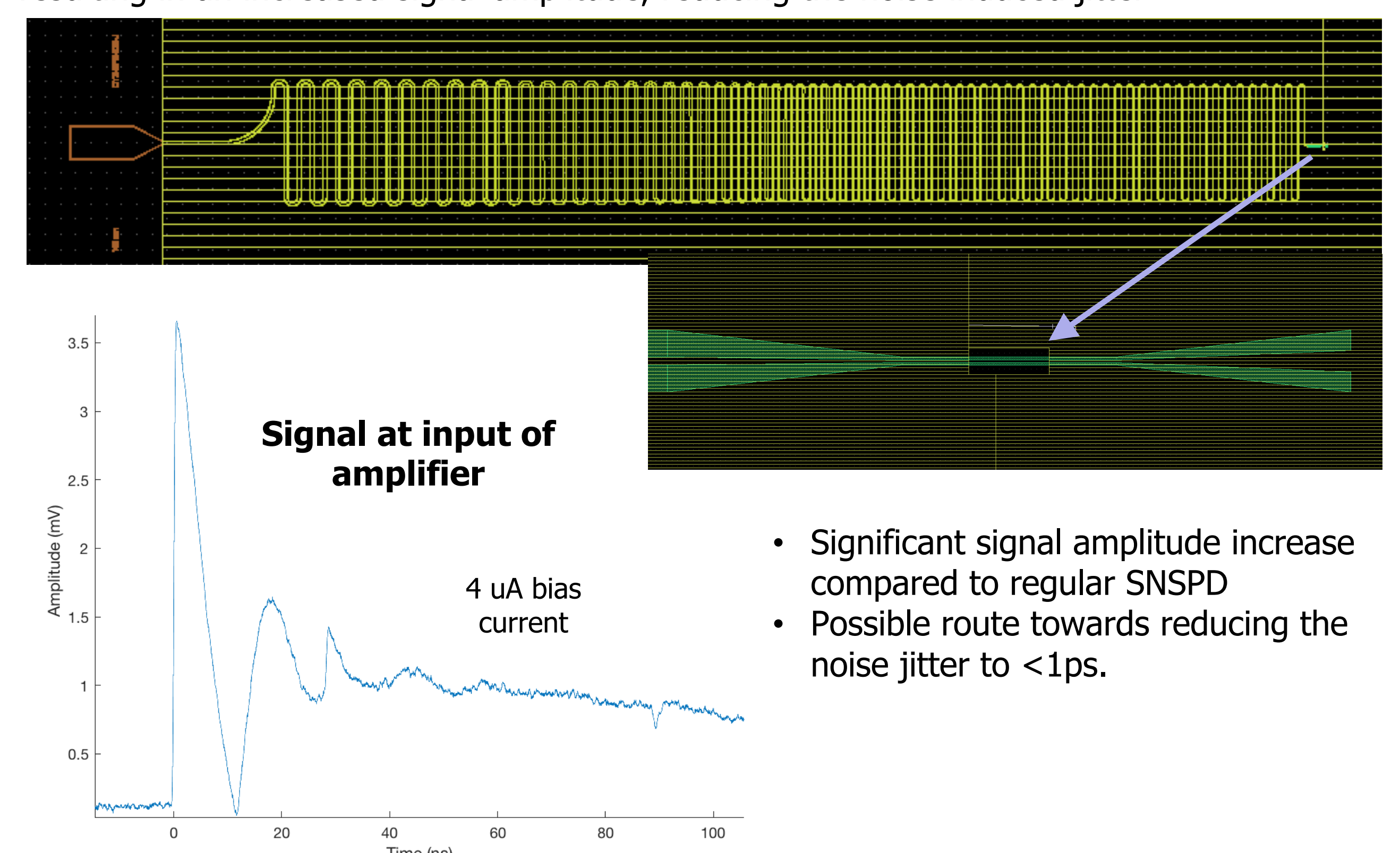
## Photo response



## Temperature dependence

## Outlook

During the detection in SNSPDs, the hotspot resistance is on the order of kilo Ohms, meaning that interfacing to a 50 Ohm transmission line and amplifier results in a large portion of the signal power to be lost. We are developing a low jitter SNSPD with an impedance matching taper, which efficiently transfers the signal power to 50 Ohm, resulting in an increased signal amplitude, reducing the noise induced jitter.



- Significant signal amplitude increase compared to regular SNSPD
- Possible route towards reducing the noise jitter to <1ps.

## Acknowledgements

We thank Q-Y. Zhao, A. Dane, M. Colangelo and K. Berggren from MIT for design and fabrication of the devices and the DARPA DETECT program for support.



# Automated In-situ Subcritical Water Extraction and Pre-characterization Platform for Martian Regolith and Ocean Worlds

F. Kehl (389R), E. Tavares Da Costa (389R), D. Wu (389R), M. F. Mora (389R), J. S. Creamer (389R), P. A. Willis (389R)  
florian.kehl@jpl.nasa.gov

## Objective

To develop an automated system to extract organic and inorganic compounds from solid samples, coupled to chemical sensors for liquid-based, compositional analysis.

## Background

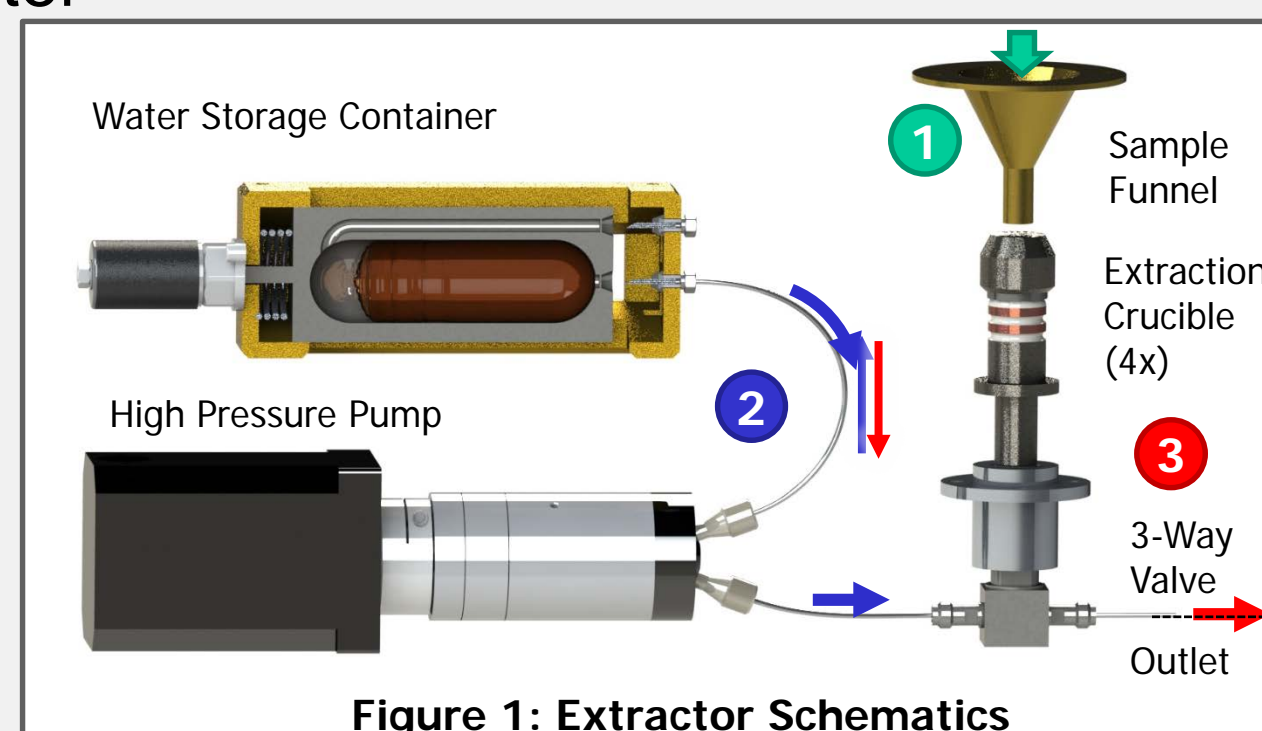
- The search for life in our Solar System is one of the highest priorities at NASA
- All life as we know it evolved in water and requires water
- Therefore, we are looking for biochemical signatures of life directly in aqueous solutions
- Inorganic compositional analysis can be used to assess the local environment's habitability
- Organic analysis of components such as amino acids is one of most powerful means for identifying potential biosignatures.

## 1st Method: Extraction

Use Subcritical Water Extraction (SCWE) to extract both polar and apolar compounds at elevated temperatures and pressure.

- Water is superheated and pressurized to keep it from boiling
- Water can greatly vary its static dielectric constant as a function of temperature and pressure
- This enables efficient extraction of a variety of organic compounds using a single, nontoxic, and easy to handle solvent: water

**HOW?** Figure 1: solids enter the extraction crucibles through the sample funnel (1). Crucible is hermetically sealed and pressurized with water by a high pressure pump (2). The cell temperature is increased to 200°C. The extraction is concluded by releasing the eluate via a 3-way valve (3).



## Results: Extraction

We developed a fully-automatic, multiplexed SCWE system, featuring

- 4 independent extraction crucibles
- Vibrating funnel for sample ingestion fed by robotic arm
- Sample carousel with magnetic encoder
- Automatic cell sealing mechanism with force sensor to ensure hermetic seal
- Integrated high-pressure fluidics, thermal control and flow-sensor
- Successfully tested and validated in the Atacama desert in Chile in 2017.

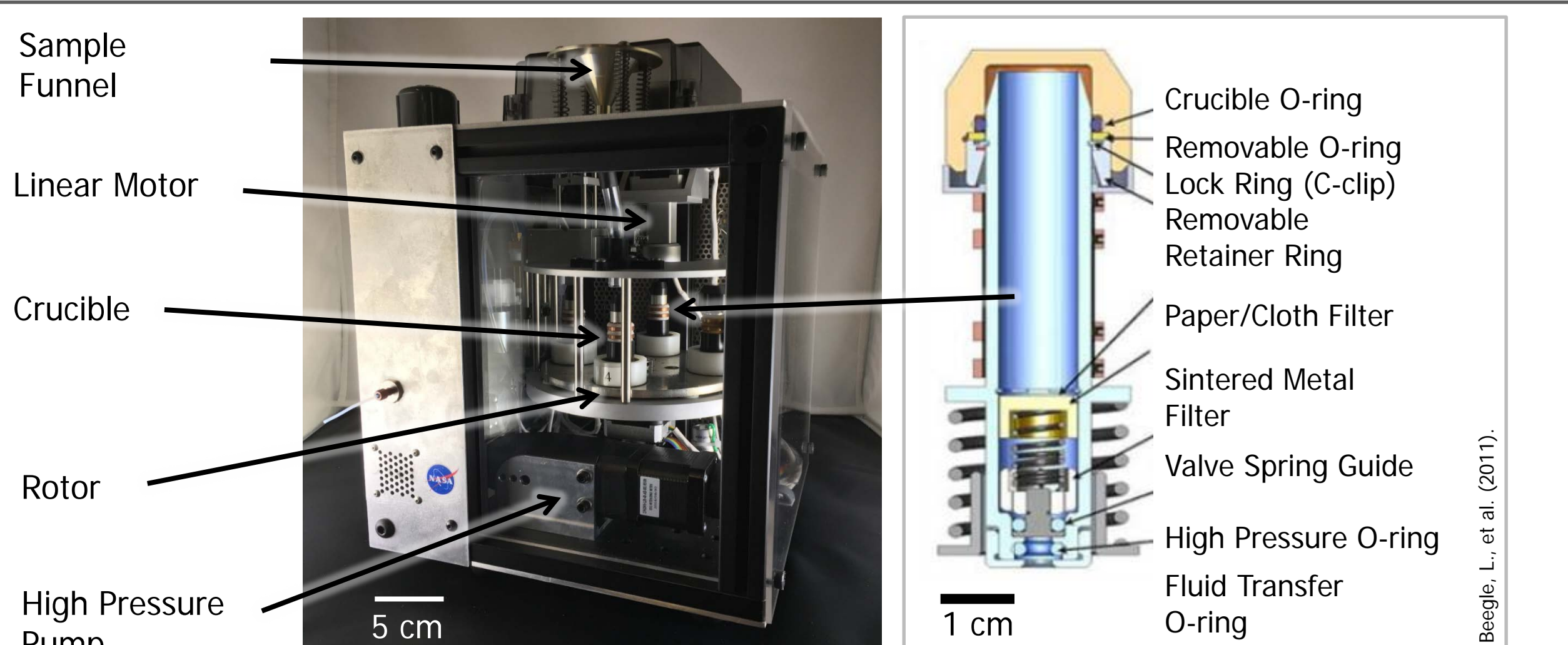


Figure 2: Automated SCWE System (top). Successful SCWE field test in Atacama desert in Chile (bottom)

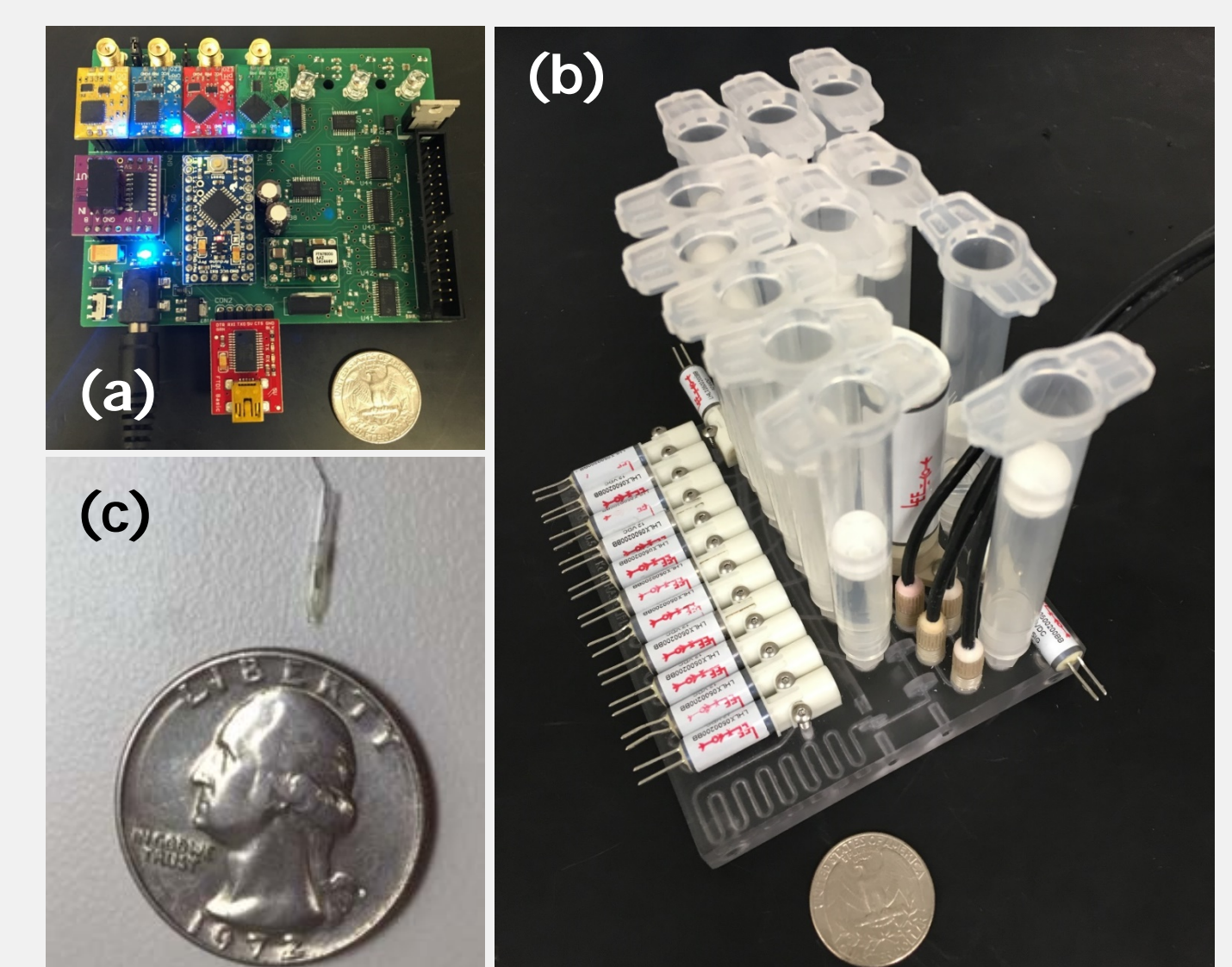
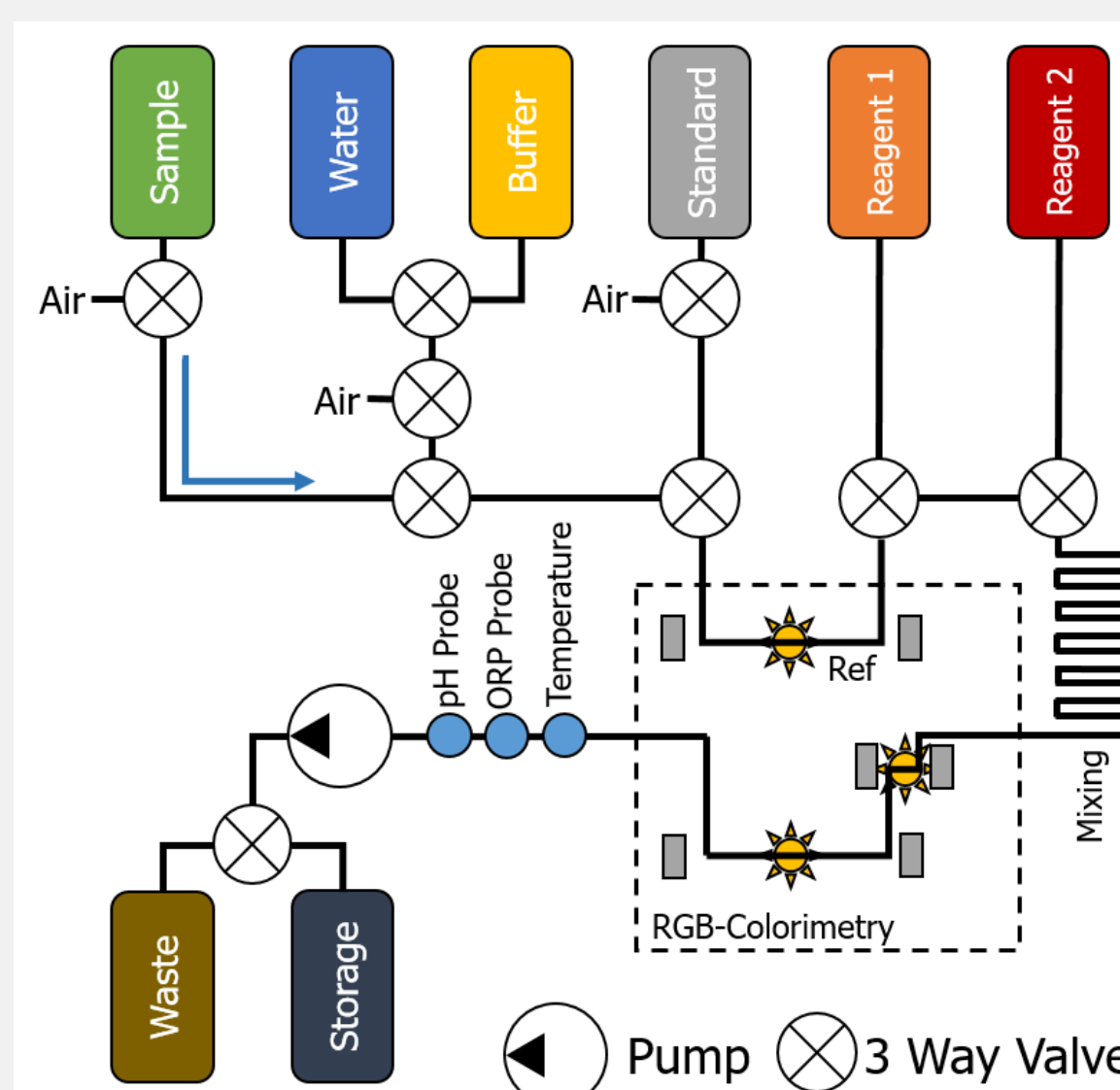
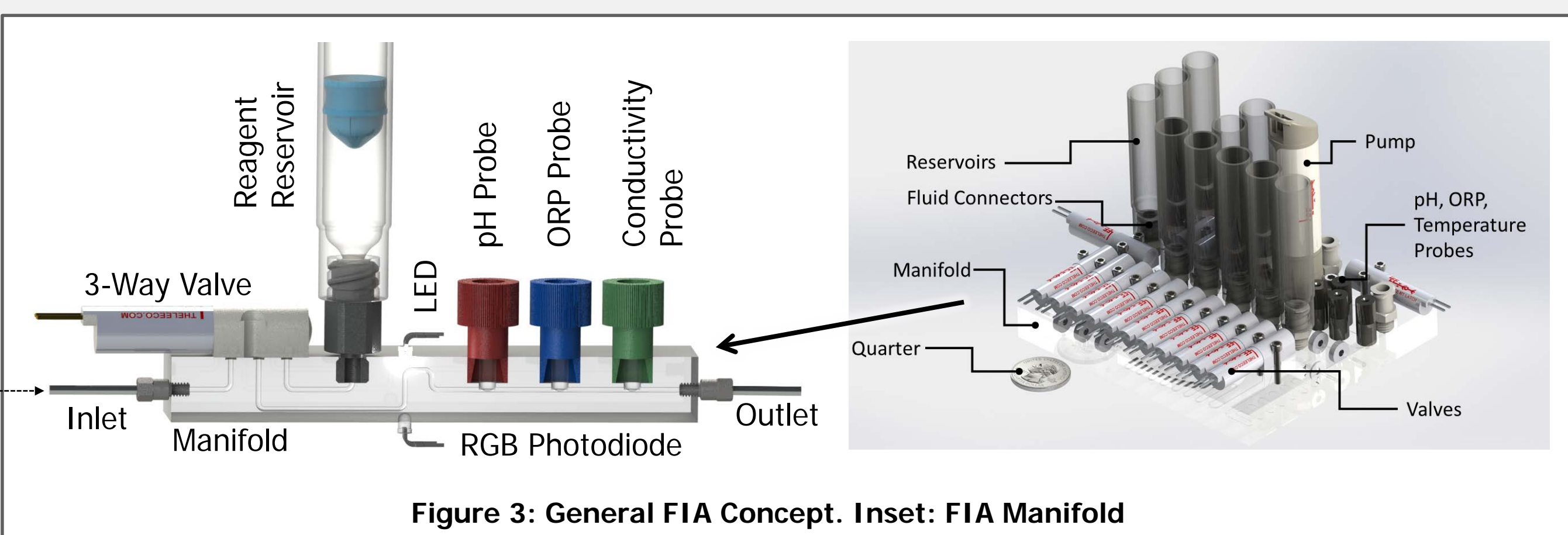
## The Challenge

Most celestial bodies in our solar system do not have readily accessible liquid water bodies to analyze. The solid samples (regolith, drill-fines or ice) have to be transferred to an aqueous phase.

## 2nd Method: Analysis

To assess the local habitability, the extract is automatically analyzed by in-line, miniaturized electrochemical and colorimetric sensors. The technique is based on a miniaturized Flow Injection Analysis ( $\mu$ FIA) system.

- Principle: injection of nL to  $\mu$ L of reagent into moving carrier stream, forming a reaction plug, which is transported towards a detector which continuously measures changes in absorbance and electrode potential
- Measures pH, redox potential and electrical conductivity of the extract
- Versatile, custom 3D printed microfluidic platform for the detection of ions such as:  $Mg^{2+}$ ,  $Ca^{2+}$ ,  $PO_4^{3-}$ ,  $ClO_4^-$ ,  $Cl^-$  and many more
- Low sample and reagent consumption
- Can be coupled to more sophisticated instruments such as capillary electrophoresis or mass spectrometers for organic analysis



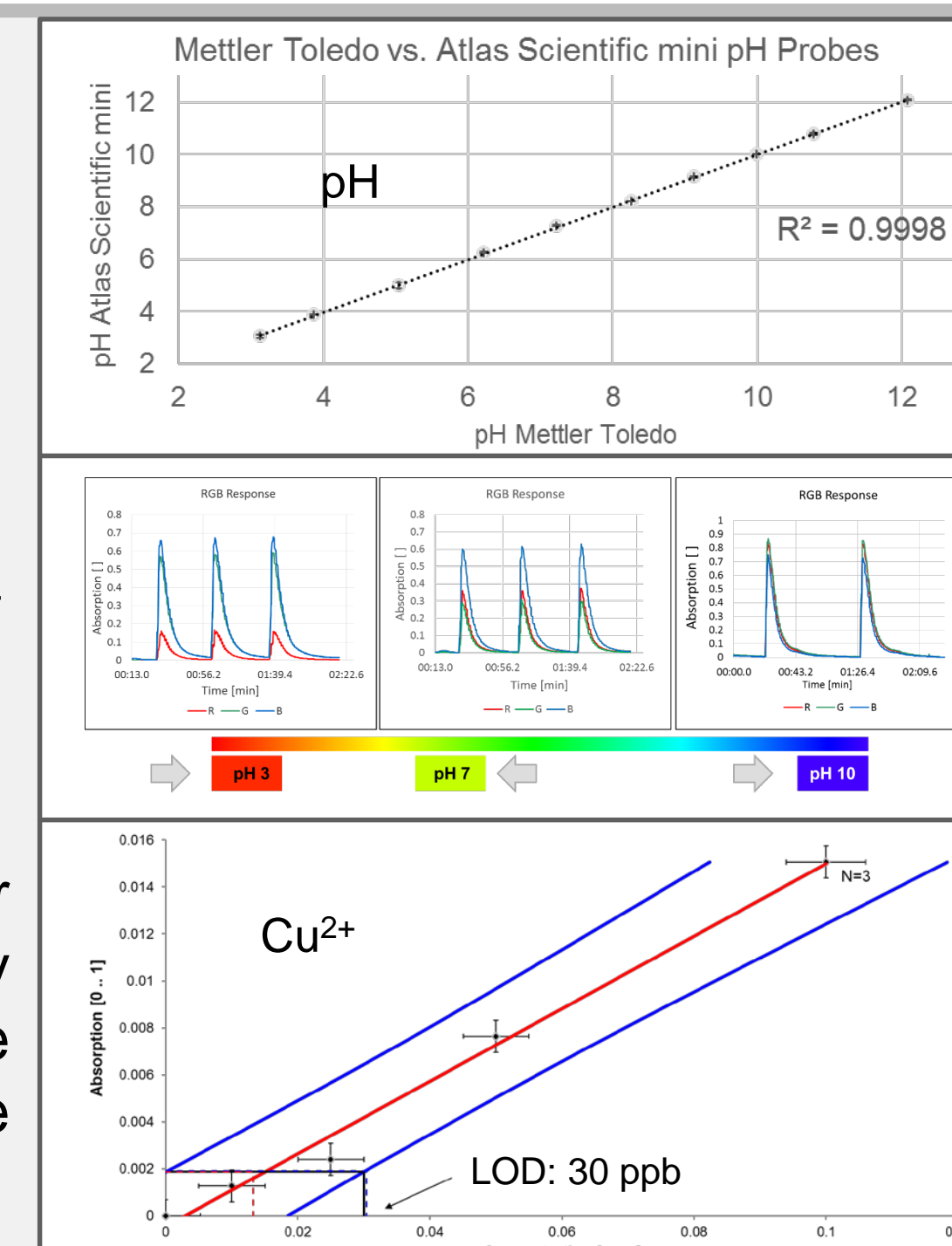
## Results: Analysis

Development of a miniaturized liquid sample characterization platform.

- Electrochemical sensing of pH, ORP, conductivity,  $Mg^{2+}$ ,  $Ca^{2+}$ ,  $ClO_4^-$ , covering concentrations ranging from 1  $\mu$ M to 100 mM
- Colorimetric measurement of pH,  $Cl^-$ ,  $Ca^{2+}$ ,  $PO_4^{3-}$  and  $Cu^{2+}$  (down to 500 nM)

## Conclusions

We developed an automated liquid sample extractor and characterization unit, which has successfully been validated in a relevant environment, the Atacama desert, thus further advancing the system's Technology Readiness Level.



## Outlook

Later in 2017, a fully-integrated version will be installed on the K-Rex Rover (NASA Ames) for autonomous in-situ measurements in the Atacama Desert (Chile) as well as the FIA portion on an underwater platform for oceanographic measurements in Alaska.



# Development of a Compact Ringdown Spectrometer

Bradley M. Gibson (389R)  
Jordana Blacksberg (389R) and Chris Webster (3200)

## Introduction

Cavity ringdown spectroscopy is more sensitive than multipass absorption spectroscopy, usually at the cost of higher complexity and lower reliability. We designed a miniaturized, simplified spectrometer that performs as well as traditional ringdown, but with fewer components and more robust alignment. We also developed a novel FPGA-based data acquisition system and a reliable fringe cancellation technique.

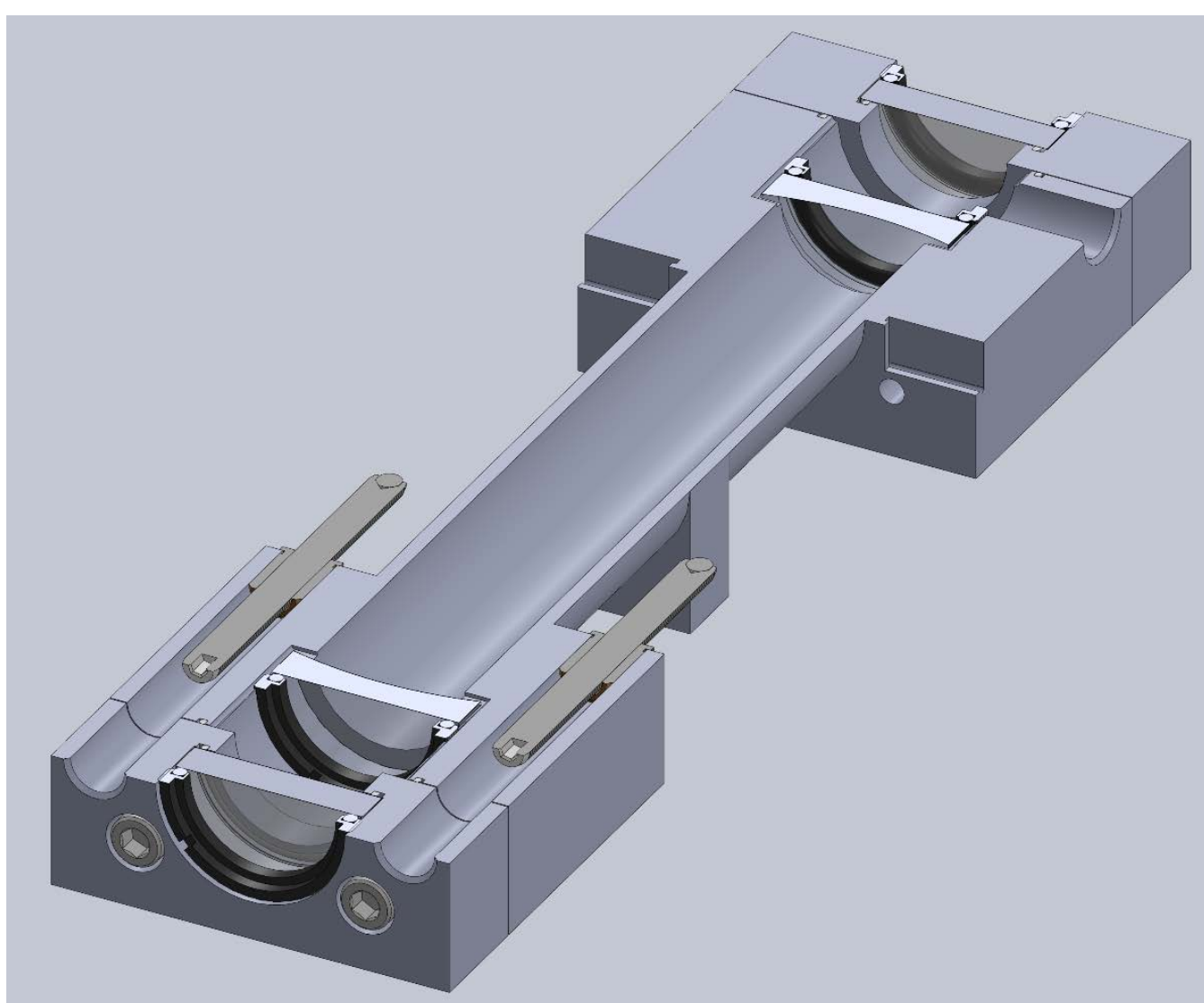
## Relevance

Increased sensitivity and small sample volume enable planetary science goals in challenging circumstances such as:

- Low abundance targets (methane on Mars)
- Difficult-to-collect samples (water plumes on Enceladus)
- Difficult-to-pump balance gases (helium on Saturn)

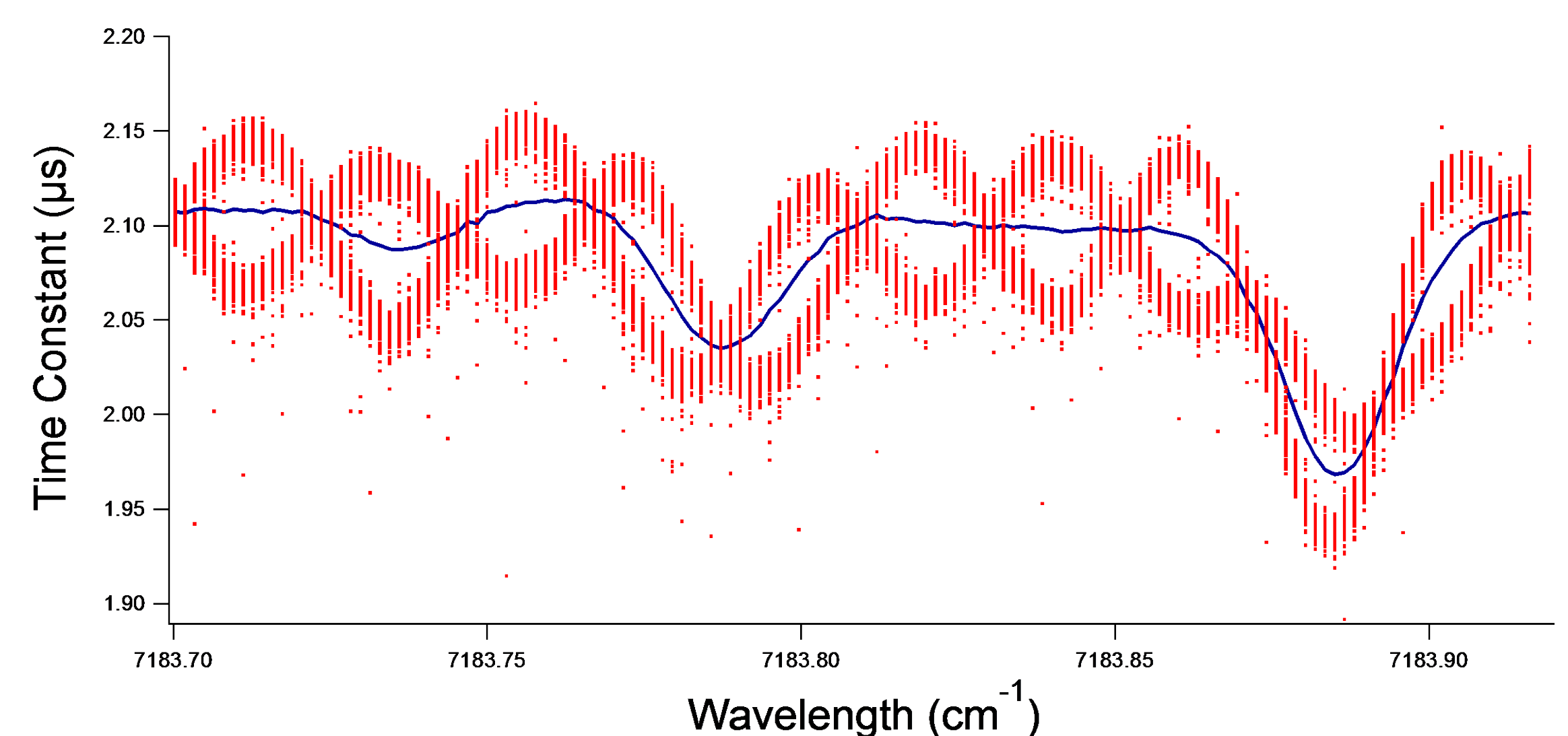
## Spectrometer Design

- Mirrors rigidly aligned by machined cell, low sensitivity to misalignment of other optics
- 12 cm mirror separation, 630 meter effective path length
- Mirrors masked to 5mm diameter to demonstrate further miniaturization potential – 2.355 cm<sup>3</sup> sample volume
- Piezo placement enables fringe cancellation technique
- Ringdown events triggered by laser switching
- All components used have equivalents available from the visible through the mid-infrared spectrum

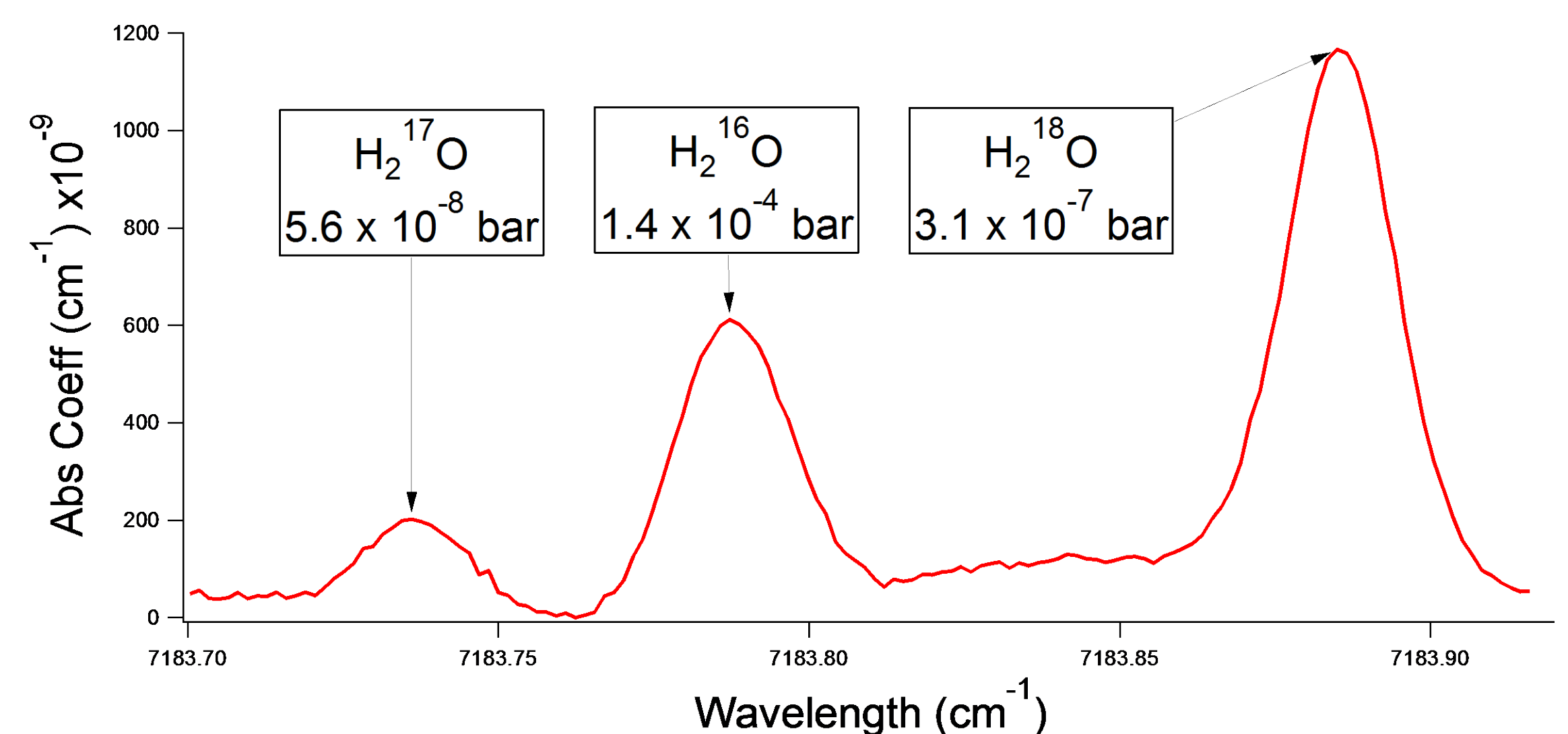


## Spectrometer Performance

- Single-point noise level:  $5 \times 10^{-9} \text{ cm}^{-1} \text{ Hz}^{-1/2}$ 
  - ~100 times better than noise level on MSL spectrometer
- Fringe cancellation technique gives noise floor of  $1 \times 10^{-8} \text{ cm}^{-1} \text{ Hz}^{-1/2}$  under real-world scanning conditions
- Validated by water vapor isotope measurements under realistic conditions at 1.39  $\mu\text{m}$



Fringe cancellation: Adjacent mode spectra (red) are acquired and processed separately, then averaged to produce a clean spectrum (blue)



Water isotope ratio demonstration: Spectrum was obtained in 170 seconds at a cell pressure of 1 mbar using humidified lab air. Partial pressures of each species were calculated assuming a cell temperature of 296 K.

## Future Goals

- Demonstrate methane measurements at 3.27  $\mu\text{m}$
- Design second-generation miniaturized cell
- Demonstrate reliability in field settings

## Conclusions

Our first generation prototype shows excellent performance, on par with typical full-sized ringdown instruments. Its design is compact enough for cubesat / UAV applications, and its increased sensitivity would enable several measurements relevant to the planetary science community.

# GRACE Accelerometer data transplant

Author: Tamara Bandikova (392A)

Christopher McCullough (392R), Gerhard L. Kruizinga (392A)

## Gravity Recovery and Climate Experiment (GRACE) – where are we now –

- 15 years of mission operation (planned mission lifetime was 5 years)
- Aging of the spacecraft → serious battery problems on GRACE-B
- Accelerometer (ACC) on GRACE-B turned off since September 2016 to reduce battery load
- ACC measurement provides information about the non-gravitational forces acting of the spacecraft (air drag, solar radiation pressure, Earth albedo)
- **ACC data are necessary for the gravity field recovery**

## Key question: can we use GRACE-A ACC data to generate the missing GRACE-B measurement?

- **Yes, because** both satellites fly in identical orbit, separated by a distance of approx. 220 km, i.e. approx. 25 s, and the change in the non-gravitational forces is assumed to be very small within these 25 s
- **Yes, but** the ACC also senses residual accelerations due to thruster firings which are unique for each spacecraft. These residual accelerations need to be modeled and removed/added from/to the GRACE-A measurement.

## The challenge: Modeling of residual linear acceleration caused by thruster firings

- There are 12 attitude control thrusters (THR) aboard, operating in pairs, controlling the angular acceleration of the spacecraft
- If the thrusters would be perfect, there will be no linear acceleration sensed by the accelerometer
- **The residual linear accelerations (“thruster spikes”) are caused by thruster imperfections such as misalignment of THR pair, force imbalance or differences in reaction time**
- The shape and amplitude of the thruster spikes are unique for each thruster pair, for each firing duration (30 ms – 1000 ms), for each x,y,z component of the ACC linear acceleration, and for each spacecraft, they also depend on other factors such as valve pressure
- **The thruster spikes are one of the most dominant high-frequency signals in the ACC measurement**
- Due to their asymmetric shape, the thruster spikes remain in the ACC data even after 35 mHz low-pass filtering

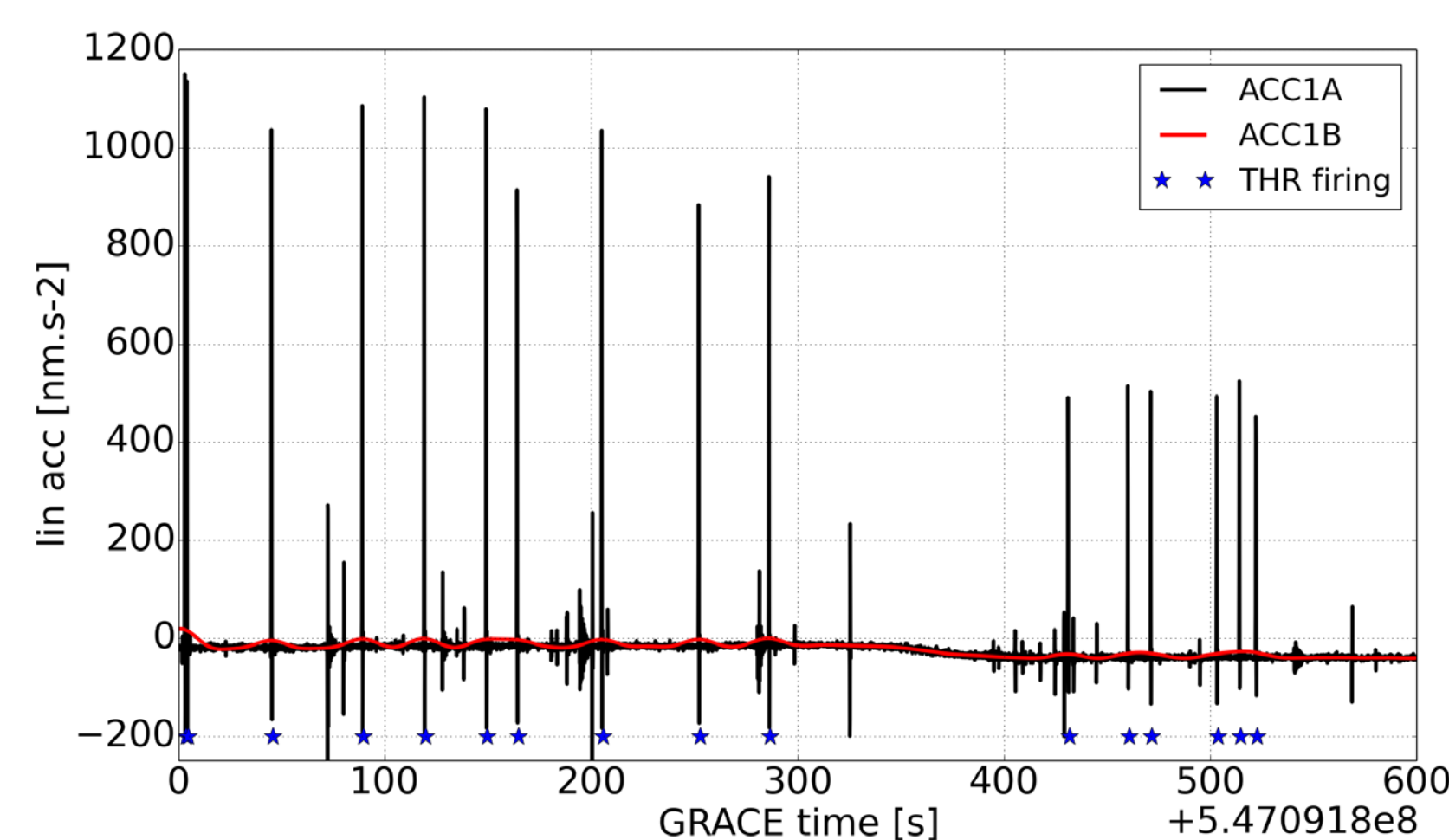


Fig. 1  
GRACE-A linear acceleration (cross-track component) - the original 10 Hz measurement (ACC1A) and the 35 mHz low-pass filtered data (ACC1B). The large high-frequency signals are the “thruster spikes” caused by the thruster firings.

## Thruster spike model

- The thruster spike model is an analytical function obtained by inverse Laplace transform of the ACC transfer function
- The thruster pulse is modeled as two pulse function (ramp shaped + squared pulse)
- The parameters to be estimated using the Least squares method are: amplitude ( $A_1, A_2$ ) and width ( $\tau_1, \tau_2$ ) of the two pulses and ACC response delay ( $t_0$ )

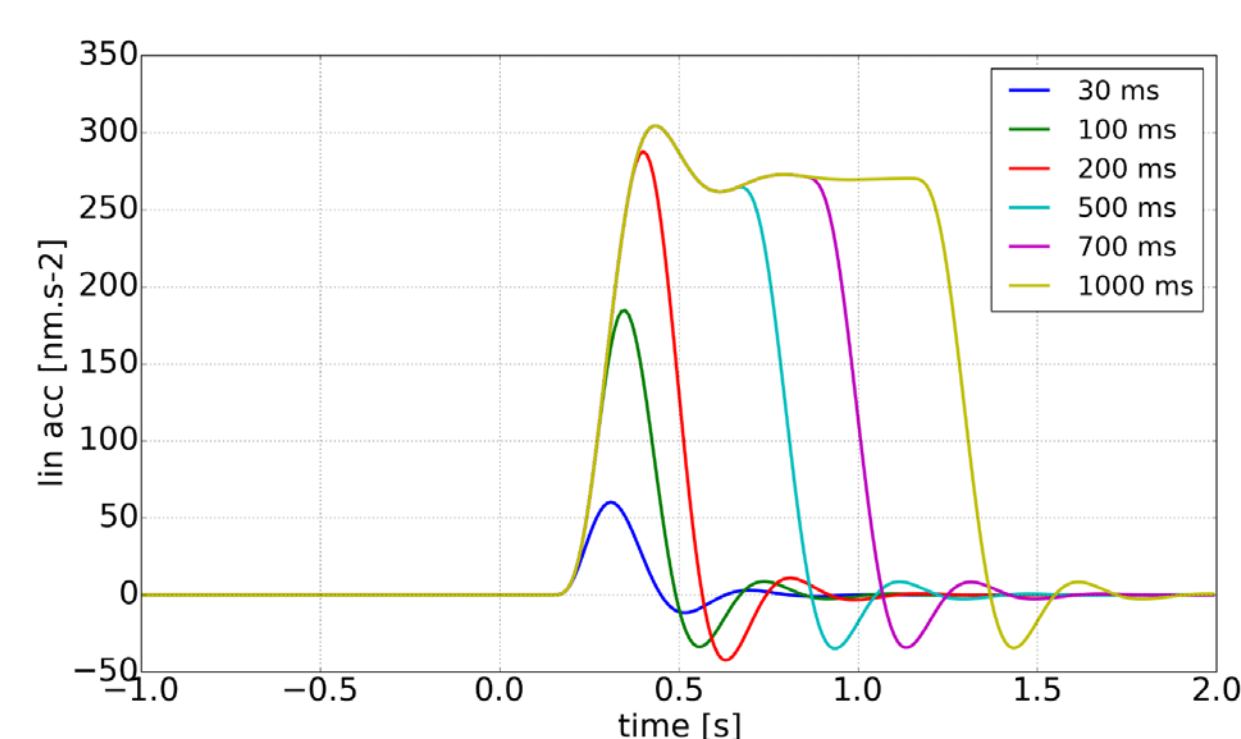


Fig. 2: Thruster spike model for different thruster duration

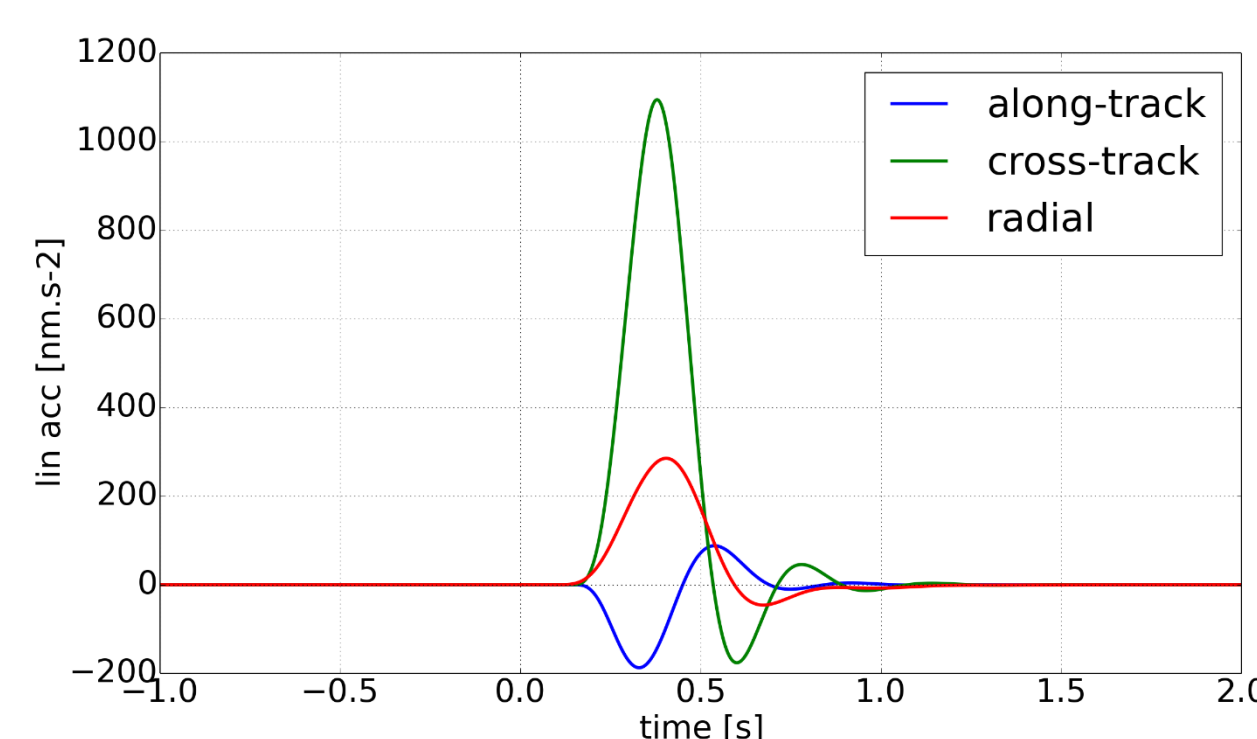
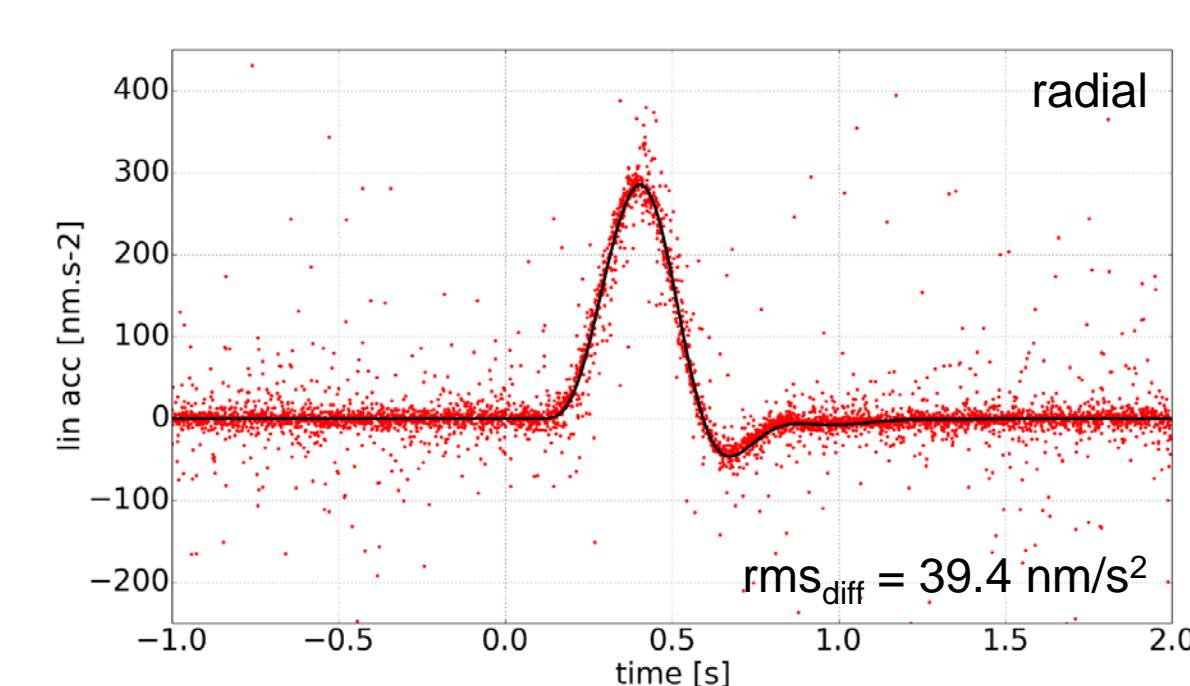
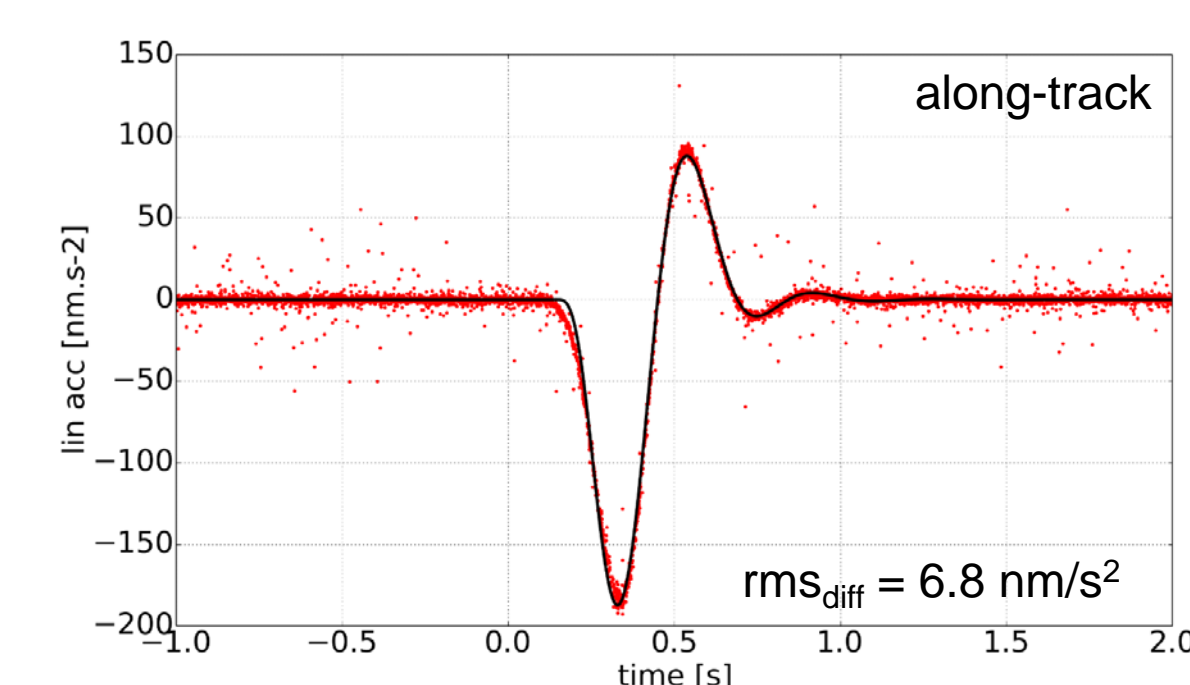
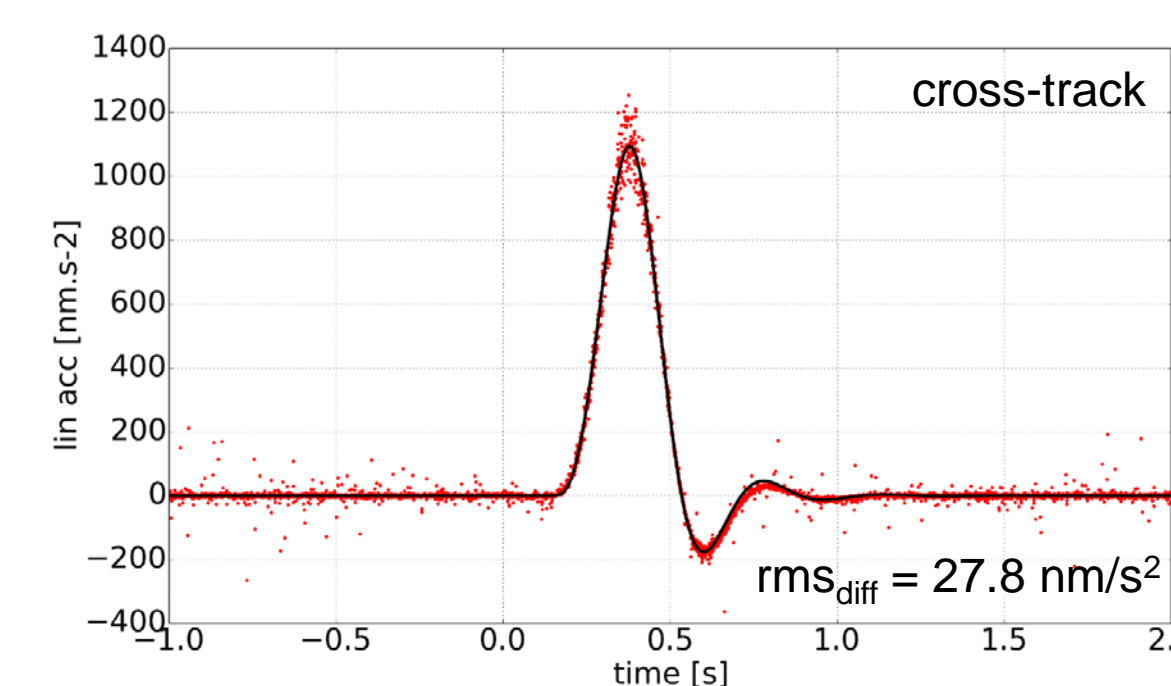


Fig. 3: Thruster spike model for (+)roll 100 ms thrust duration, all three components

Fig. 4:  
Fit of the thruster spike model to the original GRACE-A ACC1A 10 Hz data. The red dots represent approx. 170 thruster spikes caused by (+)roll 100 ms thrust on 2017-05-03.  $rms_{diff}$  gives the root mean square of the differences between the model and the ACC measurement



## ACC data transplant

G-A 10 Hz data

Remove G-A THR spike model

Attitude correction

Time correction

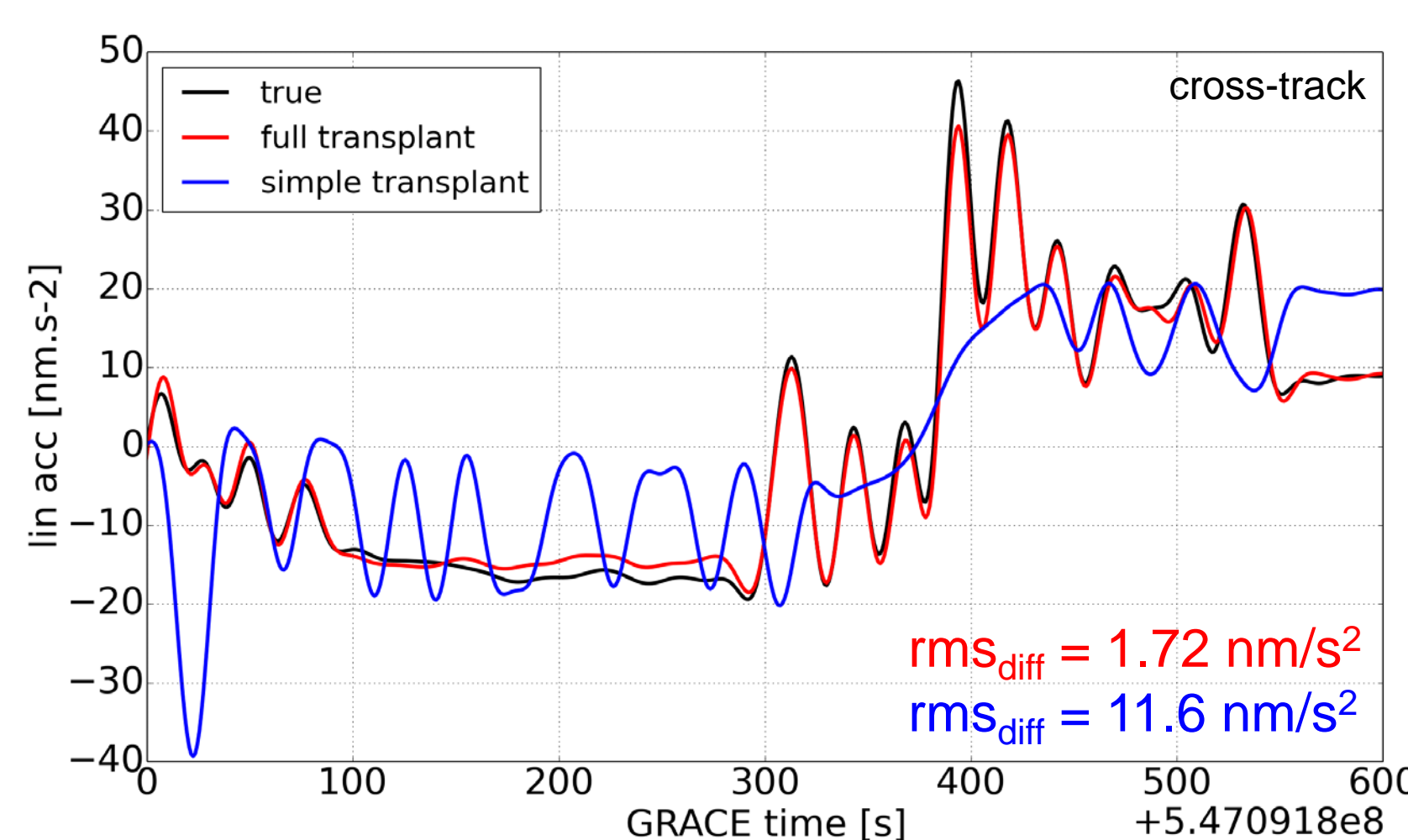
Add G-B THR spike model

35 mHz low pass filter

G-B transplanted data

- The **full ACC data transplant** requires all steps indicated in the flowchart
- As temporary solution, in the current GRACE data processing, **simple ACC data transplant** is used, i.e. without thruster spike modeling
- Validation of the ACC data transplant can be done for days when ACC data from both satellites are available
- **The fully transplanted data fits the original GRACE-B measurement very well, about a factor 7 better than the simply transplanted data**

Fig. 5: Comparison of the transplanted ACC data with the original GRACE-B data (all low-pass filtered).  $rms_{diff}$  gives the root mean square of the differences between the respective transplanted solution and the original GRACE-B data.



## Conclusions / Outlook

- ★ The missing accelerometer measurement on GRACE-B can be modeled with satisfactory accuracy by full transplant of the GRACE-A ACC data, which includes modeling of the residual linear acceleration caused by thruster firings
- ★ The full ACC data transplant is a promising solution which will allow GRACE to deliver high quality science data despite the serious problems related to satellite aging
- ★ Work in progress:  
Full data transplant to be done for September 2016 onwards followed by generating the new gravity field solutions and their analysis

# Computing Periodic Orbits and Spacecraft Orbit-Attitude Solutions

Author: Dayung Koh (392K), Rodney L. Anderson (392K)

Problem

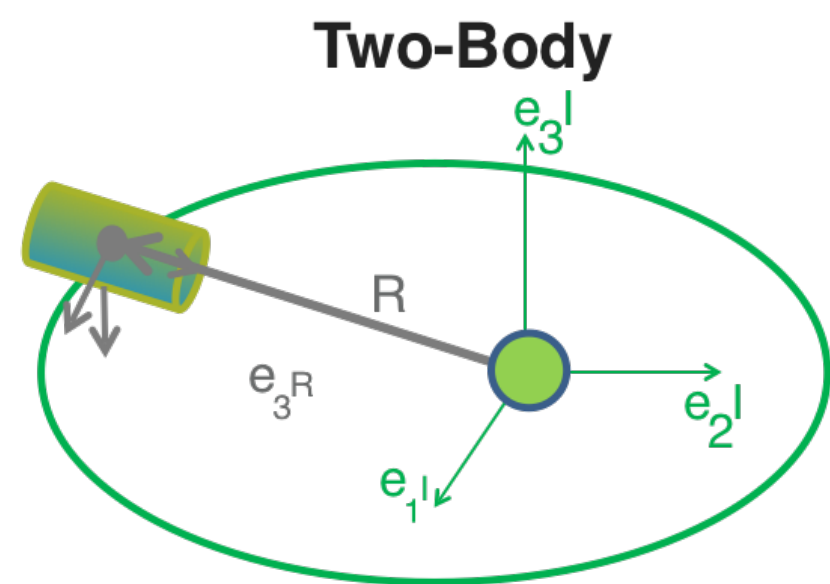
Cell Mapping Method

TRAJECTORY DESIGN

ATTITUDE CONTROL of SATELLITE

The Three-Body Problem

- + Lagrangian Points
- + Periodic Orbits
- + Low Thrust Mission Design Applications



Passive technique using Gravity gradient

Missions with no expenditure of stored energy

Natural periodic dynamics benefit Low cost mission design

Benefits

- + Generic, Systematic
- + Easy to implement for any type of nonlinear dynamics EOM
- + Generates
  - + Multiple-period periodic solutions
  - + Invariant surface
  - + Regions of attraction

Applications

- + Periodic motion analysis of Spacecraft (gravity gradient satellite/ Spinning satellite)
- + Periodic orbits in the CRTBP
- + Orbit and attitude coupled periodic motion analysis around asteroids and other bodies

Abstract

A new methodology to obtain a rapid understanding of the global dynamics for various systems is introduced. The method does not require previously known solutions as inputs, which is required for continuation approaches, and no symmetric constraints are imposed. A primary strength of cell mapping is that it is generic for various classes of problems.

Cell Mapping Method

CONTINUOUS TIME

DISCRETE TIME

$$\dot{X} = f(t, X(t), s)$$

$$z(n+1) = C(z(n))$$

$f$ : any type of nonlinear system  
 $X$ : state variable

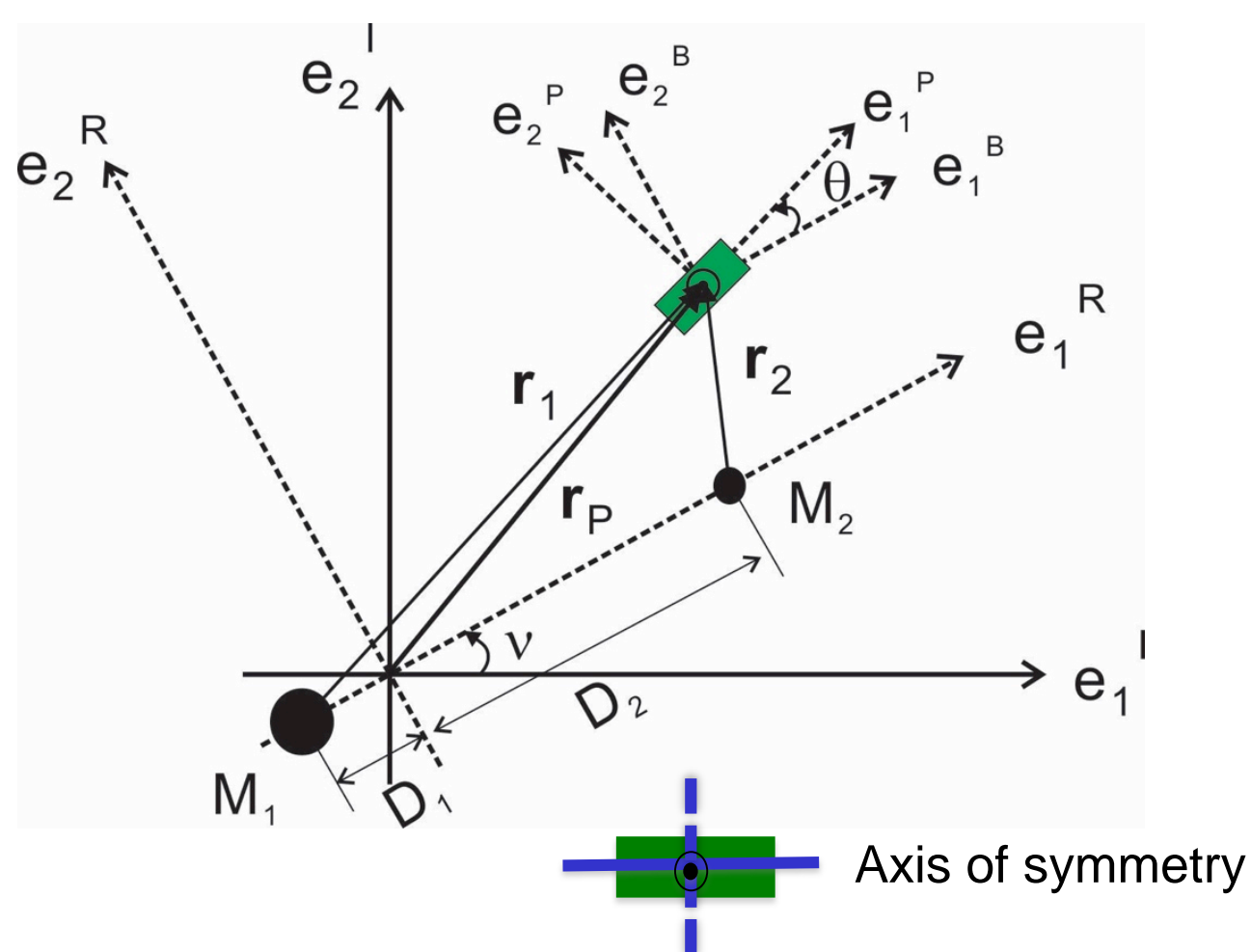
$C$ : cell mapping  
 $z$ : cell number

Motivation

There are two important components of the procedure: how to select the initial guess and how to compute periodic solutions. In many of these studies, initial conditions for the search space were determined with points emanating from the libration points or planar symmetric periodic orbits known from the previous results. Exploring undiscovered systems or the global system behavior is challenging.

Cell Mapping Method Example

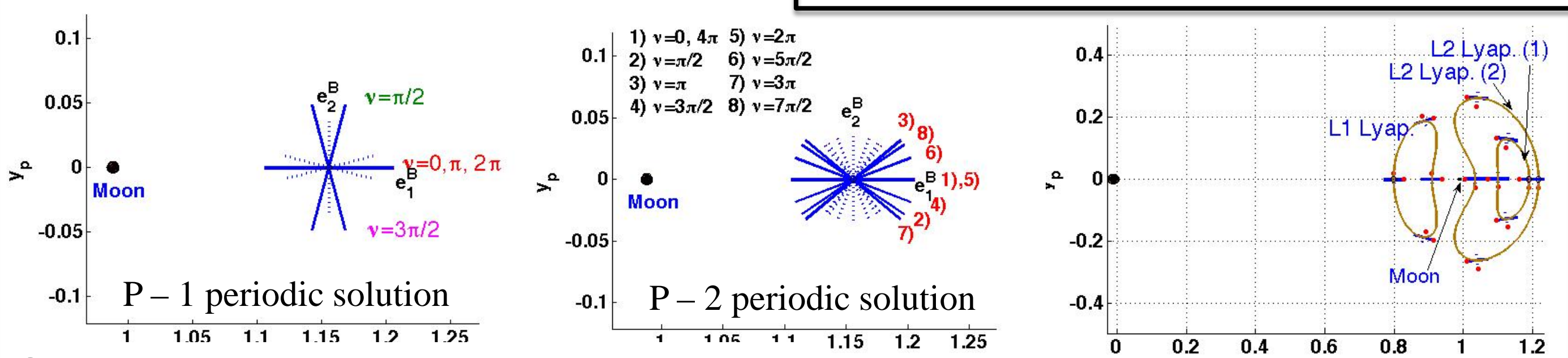
Orbit + Attitude Problem in the Three body problem



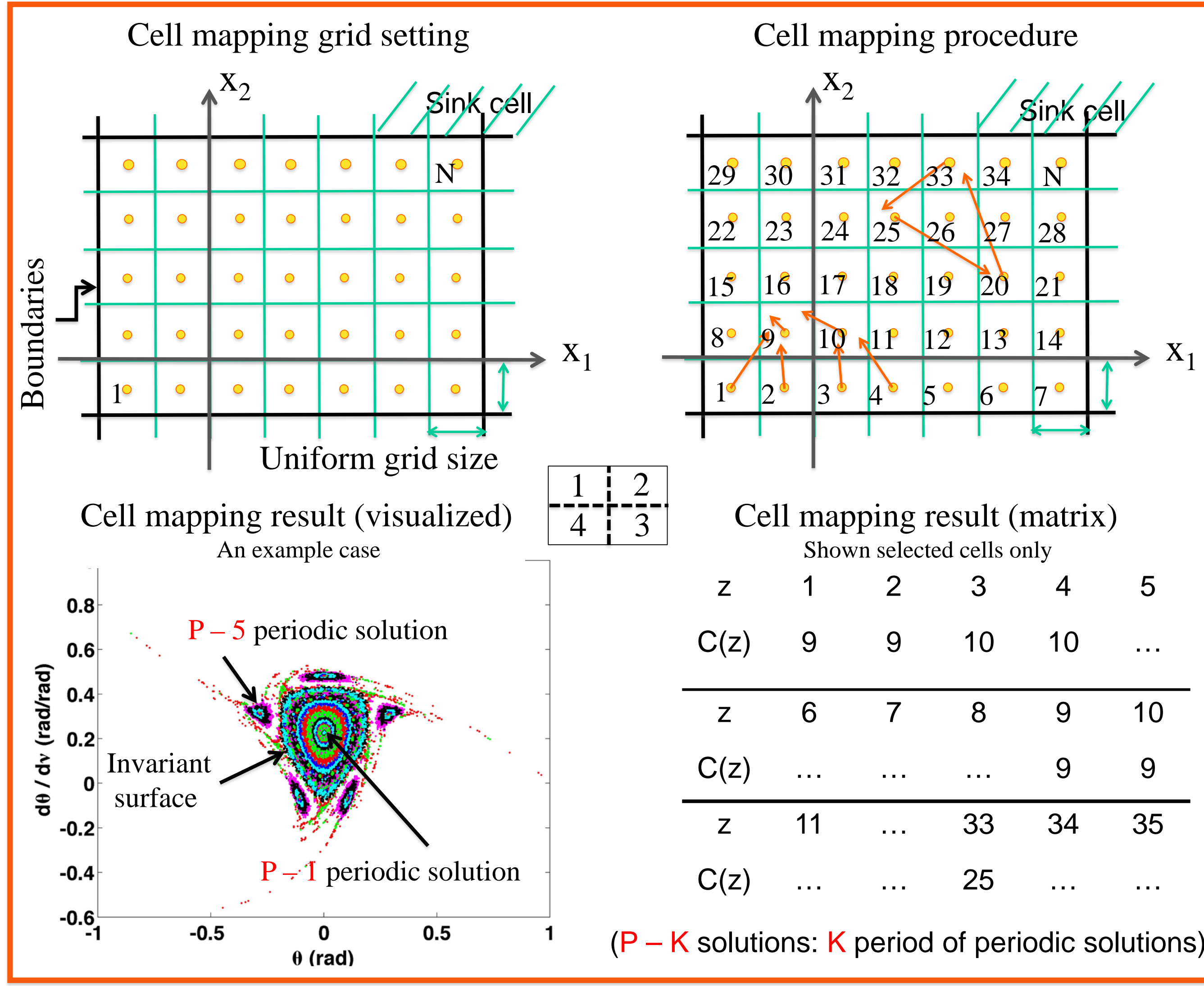
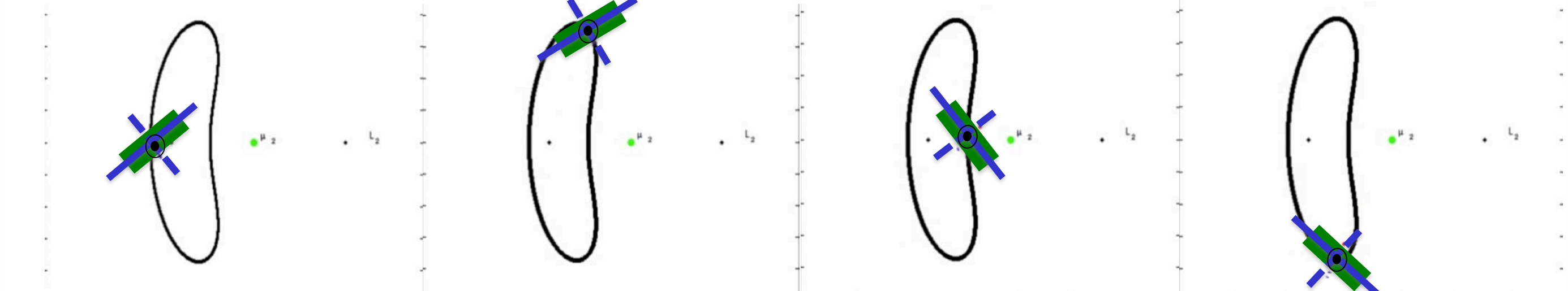
Results

- + Invariant surfaces shrink /w eccentricity
- + P - 1 solution amplitude grows /w eccentricity
- + P - 1 solution bifurcates as Spacecraft width and height ratio changes at E - M, L<sub>2</sub>
- + Multiple periodic solutions are found, and they might be useful for low cost station keeping

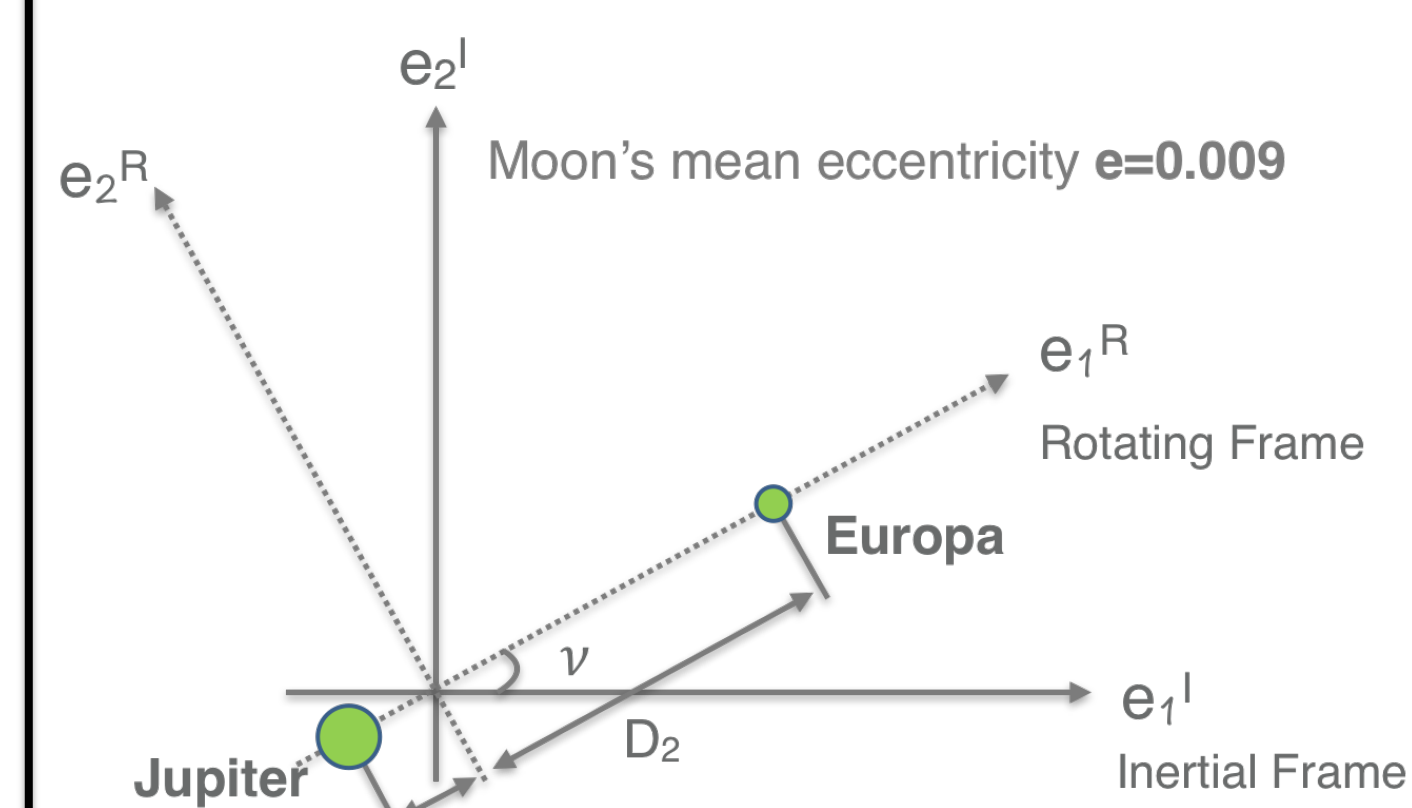
Spacecraft Motion at Lagrangian point



Spacecraft Motion on a Lyapunov orbit



Landing / Relay orbit survey for a potential Europa lander



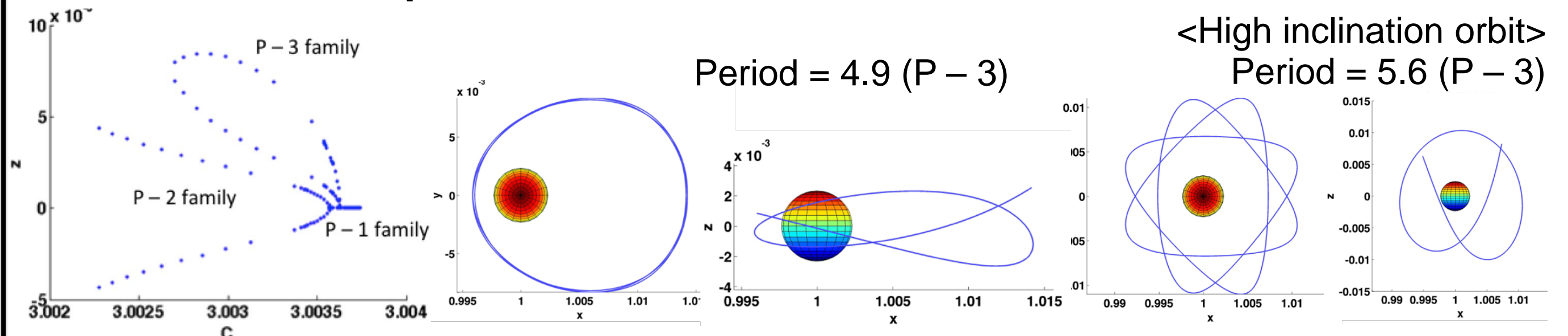
Results

- + A catalog with large range of Jacobi constant and periods of periodic orbit families is built
- + found highly inclined, asymmetric 3D orbits
- + claimed newly found orbit solutions
- + studied bifurcation orbits to find global characteristics of the system

Orbit Example

Period = 8.82  
Jacobi const = 3.00251

Bifurcation Example



# Avoiding Armageddon: Long Term Asteroid Orbit Deflection Optimization

Author: Siegfried Eggl (392-R)

Steven R. Chesley, Davide Farnocchia, Paul Chodas (392-R)

## 1. Abstract

Today, the majority of asteroids that could cause global disasters if striking the Earth are tracked on a regular basis [1-3]. In contrast, the whereabouts of the vast majority of 100 m sized near-Earth objects (NEOs) remain largely unknown [4]. Should an asteroid be discovered and predicted to impact our planet near a population center, humankind now has the option of sending a space-mission to deflect the potentially hazardous object's orbit. A kinetic impactor (KI) spacecraft, for instance, could transfer momentum to the asteroid through a high velocity collision, thus avoiding a future impact on our planet. Differences in asteroid shape and composition, however, cause the magnitude and direction of the delivered momentum to be to some degree uncertain [5-7]. Without accurate information on where an asteroid is 'parked' after a deflection attempt, the same object may become a concern for planetary safety at a later date. In the worst case, the target asteroid enters a so-called 'gravitational keyhole', retaining a high probability to collide with our planet. In order to avoid such scenarios, we demonstrate how to best target an asteroid during a kinetic deflection maneuver so as to minimize the chances of an Earth impact in the foreseeable future.

## 2. Momentum Enhancement

The change in an asteroid's heliocentric velocity vector ( $\Delta\vec{v}$ ) caused by a kinetic impact can be described through a linear momentum transfer equation [8]

$$\Delta\vec{v} \approx \frac{m}{M} [\vec{v}_\infty + \vec{\beta}], \quad \vec{\beta} = (\beta - 1) (\vec{n} \cdot \vec{v}_\infty) \vec{n}, \quad (1)$$

where  $M$  is the asteroid's mass,  $\vec{n}$  the surface normal vector at the location of impact and  $m$  and  $\vec{v}_\infty$  the impactor spacecraft's mass and relative velocity, respectively. Ejecta from the impact crater cause an

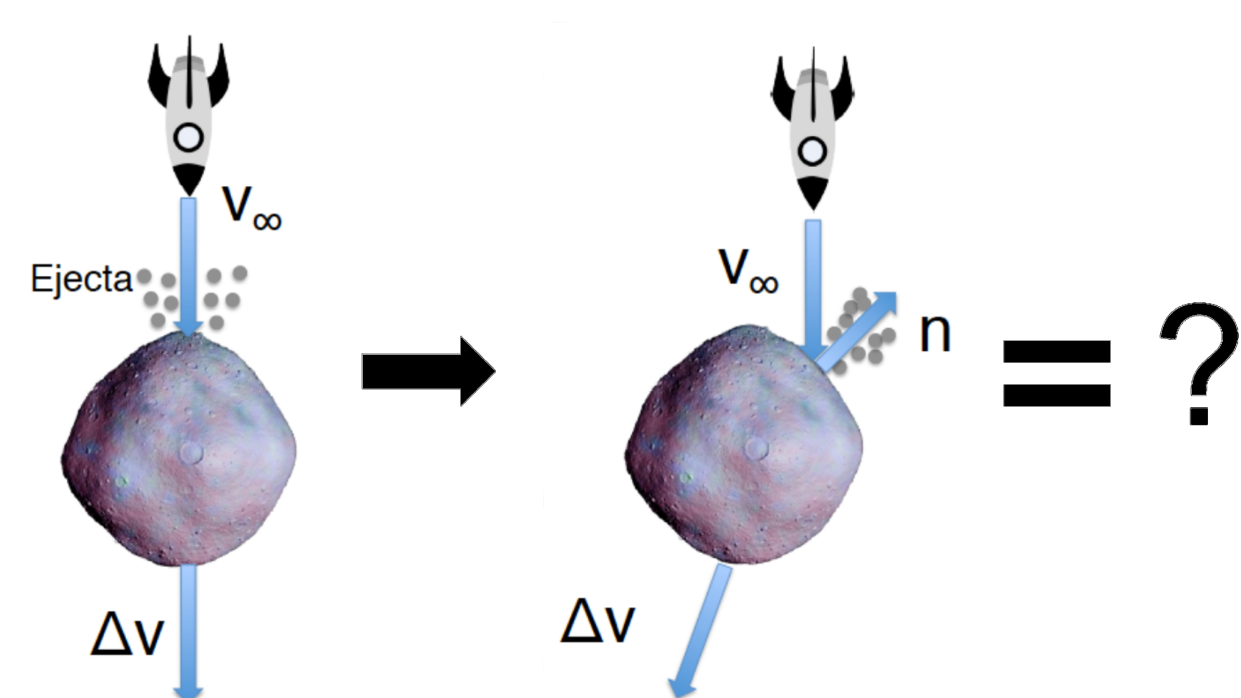


Figure 1: KI based asteroid deflection.

additional momentum enhancement ( $\vec{\beta}$ ) influencing the direction of  $\Delta\vec{v}$ . Laboratory experiments and modeling efforts have seen some success in estimating the range of possible  $\beta$  values [6-7]. However, uncertainties in the direction and magnitude of the net ejecta momentum vector remain uncomfortably large [7-9], in particular due to a dependency on a target's shape, see Figure 1. Accounting for those factors, where should a potentially hazardous object best be targeted and what consequences for future encounters with the Earth can be expected?

## 4. Shape Dependency and Asteroid Targeting Maps

How much a KI alters an asteroid's position on a future b-plane ( $\Delta\zeta$ ) depends on the shape of the asteroid. This is due to  $\vec{\beta} = \vec{\beta}(\vec{n})$  in eq. (1). While the response in  $\Delta\zeta$  is qualitatively similar between an idealized, spherical model and the actual shape of Benu, quantitative differences emerge when several  $\beta$  values are considered and impact probabilities estimated.

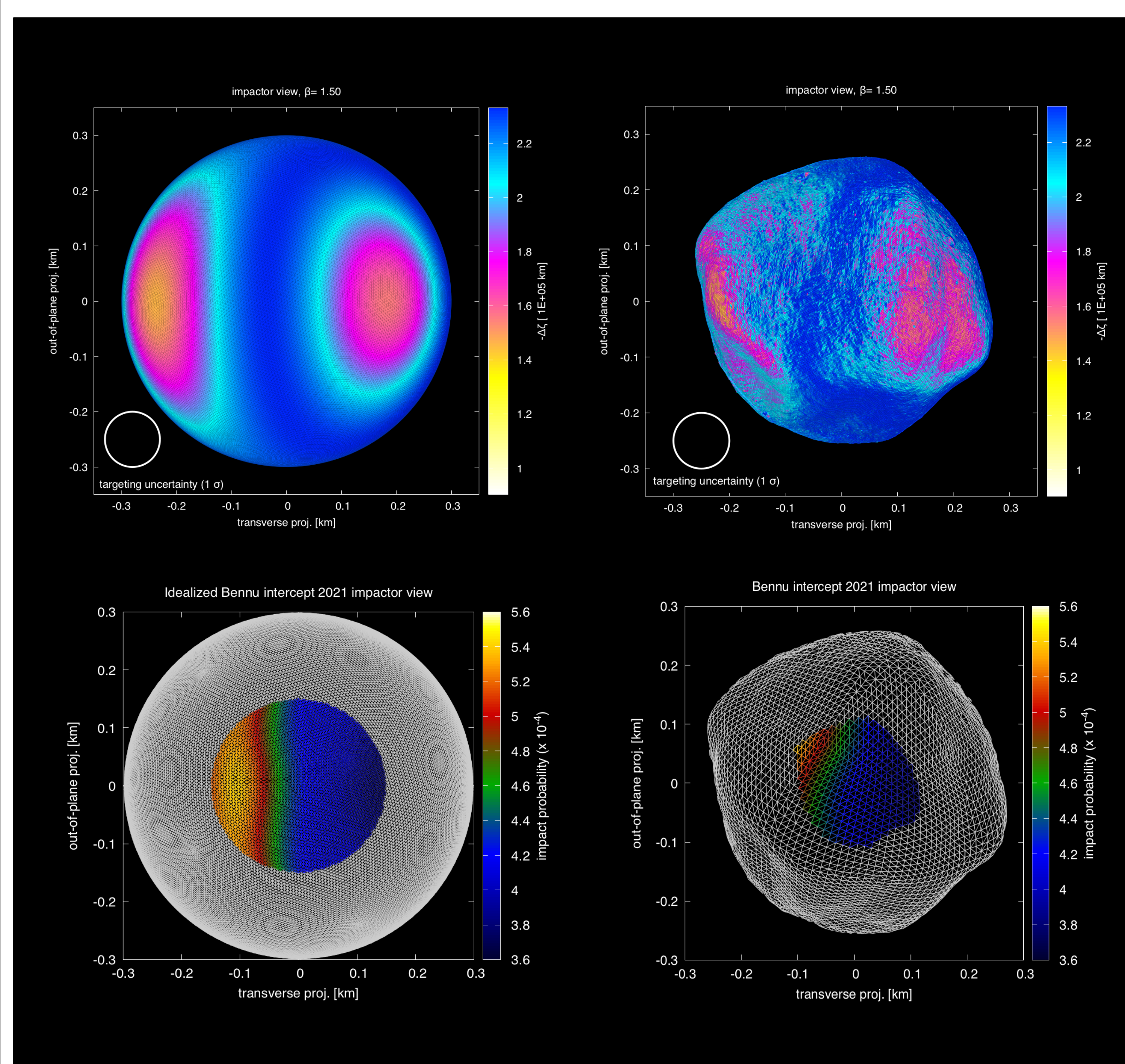
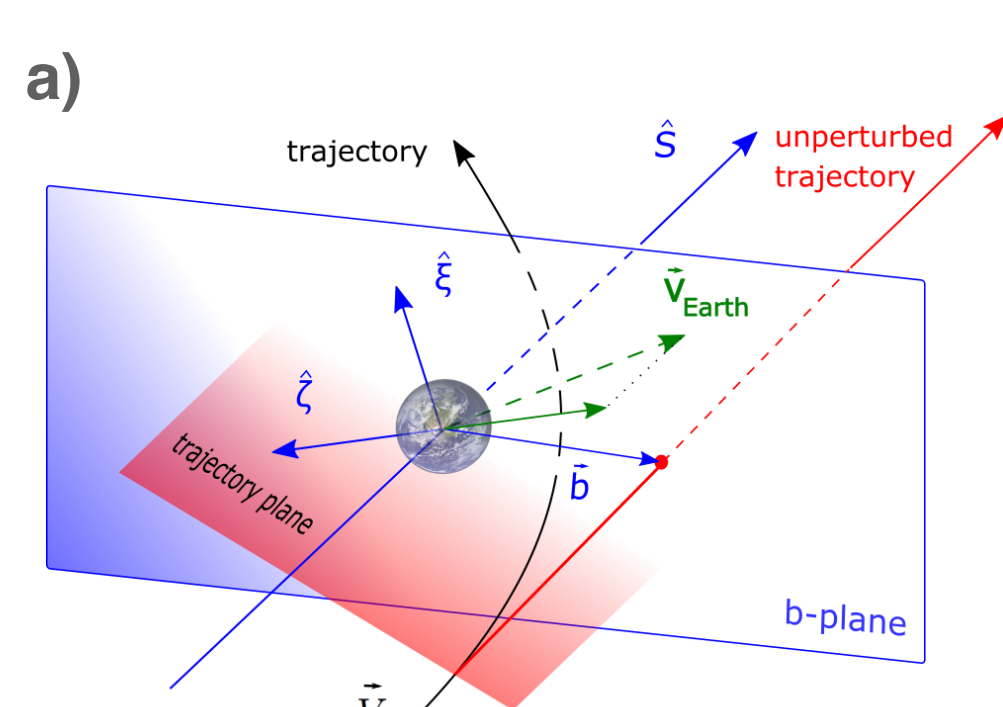


Figure 3: The b-plane displacement (top) and impact probability (bottom) for a simplified (left) and realistic shape (right) of the near-Earth asteroid (101955) Benu are shown from an impactor spacecraft's perspective.

In order to determine the target location that would yield the lowest impact risk after the deflection attempt on the asteroid we performed Monte-Carlo simulations assuming a uniform distribution of  $\beta$  between 1 and 3, as well as a 3- $\sigma$  targeting uncertainty of 150 m with a Gaussian envelope. Only the center region of the asteroid was targeted so as to avoid a miss. Naturally, the orientation of the object at the time of impact needs to be considered for the realistic shape model. Results are shown above. Targeting uncertainties and the shape of the asteroid influence the optimum impact location. Aiming for the largest shift ( $\Delta\zeta$ ) in the 2135 b-plane would not necessarily be the best choice in terms of lowering the post deflection impact probability. Instead, a region 100 m to the right of the center of the projected shape would be a good point to target.



## 3. Keyhole Maps

During close encounters with our planet, an asteroid's orbit uncertainty can be mapped onto the 2-body scattering plane (b-plane) [10], see Figure 2 a). The resulting probability density is shown for (101955) Benu the target asteroid of NASA's OSIRIS-REx mission (OREx) [11] in Figure 2 b). During a close approach with the Earth, an asteroid's orbit is changing. Some of those changes would cause the asteroid to return and impact the Earth at a later date. Initial conditions leading to future impacts correspond to certain locations on the b-plane, so-called 'keyholes'. Keyholes in the 2135 b-plane are represented by the vertical bars in Figure 2 b). It is possible that Benu could enter one of several keyholes during its close encounter with the Earth in the year 2135 leading to collisions with the Earth five to six decades later. Depending on the findings of OREx, Benu may have to be deflected.

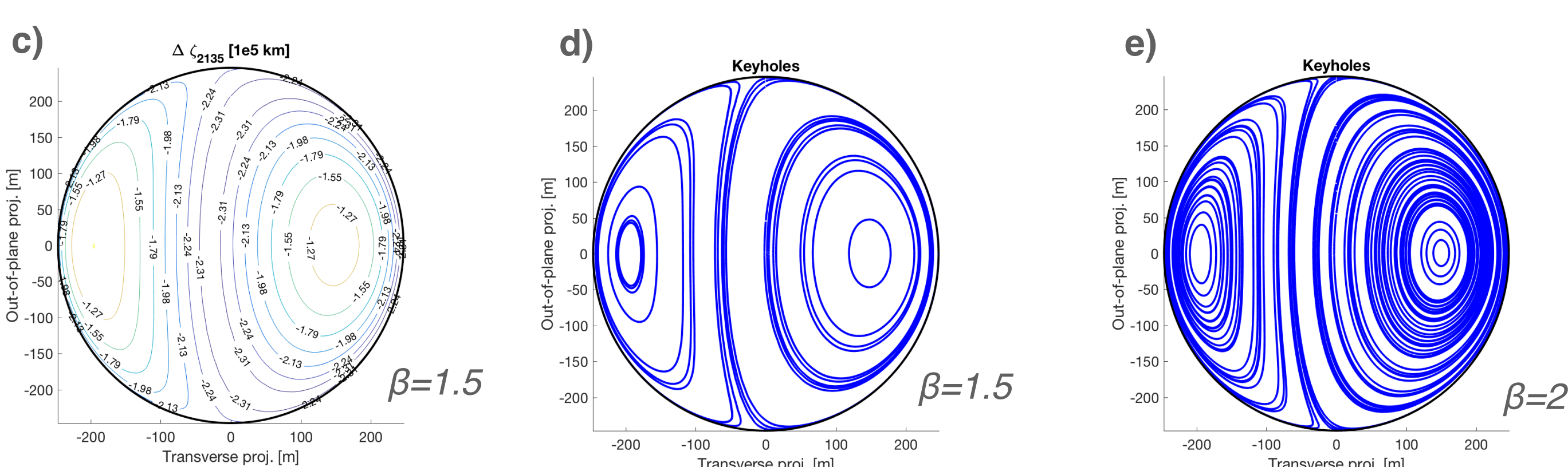
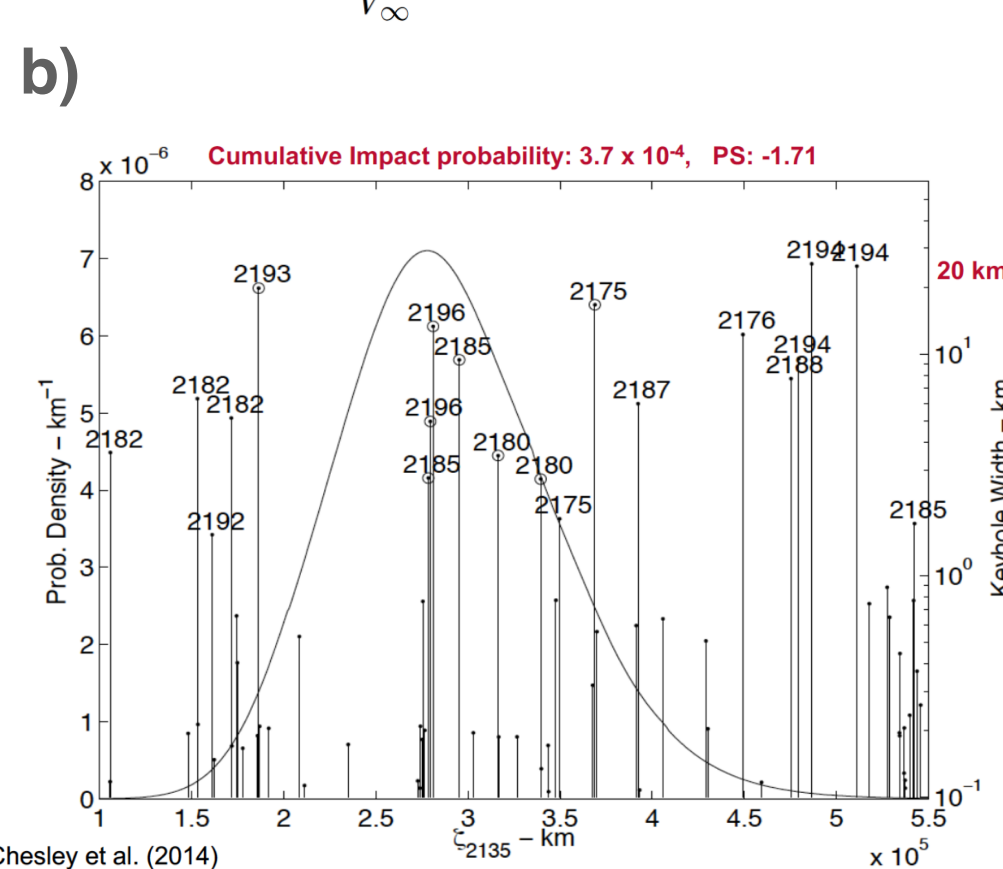


Figure 2: b-plane and keyholes for the year 2135 mapped on (101955) Benu's surface.

Given the extended presence of OREx at Benu, a kinetic impact orbit deflection experiment was considered. Arriving at the asteroid in 2021 with a relative speed of 14.9 km/s the impactor would change the heliocentric velocity of Benu by up to 0.2 mm/s. This would suffice to significantly alter Benu's position in the 2135 b-plane ( $\Delta\zeta$ ), see Figure 2 c). Depending on where the asteroid would be hit and on the amount and direction of the resulting ejecta, Benu could be pushed into a 'secondary gravitational keyhole', however, leading to a potential future impact. Mapped onto the surface of the asteroid the keyholes for Benu are shown in Figure 2 d) and e). Where to best aim in order to avoid a future collision with the Earth depends not only on the location on the asteroid but also on the ejecta momentum ( $\vec{\beta}$ ).

## References

- [1] Milani, A., et al. *Icarus* 173.2 (2005): 362-384.
- [2] Chamberlin, A. B., et al. (2001): *Bulletin of the American Astron. Soc.* Vol. 33.
- [3] Chodas, P. (2015): In *AAS/DPS Meeting Abstracts* (Vol. 47).
- [4] Harris, A.W., & D'Abramo, G. *Icarus* 257 (2015): 302-312.
- [5] Flynn, G. J., et al. *Planetary and Space Science* 107 (2015): 64-76.
- [6] Jutzi, M. & Michel, P. *Icarus* 229 (2014): 247-253.
- [7] Holsapple, K. A. & Housen, K. R. *Icarus* 221 (2012): 2, 875-887.
- [8] Scheeres D. J. et al. (2015), *Aerospace Conference* (2015): IEEE, 1-7.
- [9] Eggl, S. et al. *Advances in Space Research* 56 (2015): 528-548.
- [10] Valsecchi, G. B., et al. *Astronomy & Astrophysics* 408.3 (2003): 1179-1196.
- [11] Chesley, S. R., et al. *Icarus* 235 (2014): 5-22.

## Acknowledgements

This research has received funding from the Jet Propulsion Laboratory through the California Institute of Technology postdoctoral fellowship program, under a contract with the National Aeronautics and Space Administration.

# TOWARDS SMART SCREENING OF NAND FLASH MEMORY FOR SPACE APPLICATIONS

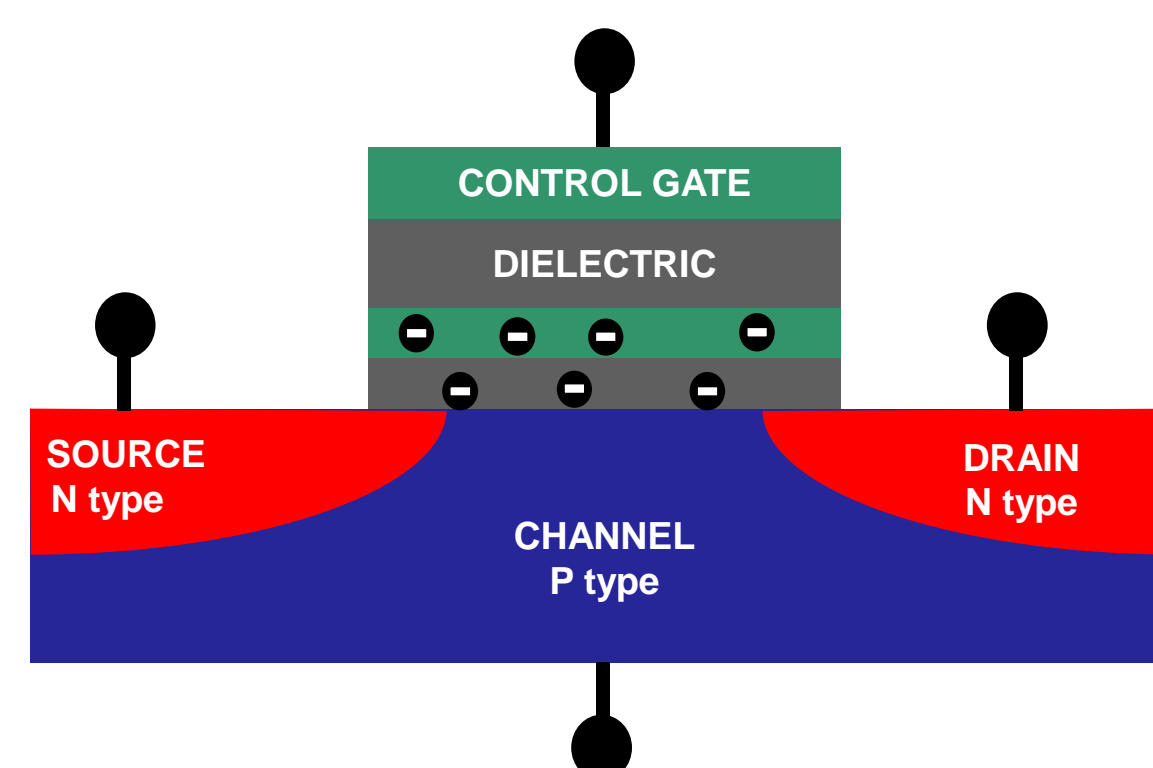
Avyaya Jayanthi Narasimham (5141), Randall Swimm (5141), Dariush Divsalar (332B), & Jean Yang-Scharlotta (5141)

**Goal: A technique, which is applicable at part level while providing insights into bit level failure.**

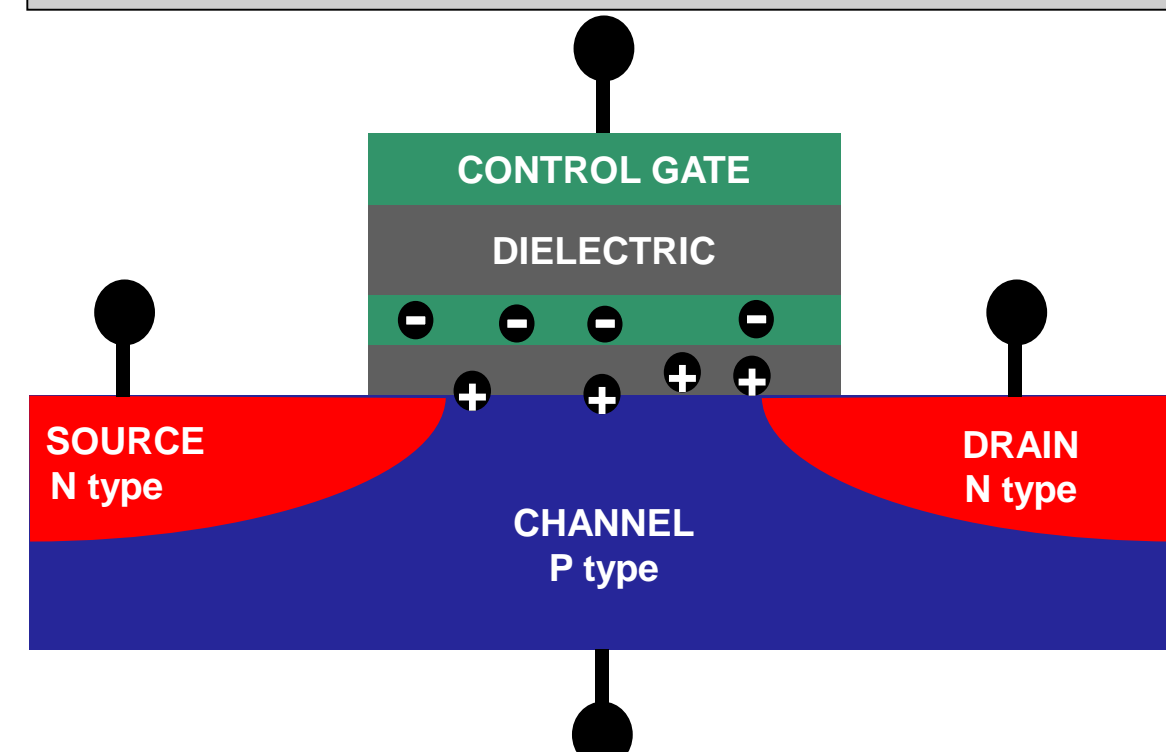
The current screening approach is limited by the large set of variables due to radiation exposure, program-erase cycles and extreme temperature exposure and their mutual interactions. Also, upcoming Europa mission requires electronics to perform under high radiation, extreme temperatures and longer mission duration, thus, it is necessary to create an efficient approach. We propose an innovative technique to map the weak bits which fail much earlier than the large population eventually leading to the part-failure.

Now, at the start of icy world missions such as the Europa program with its highly demanding radiation, temperature and mission length requirements, need for deeper understanding is more urgent than ever. Our innovative technique will ultimately increase the screening certainty and can lead to better NAND-based data storage for improved instruments and spacecraft, and greater science delivery. Thus, providing greater mission assurance and safety for appropriate JPL missions.

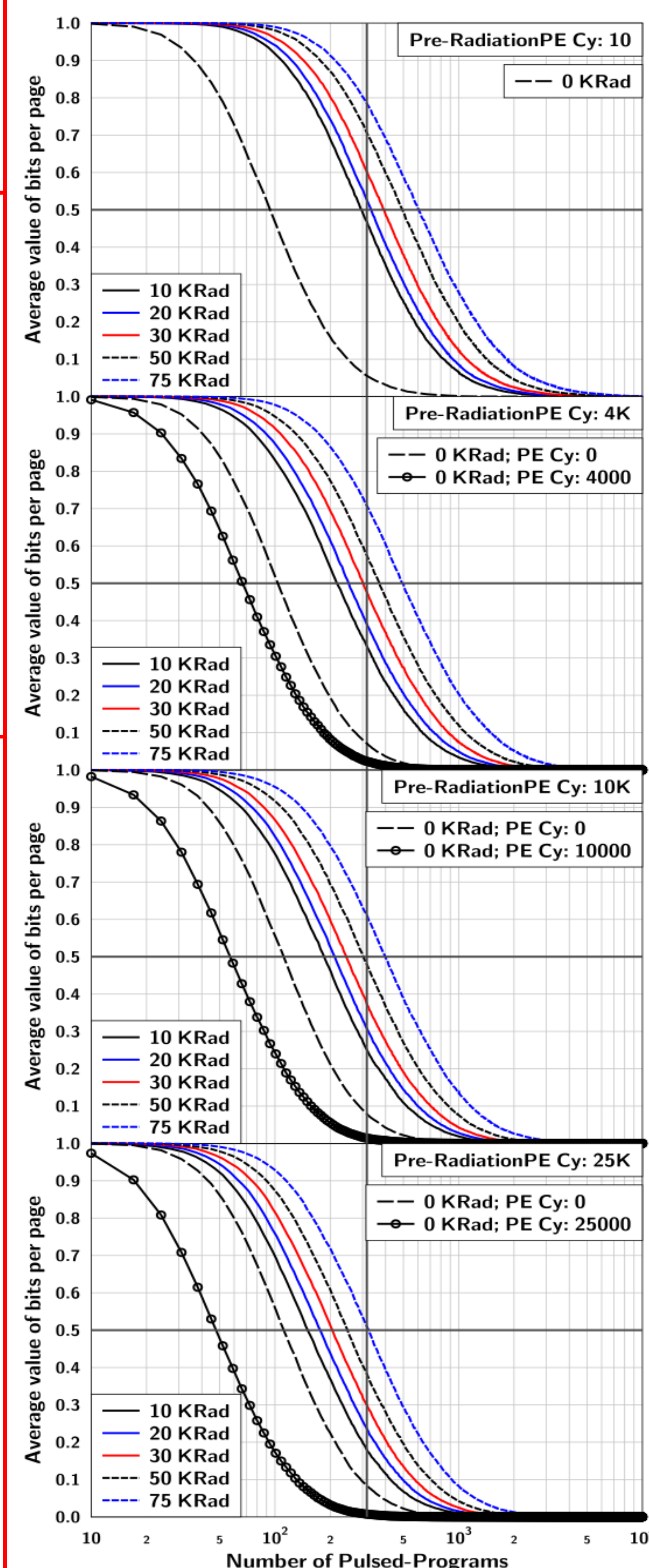
Programs-Erase stress traps electrons creating negatively charge traps



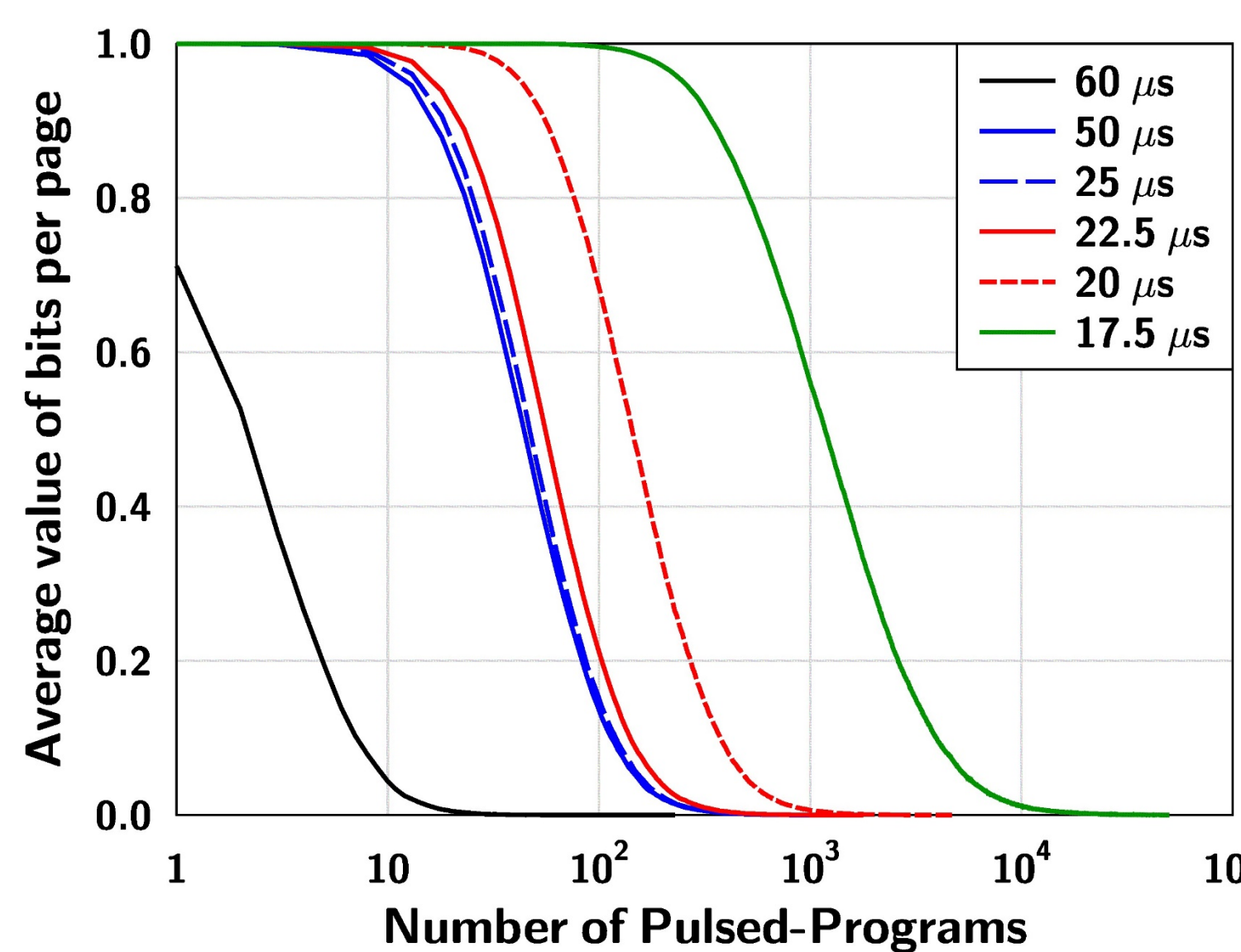
Incoming radiation creates electron-hole pairs and induces a hole-traps which are positively charged traps



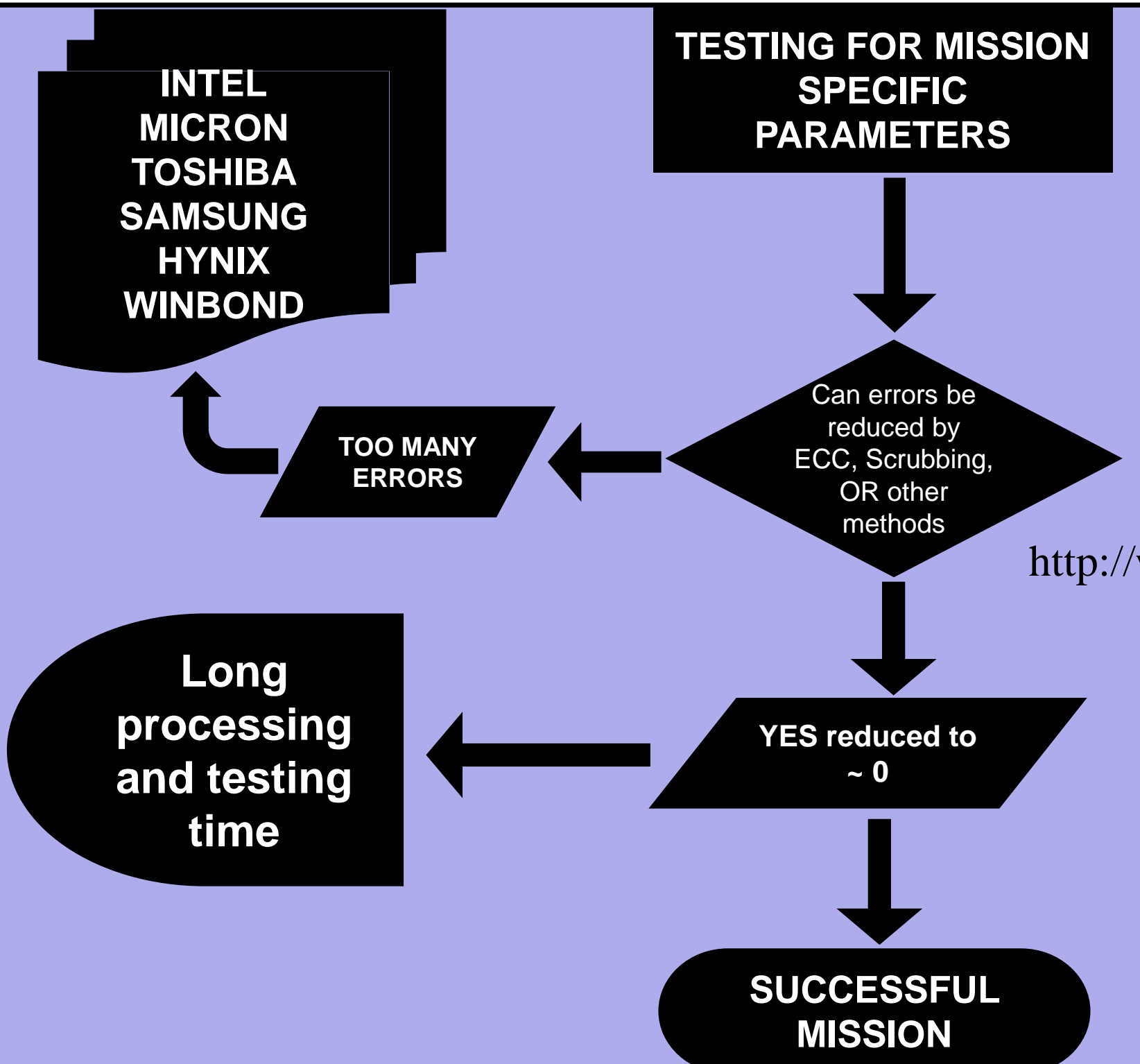
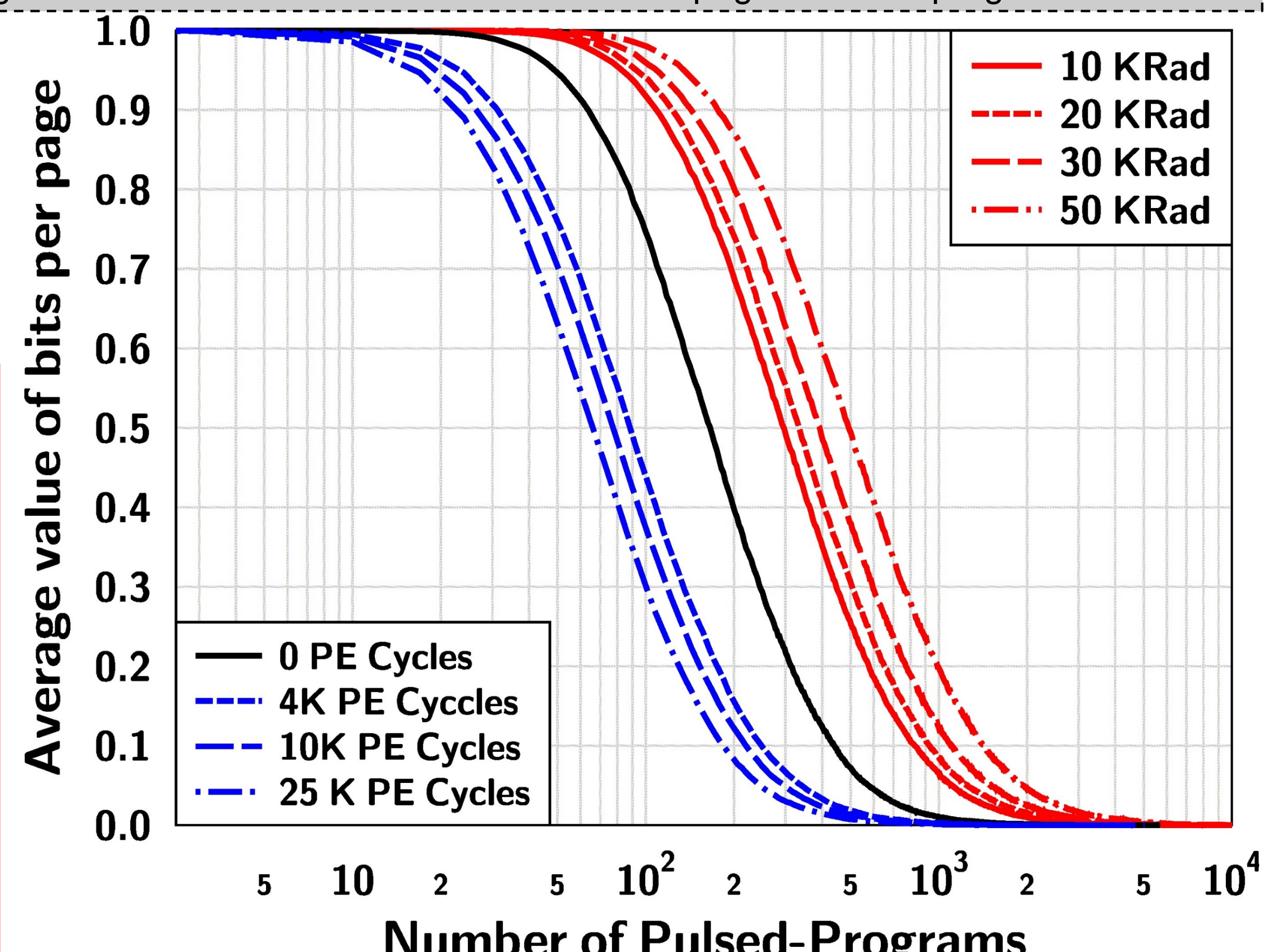
The negative electron-traps due to endurance and the positive hole-traps due to TID appear to not exhibit any interactions with each other. As it can be seen from the grey cross-lines (guide only) that as the program-erase stress increases the entire set of curves from block shift towards the lesser pulsed programs.



A program operation executes for a predefined amount time, referred here as the pulse, resulting in a single pulse program operation. A longer pulse-width can program a larger population of bits on a page. Repeating the pulse program operation many times will eventually program the entire page

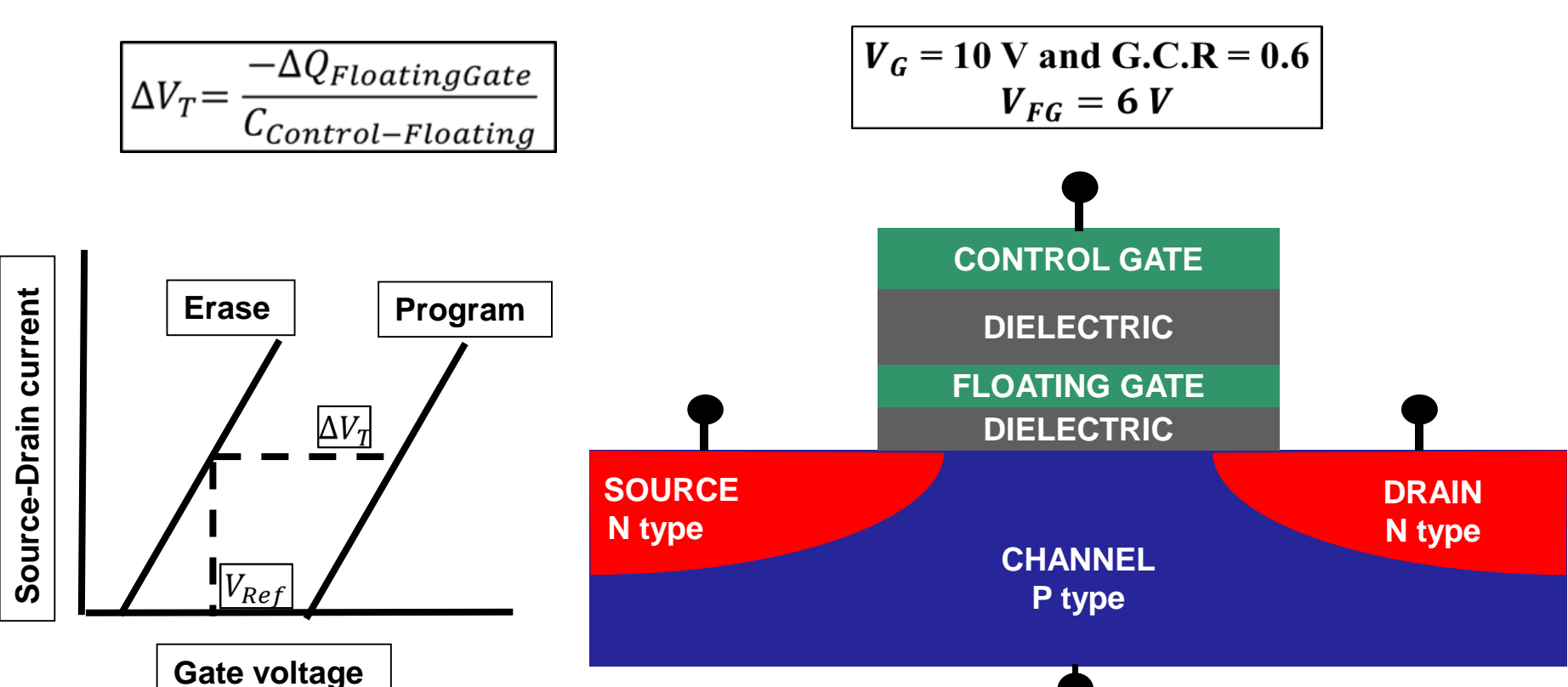


http://www.Radiation.com/products/87399/Tools-for-the-Medium-Energy-Wipe-Super-Write-Program-erase-stress made the bit cells on the page easier to program



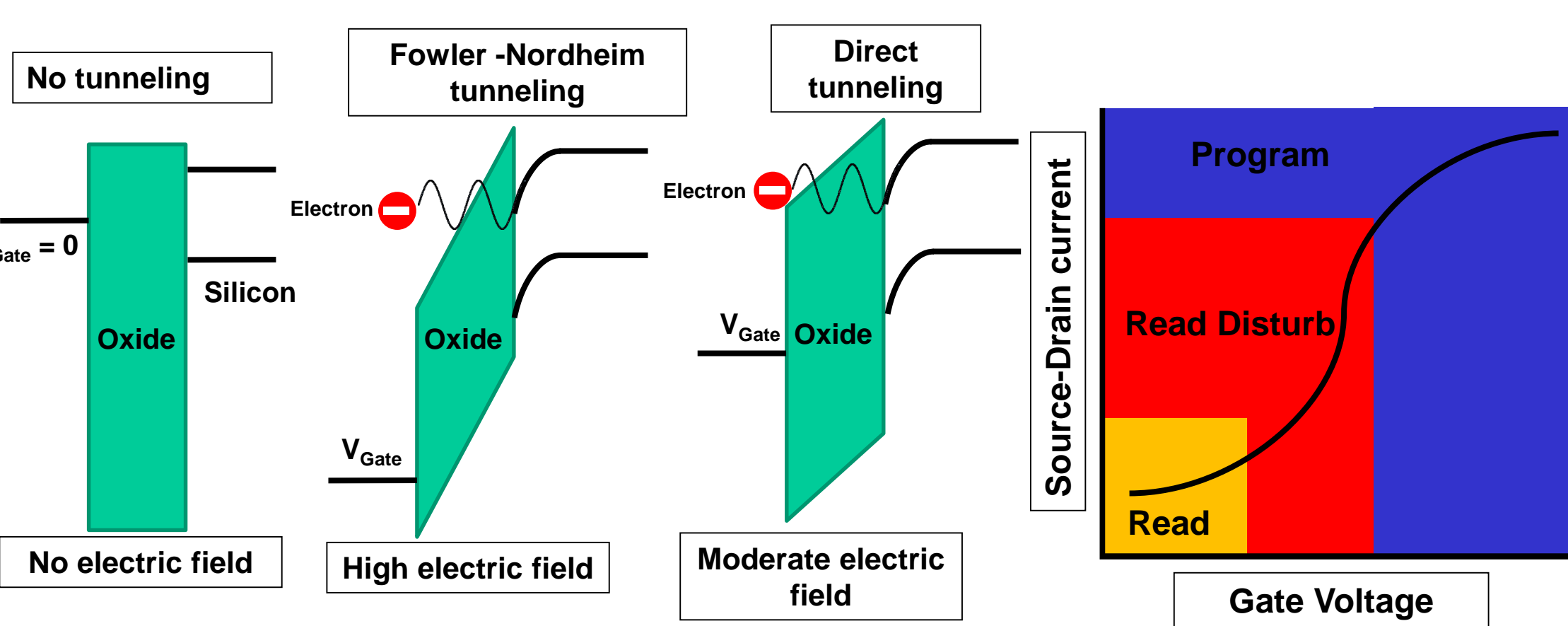
## NAND Flash memory bit and capacitive coupling

Large positive (negative) bias on the control gate induces (extracts) electrons in (from) the floating gate.



The charge i.e. positive or negative on the floating gate controls the source-drain current and bit is either programmed "0" state or erased "1"

## Storing charge in floating gate or tunneling



A large positive bias bends the barrier towards the gate and the probability of tunneling of electrons increases thus electrons are stored in the floating gate.

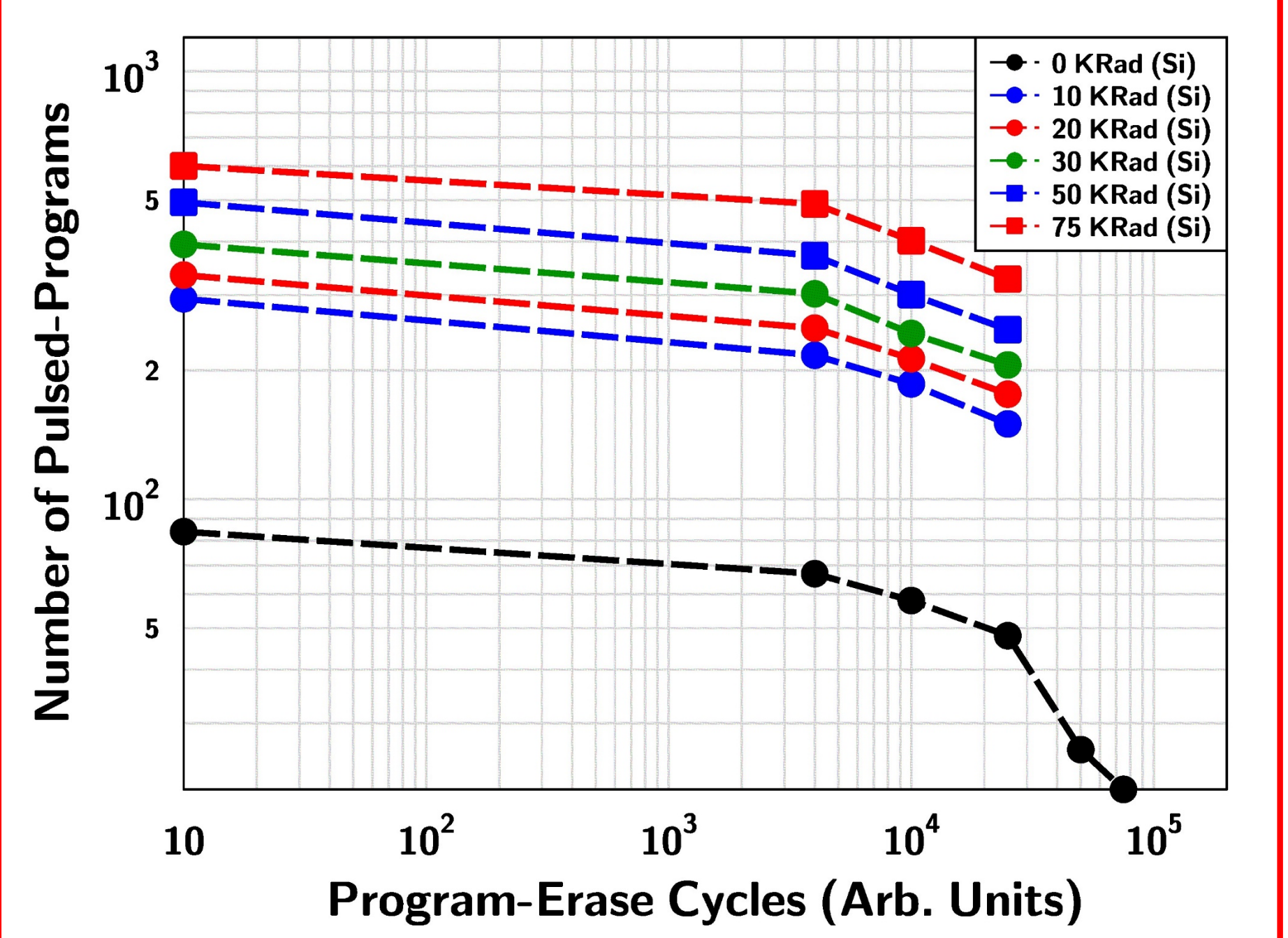
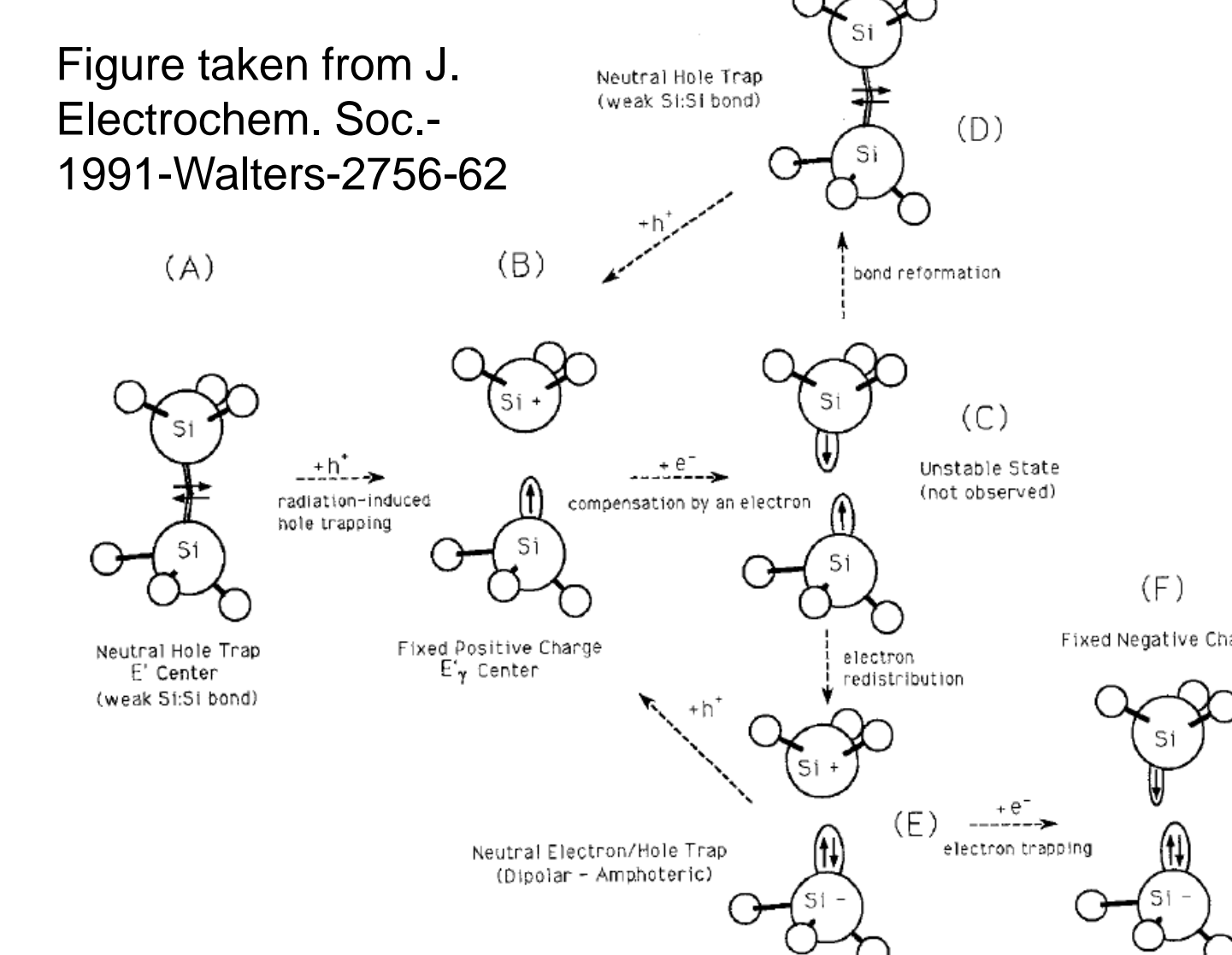


Figure displaying opposing effects of TID and endurance stress. However, if endurance does recover the damage from TID the data retention of such a sector should be significantly similar to the chip before any irradiation. Data retention studies are in progress to understand the impact of these traps.

## A species which can trap an electron or hole



In conclusion, we are able to successfully utilize pulse explore some fundamental properties at the bit level. This technique can universally extended to other chips to examine the credibility of the technique and extract bit-level information at the same time. Data retention studies are underway to validate this model.